University of Southampton

Faculty of Engineering and Physical Sciences

Optoelectronics Research Centre

Development of Wideband Optical Amplifiers and Associated Technology

by

Xin Huang

ORCID: 0000-0001-8105-3611

Thesis for the degree of Doctor of Philosophy

May 2025

University of Southampton

Abstract

Faculty of Engineering and Physical Sciences

Optoelectronics Research Centre

Degrees for Doctor of Philosopy

Development of Wideband Optical Amplifiers and Associated Technology

by

Xin Huang

This thesis presents a comprehensive investigation into the development and optimization of wideband ytterbium-doped fibre amplifiers (YDFAs) for next-generation optical communication systems operating in the 1 μm spectral region. The research encompasses a systematic exploration of various technologies and configurations, from gain-flattening filters to advanced multi-stage amplifier designs.

The research first examines gain flattening filters and long period fibre gratings as flexible, low-loss solutions for flattening amplifier gain. Dielectric thin-film filters and programmable waveshapers are also evaluated for their precision and flexibility, offering a range of approaches to address gain flattening in optical amplifiers. Further analysis and design of multi-stage EDFAs (Erbium-doped fibre amplifiers) show how optimized GFFs (gain flattening filters) improve gain flatness with minimal noise figure degradation. Despite bandwidth extension challenges, the findings suggest multi-stage configurations and filter optimization as effective strategies for enhancing amplifier performance, providing crucial insights that informed subsequent work on YDFAs.

The core of the thesis presents groundbreaking advancements in YDFA technology. Single-stage and dual-stage configurations were extensively simulated and experimentally validated, culminating in the demonstration of a dual-stage YDFA with a 50 nm gain bandwidth (1025-1075 nm). This bandwidth, equivalent to 13.7 THz, significantly surpasses that of conventional C-band EDFAs. Further optimization led to the development of cladding-pumped YDFAs for long-wavelength operation, showcasing superior gain stability and power conversion efficiency. A hybrid core + cladding pump scheme demonstrated particular promise, achieving broader bandwidth and lower noise figures. The research culminated in the creation of an ultra-wideband YDFA combining two amplifiers operating in different windows (1025-1072 nm and 1075-1110 nm). This innovative parallel configuration achieved a remarkable bandwidth of 21.9 THz, nearly five times that of a C-band EDFA. Simulations also explored potential extensions to both shorter and longer wavelengths, indicating promising avenues for future development. The thesis concludes by outlining key areas for future research.

Table of Contents

Table of Tables

Table of Figures

Research Thesis: Declaration of Authorship

Print name: Xin Huang

Title of thesis: Development of Wideband Optical Amplifiers and Associated Technology

I declare that this thesis and the work presented in it are my own and has been generated by me as the result of my own original research.

I confirm that:

1. This work was done wholly or mainly while in candidature for a research degree at this University;
2. Where any part of this thesis has previously been submitted for a degree or any other qualification at this University or any other institution, this has been clearly stated;
3. Where I have consulted the published work of others, this is always clearly attributed;
4. Where I have quoted from the work of others, the source is always given. With the exception of such quotations, this thesis is entirely my own work;
5. I have acknowledged all main sources of help;
6. Where the thesis is based on work done by myself jointly with others, I have made clear exactly what was done by others and what I have contributed myself;
7. Parts of this work have been published as: [see list of publications]

Signature:

Date:

Acknowledgements

The four years' PhD study has been an incredibly valuable and unforgettable experience. I am filled with gratitude, especially during the challenging times of COVID-19 in the first two years of my PhD. This period has been both difficult and unforgettable, and I feel fortunate to have been part of the ORC, where I received unwavering support from my colleagues and mentors.

I would like to express my heartfelt thanks to my supervisors, Prof. David J. Richardson, Dr. Yongmin Jung, and Dr. Lin Xu. I am particularly grateful to Dave for giving me the opportunity to pursue my PhD at ORC. I vividly remember our first conversation during my PhD interview when he inquired about my family's well-being during the peak of the COVID crisis in China. That gesture made me feel both relieved and warmly welcomed. Dave's wisdom and knowledge have been invaluable in steering my research in the right direction. Despite his busy schedule managing numerous projects and supervising many students, he has always been prompt in replying to emails and offering guidance. I am especially thankful to Yongmin, my main supervisor, whose support has been instrumental in my experimental work. Yongmin has consistently made himself available for discussions. His patience and willingness to help whenever I needed guidance have been truly appreciated. I would also like to thank Lin, who joined my journey in the final year of my PhD. Lin's insightful suggestions and constructive feedback have greatly enriched my work and helped me refine my ideas.

I would also like to sincerely thank Dr. Sijing Liang, Dr. Yang Hong, and Dr. Di Lin for their invaluable assistance with my experiments. Sijing has been like a mentor to me, providing not only guidance in my projects but also advice on my future career. Di's advice and help during the first year of my PhD, especially when the lab was nearly closed, meant so much to me. I am grateful for Yang's collaboration during the transmission experiments.

My heartfelt thanks go out to all the members of the Pulsed Fibre and Laser Group: Dr. Hans Christian Mulvad, Qiang Fu, Duanyang Xu, Kunhao Ji, Mattew Gerard, Yudi Wu, Viktor Zuba, Ibrahim Abughazaleh, Jikun Yan, Panuwat Srisamran and Jing Meng. Thank you for your generosity in sharing equipment and your readiness for discussions. I would also like to thank Dr. Kyle Bottrill, Dr. Meng Huang, and Dr. Meng Ding for sharing their experience and offering help despite not being from our lab.

I am incredibly thankful for the friends who have made my life in Southampton not only bearable but also enjoyable: Lulu Wang, Huainan Wang, Xiaomeng Feng, Meijing Liu, Zijian Xu, Yiyuan Zhang, and Xiangyu Qu, Tongtong Yan and Szu-min Yu. I am also deeply grateful to my friends in China—

Haohao Wang, Fengfei Sui, Guilei Zhu, Jiaming Liu and Jingjing Qiu— thank you for being my connection to home and for your unwavering support across the distance.

Last, but certainly not least, I want to express my profound gratitude to my parents. Your selfless love and support, both financial and emotional, have been the bedrock of my academic journey. A special thank you to my cousin, Yue Wang, who has been my confidant and source of comfort during moments of homesickness and loneliness.

A big thank-you to all of you. Your support has made this journey wonderful!

Definitions and Abbreviations

ASE ..... amplified spontaneous emission

ATT ..... optical attenuator

B2B ..... back-to-back

BDFA..... bismuth-doped fibre amplifiers

BDFL ..... bismuth-doped fibre lasers

BER ..... bit error rate

BPF ..... band pass filter

DC-YDF ..... double-cladding YDF

DGD ..... differential group delay

DMG ..... differential modal gain

DMT..... discrete multitone

DS-YDFA ..... dual-stage YDFA

EDFA..... Erbium-doped fibre amplifiers

EDF ..... erbium-doped fibres

ESA ..... excited state absorption

FOPA..... fibre optical parametric amplifiers

FRA ..... Fibre Raman amplifiers

GFF ..... gain-flattening filter

HCF ..... hollow core fibre

HDFA ..... holmium-doped fibre amplifiers

HD-FEC ..... hard-decision forward error correction

IL..... insertion loss

ISO ..... isolator

LAN ..... local area network

LCOS ..... liquid crystal on silicon

LD ..... laser diode

LPFG ..... long period fibre grating

MDL..... mode dependent loss

MDM..... mode division multiplexed

MIMO..... Multiple Input Multiple Output

MM ..... multimode

MZM ..... Mach-Zehnder modulator

NA ..... numerical aperture

NF..... noise figure

OC ..... optical circulator

OSA ..... optical spectrum analyser

OSNR..... Optical Signal-to-Noise Ratio

PAM4 ..... pulse amplitude modulation

PCE..... power conversion efficiency

PD..... photodetector

PDL..... polarization-dependent loss

SC-YFD..... single-clad YDF

SDM ..... space division multiplexing

SE ..... spectral efficiency

SEM..... scanning electron microscope

SLA ..... stereolithography

SMF ..... single-mode fibre

SNR..... signal-to-noise ratio

SOA ..... semiconductor optical amplifiers

SS-YDFA..... single-stage YDFA

TDFA..... thulium-doped fibre amplifiers

TGG ..... terbium gallium garnet

TLS..... tunable laser source

TMF ..... two-mode fibres

WDM ..... wavelength-division multiplexing

YDFA ..... ytterbium doped fibre amplifier

YDF ..... ytterbium-doped fibres

YIG ..... yttrium iron garnet

Chapter 1 Introduction

This chapter serves as the introduction of this thesis, starting with the motivation of this PhD project. It outlines the structure of the thesis and summarize the key achievements made during the research.

1.1 Motivation

It has witnessed an explosive and exponential growth in fibre optic communication since Charles Kao foresaw the potential of single-mode silica optical fibres in 1960s [1]. Before the development of optical amplifiers, the challenge of signal attenuation in fibre optic networks was addressed through the periodic placement of electronic regenerators. However, this approach imposed limitations on transmission capacity due to constraints in electronic bandwidth [2]. The introduction of optical amplifiers transformed this landscape, significantly increasing transmission capacity.

A pivotal moment in this evolution occurred in 1987 with the development of Erbium-doped fibre amplifiers (EDFAs) for 1.5 μm signal amplification. This breakthrough, achieved at the University of Southampton and AT&T Bell Laboratories, paved the way for a new era in optical communications. [3]. The subsequent successful undersea test of EDFAs in 1989 heralded the dawn of high-capacity submarine and terrestrial fibre networks, fundamentally altering the landscape of global telecommunications [4]. The impact of these advancements is evident in the exponential growth of commercial optical transmission systems over the past three decades. Both submarine cable and terrestrial wavelength-division multiplexing (WDM) transmission capacities have experienced nearly exponential increases, as shown in Figure 1.1, and predictions suggest this trend will continue in the next 14 years, with an estimated 40% technology scaling rate [5].

However, this rapid progression has brought the industry to a critical juncture. Telecommunication networks are approaching their capacity limits for silica single-mode fibres (SMFs) due to the nonlinear Shannon limit. This constraint necessitates innovative approaches to further expand network capabilities [6]. According to the Shannon-Hartley theorem, the maximum capacity of a communication channel is a function of bandwidth, spatial paths, and signal-to-noise ratio (SNR). Specifically, the overall fibre capacity can be expressed as [7]:

$$C = M \times B \times 2log_2(1 + SNR) \tag{1.1}$$

Where the logarithmic term reflects the maximum spectral efficiency (SE) of a dual-polarization signal, and capacity increases proportionally with system bandwidth (B) and the number of spatial paths (M).

As is evident from Equation (1.1), the overall fibre capacity is related to the spatial paths and system bandwidth, and the SE. Improving SE could be achieved through the development of low-noise optical amplifiers, low-loss and lower-nonlinearity fibres, and digital nonlinearity compensation techniques to offer incremental gains [8]. However, these approaches typically yield modest capacity improvements, generally in the range of tens of percent. The key to achieving substantial linear capacity gains lies in expanding system bandwidth (B) and increasing the number of spatial paths (M). This realization is driving research and development efforts towards novel technologies that can overcome current limitations and usher in the next generation of optical communication systems.

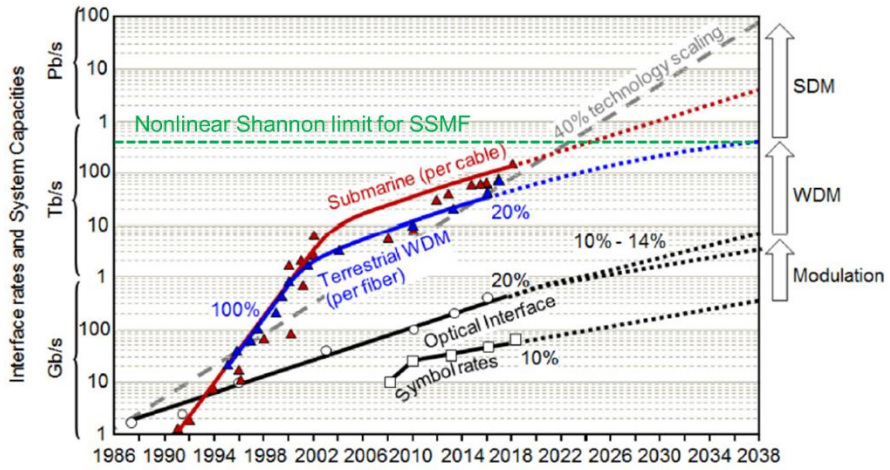

Figure 1.1: Evolution of commercial optical transmission systems over the past 30 years and extrapolations for the coming 20 years [5].

Several approaches have been explored to increase the transmission capacity, e.g., space division multiplexing (SDM) that utilizes multi-mode and multi-core fibres have been investigated to increase spatial paths (M) could significantly boosting data transmission performance [9-11]. Wideband optical amplifiers have been developed to expand the bandwidth of transmission systems. Conventional silica fibres exhibit low propagation losses of $\leqslant$0.4 dB/km across the 1260 nm to 1675 nm range, spanning from the O band to the U band. In response, various amplifier technologies have been introduced, including Raman fibre amplifiers, semiconductor optical amplifiers (SOAs), and rare-earth doped fibre amplifiers, as shown in Figure 1.2 [12].

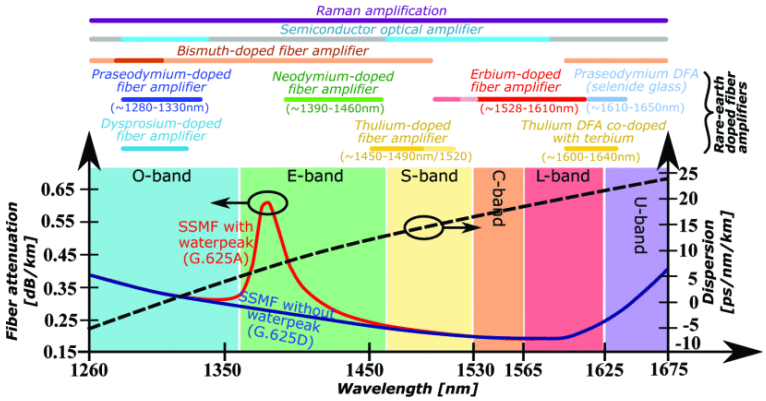

Figure 1.2: Amplifier technology for transmission in conventional silica fibres in different wavelength bands [12].

Within the rare-earth doped category, alongside the well-established Erbium-Doped Fiber Amplifiers (EDFA) operating in the C and L bands, several other amplifiers have been developed. These include Praseodymium-doped fibre amplifiers for the O band (1280-1330 nm), Dysprosium-doped fibre amplifiers, Neodymium-doped fibre amplifiers for the E band (1390-1460 nm), and Thulium-doped fibre amplifiers (TDFAs) for both the E+S band (1450-1490 nm) and the L+U band (1600-1640 nm). The Bismuth-doped fibre amplifier (BDFAs) stands out for its broad emission, providing ultra-wide bandwidth across the O+E+S bands. It is predicted that the system bandwidth requirements over the next decade could range from 5-20 THz. To meet this demand, researchers are exploring combinational approaches, such as parallel configurations that combine different amplification windows and hybrid amplifiers that integrate various types of amplifiers into a single device [13, 14].

Table 1 summarizes the operating range and bandwidth of different communication window. It is clear that the T band, operating in the 1000-1260 nm range, presents an opportunity for even wider bandwidth. However, conventional silica fibres face challenges in this region due to high propagation losses caused by Rayleigh scattering (e.g. 1.5 dB/km @1060 nm for Corning HI1060 fiber), as shown in Figure 1.3 [15]. This limitation has historically hindered the development of 1 μm wideband data transmission systems. Recent advancements in hollow core fibre (HCF) technology, particularly anti-resonant fibres [16], are changing this landscape. These innovative designs exhibit lower Rayleigh scattering losses than solid silica fibres, with a record low loss of 0.30 dB/km at 1060 nm recently reported [17], as shown in the red curve in Figure 1.3. HCFs offer several advantages over conventional silica fibres [16, 18-20]:

1) Light propagation in an air-filled core, reducing nonlinear effects.
2) Effectively single-mode guidance and ultra-low propagation loss.
3) Higher damage threshold for transmitted optical power.
4) Group velocities closer to the vacuum velocity of light, resulting in lower latency.

Table 1: Operating range and bandwidth of different communication window.

Band	Wavelength (nm)	Frequency (THz)	Bandwidth (THz)
T	1000-1260	237.9-299.8	**61.9**
O	1260-1360	220.5-238.0	**17.5**
E	1360-1460	205.4-220.5	**15.1**
S	1460-1530	196.0-205.4	**9.4**
C	1530-1565	191.6-196.0	**4.4**
L	1565-1625	184.5-191.6	**7.1**
U	1625-1675	179.0-184.5	**5.5**

HCFs have demonstrated the capability to support an ultra-wide transmission bandwidth of up to 700 nm (e.g., from 1240-1940 nm), as reported in Refs [15, 21]. Moreover, they have proven their ability to handle high-capacity data transmission, with C-band transmission at 32 GBaud demonstrated over distances of 341 km and 618 km [22, 23]. These developments highlight the feasibility and potential of 1 µm data transmission systems, creating a pressing need for suitable wideband 1 µm fibre amplifiers.

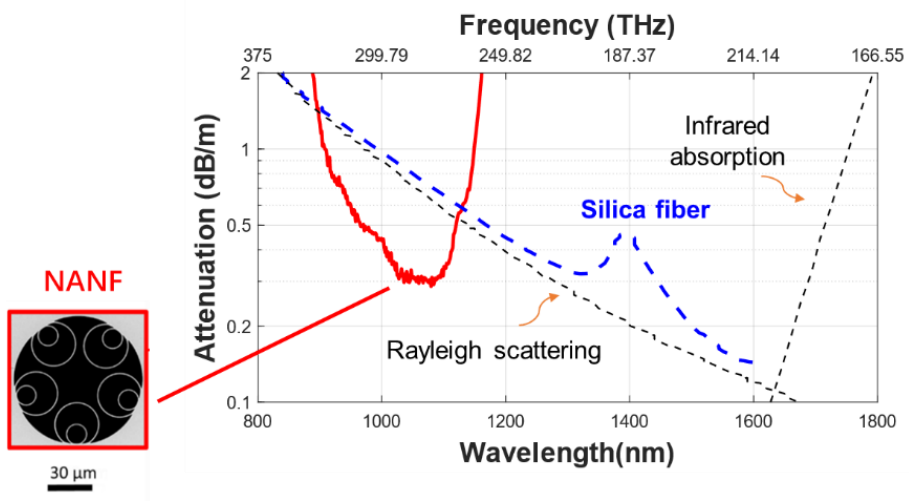

Figure 1.3: Comparison of propagation window between conventional silica fibre and NANF.

The ytterbium doped fibre amplifier (YDFA) is the most direct way to achieve a wideband amplifier at 1 µm. Ytterbium doped fibres (YDFs) serves as a versatile gain medium with a broad emission bandwidth that extends from ~976 nm to ~1178 nm [24], and they have been previously widely used for the development of high power continuous-wave and pulsed fibre laser systems due to the high efficiency [25, 26]. In addition to the broad emission bandwidth, the broad absorption spectrum of YDF allows a wide choice of pump wavelengths ranging from 800 nm to 1000 nm. Due to its simple two energy level structure, the excited state absorption and concentration quenching

by interionic energy transfer that can occur in EDFAs can be avoided in YDFAs, resulting in high output powers and excellent power conversion efficiency (PCE). Additionally, the high doping levels provide the ability to achieve high gain from a short length of fibre. Crucially, recognizing the inherent value of bandwidth at 1 µm, where 1 nm corresponds to twice the frequency bandwidth compared to 1.55 µm, is very important. According to the relation between frequency bandwidth and wavelength ($\Delta v = \frac{c}{\lambda^2}\Delta\lambda$), as depicted in Figure 1.4, a 1 nm spectral bandwidth translates to ~267 GHz at 1060 nm, in contrast to only ~125 GHz at 1550 nm. It is apparent that the YDFA holds the potential to support significantly larger data capacity than the EDFA.

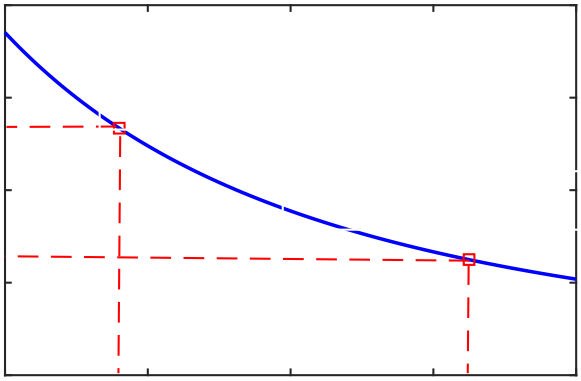

Figure 1.4: Correlation between frequency bandwidth and operating wavelength (per 1nm spectral bandwidth)

This thesis focuses on the development of wideband optical amplifiers and gain flattening technologies. The primary subject of the research is the wideband YDFA. Before delving into the wideband YDFA for telecommunications applications, an initial study was conducted on gain-flattened wideband EDFA as a foundational step to gain familiarity with amplifier technologies.

Another key aspect of this PhD study is the development of gain flattening filter technology, with a particular focus on long-period fibre gratings. In addition, thin-film-based filters and waveshaper technologies were explored, which have potential applications in both EDFA and YDFA systems as gain-flattening filters (GFFs).

1.2 Thesis Structure

This thesis is composed of four main parts:

Part I (Chapter 1-Chapter 2): This part provides the background and theoretical foundation of the thesis.. Chapter 1 introduces the motivation behind the PhD project, outlines the thesis structure,

and highlights the key achievements of the research. Chapter 2 delves into the relevant theories and summarizes the current state of technology, covering the fundamentals of optical amplification, including concepts such as gain, amplified spontaneous emission (ASE), noise figure (NF), PCE. It also explores the spectroscopic characteristics of rare-earth ions, pumping schemes of amplifiers, multi-stage amplifiers, and provides an overview of optical amplifier technologies.

Part II (Chapter 3): This part focuses on the development of GFF technologies, with an emphasis on the design of SMF long-period fibre gratings used as GFFs and the implementation in two-mode fibres (TMFs) as mode scramblers. Other GFF technologies, such as waveshapers and thin-film-based filters, are also introduced, which are applied in the subsequent amplifier chapters.

Part III (Chapter 4): This part presents the study of gain-flattened wideband Erbium-Doped Fiber Amplifiers (EDFA) operating in the C and C+L bands. The research in this chapter serves as a preliminary exploration, laying the groundwork for the subsequent wideband YDFA investigations.

Part IV (Chapter 5 - Chapter 7): This is the main part of the thesis, focuses on the development of YDFA for optical communication at 1μm. Chapter 5, describes the development of a gain-flattened dual-stage YDFA operating in the 1025-1075 nm range, and the demonstration of preliminary data transmission experiments over a 16.3 THz bandwidth (1020-1080 nm) in HCF. Chapter 6 expands on this by discussing the extension of the YDFA's operation range to 1070-1110 nm, achieved through a novel hybrid core+cladding pump scheme. In Chapter 7, the results are integrated by combining a gain-flattened dual-stage YDFA (1025-1072 nm) with a hybrid core+cladding pumped dual-stage YDFA (1075-1110 nm) in a parallel configuration, realizing an ultra-wideband YDFA with a total bandwidth of 21.9 THz over an 82 nm spectral range.

1.3 Key Achievements

The key achievements of my PhD study are summarised as follows:

1. Investigation of LPFGs as the GFF in SMF and mode scrambler in TMF, and design the LPFGs as the GFF for use in both EDFA and YDFA.
2. Investigation of wideband gain-flattened C band and L band EDFA
3. First demonstration of a gain-flattened wideband YDFA operating in the 1025-1075 nm range, with over 20 dB gain, optimized for 1 μm data transmission in HCF.
4. Collaborate with telecommunication group to demonstrate the first preliminary 1 μm data transmission experiment in HCF, covering a bandwidth of 16.1 THz.
5. First demonstration of an ultra-wideband YDFA operating in the 1025-1110 nm range, with a total bandwidth of 21.9 THz.

Chapter 2 Background and Theory

2.1 Fundamentals of Optical Amplification

The concept of optical amplification was first introduced by Albert Einstein in 1916 within the field of quantum optics, which explores the interactions between light and matter at the quantum scale. According to Einstein's theory [27], if a laser-active atom or ion is in an excited state, such as through optical pumping, it will naturally transit to a lower energy state, releasing energy in the form of a photon. This process, called spontaneous emission, occurs randomly in space, with the photon emitted in a random direction.

In addition to spontaneous emission, Einstein's theory also describes stimulated emission. In this process, if an excited atom or ion encounters a photon whose energy matches the energy difference between the excited state and the ground state, it will release an additional photon. This second photon will be identical to the original in terms of frequency, phase, direction, and polarization, effectively doubling the number of photons. As a result, the intensity of the light is amplified, with both photons traveling together. This is the fundamental mechanism of optical amplification, which is critical in the operation of lasers and optical amplifiers [27].

To understand the principle of above absorption, spontaneous emission and stimulated emission process, we can consider a simplified degenerate two-level system, where ground state (level 1) has degeneracy g_1 and excited state (level 2) has degeneracy g_2, as illustrated in Figure 2.1.

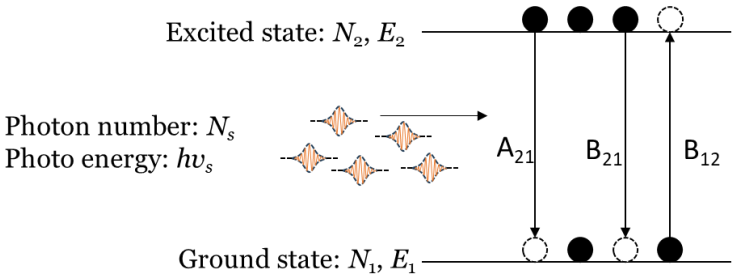

Figure 2.1: Diagram of a two-level system.

2.1.1 Einstein's coefficients

By definition, N_1 and N_2 represent the populations for ground state (E_1) and excited state (E_2) respectively. The population changes in levels 1 and 2 are governed by the transition strengths between the individual sublevels that compose each energy level. It is assumed that the total number of atoms in these two levels remains constant throughout the process. If the sublevels are

equally populated, or if the transition strengths between sublevels are uniform, the population change for each energy level can be expressed as [2]:

$$\left(\frac{dN_1}{dt}\right)_{absorption} = B_{12}\rho(v)N_1 \tag{2.1}$$

$$\left(\frac{dN_2}{dt}\right)_{spontaneous} = -A_{21}N_2 \tag{2.2}$$

$$\left(\frac{dN_2}{dt}\right)_{stimulated} = -B_{21}\rho(v)N_2 \tag{2.3}$$

Where $\rho(v)$ is the radiation energy density, A_{21} , B_{12} and B_{21} are Einstein's coefficients corresponding to spontaneous emission, absorption and stimulated emission, respectively.

At thermal equilibrium, the steady-state condition is given by the balance of absorption and emission processes [2]:

$$\left(\frac{dN_1}{dt}\right)_{absorption} = \left(\frac{dN_2}{dt}\right)_{spontaneous} + \left(\frac{dN_2}{dt}\right)_{stimulated} \tag{2.4}$$

Combining Equation (2.1), (2.2) and (2.3), we arrive at:

$$B_{12}\rho(v)N_1 = -A_{21}N_2 - B_{21}\rho(v)N_2 \tag{2.5}$$

$$\rho(v) = \frac{A_{21}}{\left(\frac{N_1}{N_2}\right)B_{12} - B_{21}} \tag{2.6}$$

According to Boltzmann's law, the population ratio between the two levels is given by [28]:

$$\frac{N_1}{N_2} = \exp\left(\frac{hv_s}{kT}\right) \tag{2.7}$$

Substituting into Equation (2.6),

$$\rho(v) = \frac{A_{21}}{\frac{g_1}{g_2}\exp\left(\frac{hv_s}{kT}\right)B_{12} - B_{21}} \tag{2.8}$$

The radiation energy at frequency v in the thermal equilibrium can also be expressed by Planck's law [28]:

$$W = \rho(v)hv = mhv\frac{1}{\exp\left(\frac{hv_s}{kT}\right) - 1} \tag{2.9}$$

Where m is the number of modes in a given volume and spectral interval. To ensure consistency between Einstein's equations and Planck's law at thermal equilibrium, combining Equations (2.8) and (2.9) leads to the following relationships, known as Einstein's relations:

$$B_{12} = \frac{g_1}{g_2} B_{21} \tag{2.10}$$

$$\frac{A_{21}}{B_{21}} = m = \frac{8\pi v^2 hv}{c^3} \tag{2.11}$$

For a simple system with no degeneracy ($g_1 = g_2$), the Einstein coefficients for absorption and stimulated emission are equal, i.e., $B_{21} = B_{12}$.

2.1.2 Population inversion

Einstein's work established the relationship between stimulated and spontaneous emission probabilities:

$$R_{21} = AN_2 + BN_2W \tag{2.12}$$

$$R_{12} = BN_1W \tag{2.13}$$

Where R_{21} and R_{12} represent the transition rates from level 2 to 1 and 1 to 2, respectively. The gain in the system is proportional to the population difference:

$$g \propto (N_2 - N_1) \tag{2.14}$$

For amplification to occur, we require more atoms in the upper energy level than in the lower energy level, a condition known as population inversion [29]:

$$N_2 > N_1 if\ E_2 > E_1 \tag{2.15}$$

This condition contrasts sharply with the natural state of atomic systems at thermal equilibrium. According to the Boltzmann distribution, in a collection of atoms at thermal equilibrium, higher energy levels are always less populated than lower levels. Consequently, the population difference ($N_1 - N_2$) is typically positive, resulting in a positive absorption coefficient $\alpha(\nu s)$. This means that under normal conditions, incident radiation is absorbed rather than amplified, as illustrated in Figure 2.2(a). Population inversion represents an abnormal situation that is characterized by a negative population difference ($N_2 - g_2N_1/g_1$), as illustrated in Figure 2.2(b) [29]. The point at which the populations of both states become equal is referred to as the "inversion threshold".

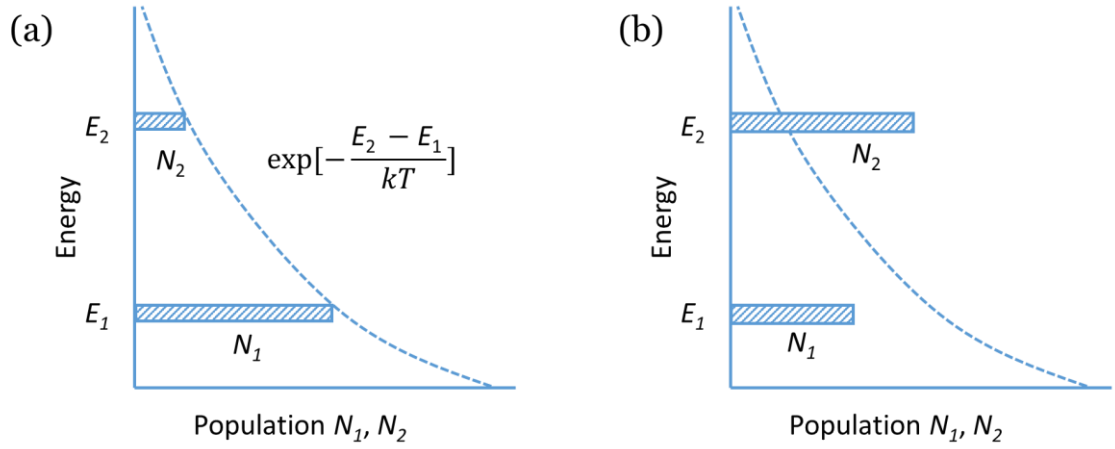

Figure 2.2: (a) Populations in two energy levels express by Boltzmann's law; (b) inverted population at two states for amplification [29].

It's important to note that stimulated absorption and emission processes always occur simultaneously, regardless of the population distribution among the energy levels. The balance between these processes determines whether the incident radiation is attenuated, transmitted unchanged, or amplified [29]:

1. When $N_1 > N_2$: Absorption dominates, leading to attenuation of the radiation.
2. When $N_1 = N_2$: The number of emissions equals the number of absorptions, rendering the material transparent to the incident radiation.
3. When $N_2 > N_1$: Emission processes predominate, resulting in amplification of the radiation as it passes through the material.

Achieving population inversion requires external energy to populate the higher energy level. This energy is referred to as pump energy, which is typically supplied by optical or electrical pumping in laser and amplifier systems. The pump energy forces atoms or ions into the excited state, creating the inversion necessary for amplification to take place [29].

2.1.3 Atomic Lineshapes and linewidth broadening

In above discussed two-level system, the interaction between an atomic system was modelled assuming an infinitely sharp energy gap. However, in practical scenarios, the interaction between an atomic system and incident radiation is more complex. Finite transition linewidths (Δv) and interact with signals over a bandwidth dv must be considered. To account for this, we introduce the atomic lineshape distribution $g(v, v_0)$, cantered at the resonant frequency v_0. is the equilibrium shape of the linewidth-broadened transitions. This distribution represents the equilibrium shape of the linewidth-broadened transitions. Considering N_2 as the total number of

ions in the upper energy level, the spectral distribution of ions per unit frequency can be written as [29]:

$$N(v) = g(v, v_0)N_2 \tag{2.16}$$

Integrating over all frequencies yields the total number of ions in the excited state [29]:

$$\int_0^\infty N(v)dv = N_2 \int_0^\infty g(v, v_0)dv = N_2 \tag{2.17}$$

This leads to the normalization condition for the lineshape function [29]:

$$\int_0^\infty g(v, v_0)dv = 1 \tag{2.18}$$

Thus, $g(v, v_0)$ can be interpreted as the probability of emission or absorption per unit frequency. The probability of a transition emitting (or absorbing) a photon with energy between hv and $h(v + dv)$is given by $g(v, v_0)dv$, with transitions occurring between $v = 0$ and $v = \infty$, leading to a total probability of 1.

The probability rate of transitions from the excited state can be expressed using the lineshape function as [29]:

$$-\frac{dN_2}{dt} = A_{21}N_2 g(v, v_0)dv \tag{2.19}$$

The linewidth and lineshape of atomic transitions are influenced by various broadening mechanism, such as lifetime, collision, and doppler broadening in gases, or lifetime, dipolar, thermal broadening, and inhomogeneities in solids. These mechanisms produce two primary types of atomic lineshapes: homogeneous and inhomogeneous broadening.

In homogeneous broadening, all atoms share the same lineshape and frequency response. This means that an applied signal affects all atoms uniformly within the linewidth. Homogeneous broadening typically results in a Lorentzian lineshape, described mathematically by [29]:

$$g(v) = \left(\frac{\Delta v}{2\pi}\right)[(v - v_0)^2 + \left(\frac{\Delta v}{2}\right)^2]^{-1} \tag{2.20}$$

Where v_0 is the centre frequency and Δv is the width between the half-power points of the curve. The factor $\frac{\Delta v}{2\pi}$ assures normalization. According to Equation (2.18) and Equation (2.20), the peak value for the Lorentz lineshape is:

$$g(v_0) = \left(\frac{\Delta v}{2\pi}\right) \tag{2.21}$$

Inhomogeneous broadening arises from variations in atomic environments, particularly in solids. This leads to a Gaussian lineshape, described by [29]:

$$g(v) = \frac{2}{\Delta v}\left(\frac{In2}{\pi}\right)^{1/2}\exp\left[-\left(\frac{v - v_0}{\frac{\Delta v}{2}}\right)^2 In2\right] \tag{2.22}$$

with a peak value given by:

$$g(v) = \frac{2}{\Delta v}\left(\frac{In2}{\pi}\right)^{1/2} \tag{2.23}$$

Figure 2.3 shows a comparison between normalized Gaussian and Lorentzian lines for a common linewidth.

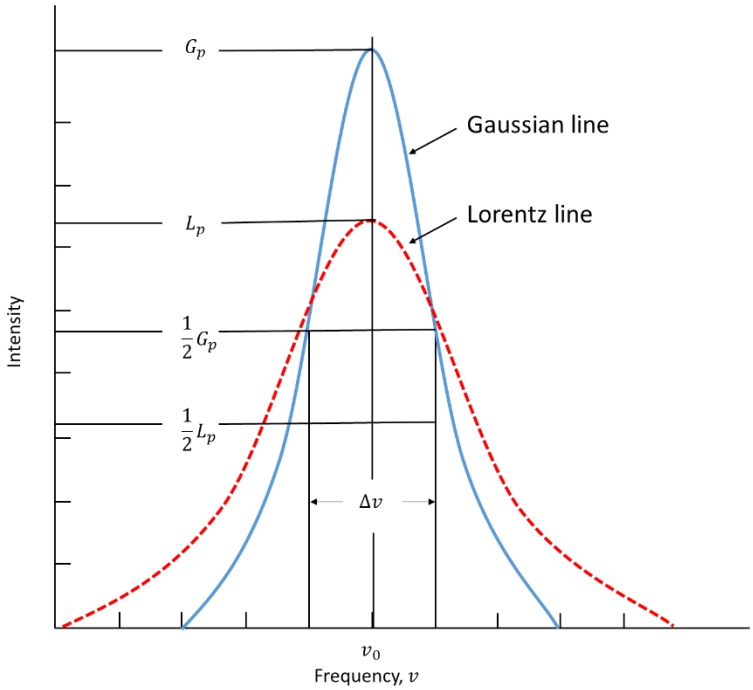

Figure 2.3: Gaussian and Lorentz lines of common linewidth (G_p and L_p are the peak intensities) [29].

The type of broadening mechanism present in an optical amplification system has significant implications for its behaviour and performance. For example, homogeneously broadened systems tend to have a smoother and more uniform spectral response, while inhomogeneously broadened systems can exhibit more complex spectral features due to the varying environments of the active ions, as illustrated in Figure 2.4. When it comes to gain saturation, in homogeneously broadened systems, saturation affects all atoms within the linewidth uniformly. This results in a uniform reduction of gain across the entire spectral range when the system is saturated. In contrast, inhomogeneously broadened systems exhibit spectral hole burning, where saturation occurs primarily at the frequency of the incident signal, leaving other parts of the spectrum relatively

unaffected, as shown in Figure 2.4. Homogeneously and inhomogeneously broadened systems also influences other aspects of optical amplifier performance, such as energy transfer, pump efficiency, amplifier noise. Understanding these broadening mechanisms and their effects is crucial for designing and optimizing optical amplifiers for specific applications. For example, EDFAs used in telecommunications, the inhomogeneous broadening of erbium ions in glass hosts contributes to their broad gain bandwidth, making them suitable for wavelength division multiplexed (WDM) systems [2].

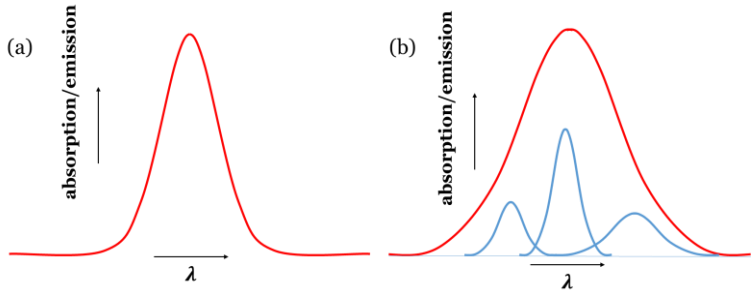

Figure 2.4: (a) a homogeneously broadened line for a collection of ions with identical transition frequencies and lifetimes; (b) in-homogeneously broadened line made up of a collection of homogeneously broadened lines with different centre frequencies and linewidths [2].

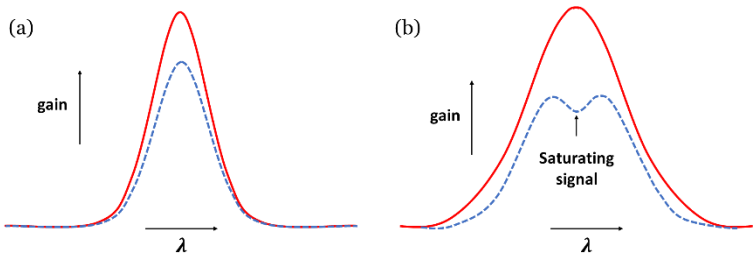

Figure 2.5: Gain saturation for a broadened line (red solid line: unsaturated gain; blue dashed line: saturated gain in the presence of a strong signal). (a) gain saturation for a homogeneously broadened line; (b) gain saturation for an inhomogeneous broadened line (the spectral position of the narrow band signal is indicated by the arrow) [2].

2.1.4 Emission and absorption cross sections

If we consider the interaction between two linewidth-broadened energy levels, the concept of cross-sections should be introduced. Cross sections quantify the ability of an ion to absorb and emit light and they are related to the Einstein A and B coefficients, which describe the probabilities of radiative transitions between energy states. The cross-section of a particular transition reflects the likelihood that the ion will absorb or emit light during a transition between two energy states.

Consider two energy states, E_1 and E_2, respectively, where $E_1 < E_2$. The probability of absorbing a photon with energy equal to $E_2 - E_1$ is proportional to the absorption cross-section, σ_{abs}, while the probability of emitting a photon during the transition from the higher energy state (E_2)to the lower state (E_1) is proportional to the emission cross-section, σ_{emis}. Both cross-sections are measured in units of area, indicating the "target size" that an ion presents to incoming photons.

The absorbed power (P_{abs}) by an ion exposed to light of frequency ω and intensity I is given by [2]:

$$P_{abs} = \sigma_{abs} I \tag{2.24}$$

The number of absorbed photons, divided by the photon energy $h\omega$, is:

$$N_{abs} = \sigma_{12} \frac{1}{h\omega} = \sigma_{abs} \phi(\omega) \tag{2.25}$$

Where $\phi(\omega)$ represents the photon flux, representing the number of photons per unit area per unit time. Similarly, the power emitted by an ion during stimulated emission is [2]:

$$P_{emis} = \sigma_{emis} I \tag{2.26}$$

For a collection of ions with populations N_1 in the lower state and N_2 in the excited state, the net change in the power of light as it traverses this collection of ions is [2]:

$$\Delta \mathrm{P} = P_{em} - P_{abs} = (N_2 \sigma_{emis} - N_1 \sigma_{abs}) I \tag{2.27}$$

In simple systems with non-degenerate states, the absorption and emission cross-sections are typically equal. However, this symmetry is often disrupted in complex systems, such as rare earth ions in solids. Here, the energy levels are composed of multiple closely spaced sublevels, populated unevenly due to thermal distributions. For example, in rare earth ions like Er^{3+}, transitions involve a series of sublevels, such as the $^4I_{15/2}$ and $^4I_{13/2}$ states, each contributing differently to the overall transition cross-section. As a result, the absorption and emission cross-sections vary across the spectral bandwidth of the transition, reflecting the specific distribution of populations among the sublevels [2].

The cross-sections can be experimentally determined by measuring the spectral absorption and emission characteristics of the medium. Two primary methods for deriving cross-sections are the Ladenburg-Fuchtbauer relation and McCumber theory.

2.1.4.1 Ladenburg-Fuchtbauer relation

The absorption and emission cross-sections can be expressed in terms of the Einstein B coefficient as follows [2]:

$$\sigma_{abs} = \frac{h\nu n}{c} B_{12} g_{12}(\nu) = \frac{h}{\lambda} B_{12} g_{12}(\nu) \tag{2.28}$$

$$\sigma_{emis} = \frac{h\nu n}{c} B_{21} g_{21}(\nu) = \frac{h}{\lambda} B_{21} g_{21}(\nu) \tag{2.29}$$

Where $g_{21}(\nu)$ and $g_{12}(\nu)$ are the normalized lineshape functions for absorption and emission, respectively, and n is the refractive index of the medium. These functions describe how the transition probabilities vary with frequency within the broadened energy levels.

By integrating Equations (2.28) and (2.29), and by taking λ to be the centre wavelength of the transition, we can derive the following relationship:

$$g_1 \int \sigma_{abs}(\nu) d\nu = g_2 \int \sigma_{emis}(\nu) d\nu \tag{2.30}$$

The upper state 2 will have a radiative lifetime τ_{21}, considering only the decay pathway to the lower state 1 via the spontaneous emission of a photon. This lifetime is intimately connected to the emission and absorption cross-sections through quantum mechanical principles. We can express the radiative lifetime as [2]:

$$\frac{1}{\tau_{21}} = A_{21} = \frac{8\pi}{\lambda^2} \int \sigma_{emis}(\nu) d\nu = \frac{8\pi}{\lambda^2} \frac{g_1}{g_2} \int \sigma_{abs}(\nu) d\nu \tag{2.31}$$

where λ represents the wavelength of the transition in the medium, equal to λ_0/n, with λ_0 being the vacuum wavelength. This relationship, known as the Ladenburg-Fuchtbauer relation, demonstrates how the emission cross-section is directly tied to the inverse of the radiative lifetime and the integrated transition strength. In practice, the absorption cross-section is typically measured using spectral attenuation methods, such as the cut-back technique, over a known material length. The emission cross-section is then derived from the measured fluorescence spectrum, calibrated using the integrated absorption cross-section.

It's important to note that if the sublevels of the energy states are equally populated, the lineshape functions for absorption and emission are identical ($g_{12}(\nu) = g_{21}(\nu)$). However, experimental observations often reveal differences between these lineshapes, particularly in systems with unequal sublevel populations, such as rare earth ions in solids. When sublevels are not equally populated, the relationships between the Einstein B coefficients and the cross-sections become more complex. In such cases, the traditional expressions derived from the Ladenburg-Fuchtbauer relation may not hold. To address these complexities, more advanced approaches like McCumber theory are often employed. McCumber theory provides a generalized framework that accounts for unequal sublevel populations and different transition strengths, offering a more accurate description of the system's behaviour.

2.1.4.2 McCumber Theory

McCumber theory provides a sophisticated framework for understanding the relationship between absorption and emission cross-sections in complex optical systems, particularly in doped materials such as erbium-doped fibres (EDFs). This theory is especially valuable when dealing with energy levels that are split into multiple sublevels due to environmental factors like crystal fields or lattice interactions.

In many doped systems, the energy levels involved in transitions are not isolated but split into numerous sublevels. These Stark splittings can reach magnitudes of hundreds of cm^{-1}, often comparable to or exceeding the thermal energy kT. This situation leads to significant variations in sublevel populations, governed by the Boltzmann distribution rather than a uniform distribution across all sublevels.

The Boltzmann distribution predicts that lower energy sublevels will be more populated than higher energy ones. Consequently, the relative strengths of absorption and emission transitions involving these sublevels vary with temperature, resulting in frequency-dependent differences in the absorption and emission cross-sections. For a general transition between levels 1 and 2 with sublevels indexed by m_1 and m_2, the emission and absorption cross-sections are given by [2]:

$$\sigma_{em}(v) = \sum_{m1,m2} \left(\frac{e^{-E_{m2}/kT}}{Z_2}\right)\sigma_{m_2,m_1}(v) \tag{2.32}$$

$$\sigma_{abs}(v) = \sum_{m1,m2} \left(\frac{e^{-E_{m1}/kT}}{Z_1}\right)\sigma_{m_1,m_2}(v) \tag{2.33}$$

where Z_1 and Z_2 are the partition functions of the lower and upper states, respectively, and $\sigma_{m2,m1}(v)$are the cross-sections for transitions between individual sublevels.

In the high-temperature limit ($kT \to \infty$), all sublevels are equally populated, and these expressions reduce to the Ladenburg-Fuchtbauer relations:

$$\sigma_{21}(v) = \frac{1}{g_2}\sum_{m1,m2} \sigma_{m_2,m_1}(v) \tag{2.34}$$

$$\sigma_{12}(v) = \frac{1}{g_1}\sum_{m1,m2} \sigma_{m_2,m_1}(v) = \frac{g_1}{g_2}\sigma_{21}(v)dv \tag{2.35}$$

However, at realistic temperatures, where the spread in energy among sublevels is comparable to or exceeds kT, populations are not equally distributed, leading to significant deviations from these simplified expression.

By manipulating the equations for emission and absorption cross-sections and using Boltzmann factors, McCumber derived a key relationship:

$$\frac{\sigma_{em}(v)}{\sigma_{abs}(v)} = \frac{Z_1}{Z_2}\frac{\sum_{m1,m2}(\frac{e^{-\frac{E_{m2}}{kT}}}{Z_2})\sigma_{m_2,m_1}(v)}{\sum_{m1,m2}(\frac{e^{-\frac{E_{m1}}{kT}}}{Z_1})\sigma_{m_1,m_2}(v)} \tag{2.36}$$

$$= \frac{Z_1}{Z_2}e^{(E_{12}-h\nu)/kT}\frac{\sum_{m1,m2}(\frac{e^{-\frac{E_{m1}}{kT}}}{Z_2})\sigma_{m_2,m_1}(v)}{\sum_{m1,m2}(\frac{e^{-\frac{E_{m1}}{kT}}}{Z_1})\sigma_{m_1,m_2}(v)}$$

$$= \frac{Z_1}{Z_2}e^{(E_{12}-h\nu)/kT}$$

This relationship incorporates non-equilibrium population effects, providing a more reliable basis for simulating device performance, especially under varying temperature conditions.

The quantity $\frac{Z_1}{Z_2}e^{E_{12}/kT}$ could be replaced by the expression $e^{\epsilon/kT}$, thus the McCumber relationship between the emission cross section σ_{em} and the absorption cross section σ_{abs} is thus written as [2]:

$$\sigma_{em}\,(v) = \sigma_{abs}\,(v)e^{(\epsilon-h\nu)/kT} \tag{2.37}$$

where ε is the "mean" transition energy between the two manifolds. This equation indicates that the emission and absorption cross-sections are equal only at one frequency. For frequencies higher than this crossing point, the absorption cross-section is larger, and vice versa for frequencies below the crossing point.

McCumber theory also provides a link between the radiative lifetime τ_{21} and the emission cross-section [2]:

$$\frac{1}{\tau_{21}} = \frac{8\pi n^2}{c^2}\int v^2\,\sigma_{emis}(v)dv \tag{2.38}$$

This relationship helps determine the absolute values of the emission cross-sections once the absorption cross-sections and radiative lifetime are measured. The McCumber treatment has led to excellent agreement with experiment.

The Ladenburg-Fuchtbauer relation and McCumber theory provide essential tools for determining the absorption and emission cross-sections in optical amplification systems. While the Ladenburg-Fuchtbauer relation is more applicable to systems with equal sublevel populations, McCumber theory accounts for more complex situations with varying sublevel populations. These cross-sections play a critical role in predicting the performance of optical amplifiers, such as EDFAs and

YDFAs, by influencing their gain profiles, efficiency, and bandwidth. The experimental determination of these cross-sections is crucial for modelling and optimizing the behaviour of rare-earth-doped fibre amplifiers. Figure 2.6 illustrates the measured and calculated cross sections for EDFs and YDFs from Thorlabs [30]. These cross-sections are crucial for modelling the behaviour of rare-earth doped fibre amplifiers, as will be discussed in Chapter 4 to Chapter 7.

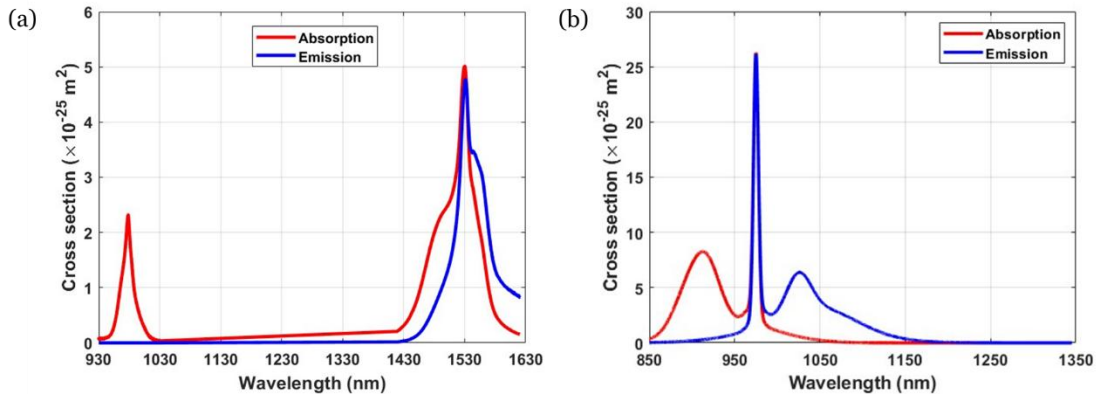

Figure 2.6: Absorption and emission cross-sections for (a) EDF and (b) YDF [30].

2.2 Fibre Amplifier Gain

2.2.1 Gain coefficient

Gain is the primary characteristic of an amplifier. Optical amplifier gain is defined as the ratio of the output signal power to the input signal power [31]:

$$G(\lambda) = \frac{P_{out}}{P_{in}} = \int_0^L g(\lambda, z) \cdot dz \tag{2.39}$$

Here, $g(\lambda)$ represents the gain coefficient, which is integrated over the length L of the active fibre. The gain coefficient is typically expressed in decibels per meter (dB/m) and depends on both the emission and absorption properties of the active medium, as well as the inversion levels at any given point in the fibre. The gain coefficient can be written as [31]:

$$g(\lambda, z) = \frac{1}{P(\lambda, z)} \cdot \frac{dP(\lambda, z)}{dz} = g^* \cdot N_2(z) - \alpha(\lambda) \cdot N_1(z) \tag{2.40}$$

Where $g^*(\lambda) = \Gamma_s n_{RE} \sigma_{emis}(\lambda)$ is the emission coefficient, $\alpha(\lambda) = \Gamma_s n_{RE} \sigma_{abs}(\lambda)$ is the absorption coefficient. Γ_s is the confinement factor of the signal mode in the fiber core, n_{RE} is the concentration of active ions in the core, and $\sigma_{emis}(\lambda)$ and $\sigma_{abs}(\lambda)$ are the emission and absorption cross-sections, respectively. $N_1(z)$ and $N_2(z)$ are the populations of ions in the ground and excited states, respectively.

The inversion level at any point (z) in the fibre amplifier is defined as:

$$Inversion\ Level = N_2/(N_1 + N_2) \tag{2.41}$$

Figure 2.7 shows the gain coefficient as a function of wavelength for different inversion levels in an EDF (Fibrecore, I-12(980/125). The Er^{3+} density is assumed to be $7.47\times10^{24}/m^{-3}$. It is seen from the figure that for 0% inversion, all ions are in the ground state and the medium is absorbing at all signal wavelengths, as the gain coefficient is negative. As the inversion level increases, however, a spectral region near the long wavelength side of the transition is characterized by a positive gain coefficient. For these wavelengths, the medium is amplifying, while for the rest of the spectrum, the medium is still absorbing. As inversion level goes to 100%, representing complete medium inversion, the region of positive gain coefficient widens to spread eventually over the whole spectral range.

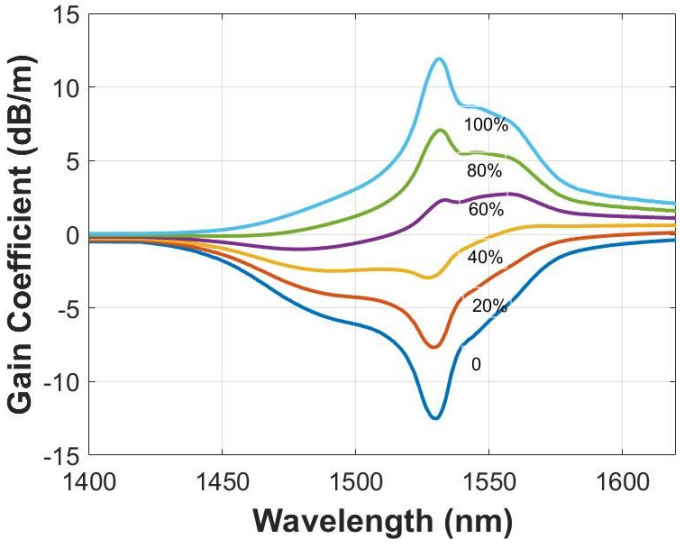

Figure 2.7: Gain coefficient as a function of wavelength for different inversion levels for an EDF.

2.2.2 Gain saturation and power conversion efficiency

The performance of rare-earth doped amplifiers is governed by fundamental physical principles, primarily the conservation of energy. This principle sets an upper limit on the signal energy that can be extracted from a fibre amplifier, which cannot exceed the stored pump energy. As a result, these amplifiers exhibit a phenomenon known as gain saturation. Gain saturation occurs when an amplifier cannot maintain a constant gain for increasingly high input powers. Instead of providing unlimited power to the amplified signal, which would violate energy conservation, the gain decreases as input power increases. This behaviour is characterized by the saturation power, defined as the input signal power at which the amplifier's gain is reduced to half of its small-signal gain. Figure 2.8 shows the gain saturation curve of an optical amplifier.

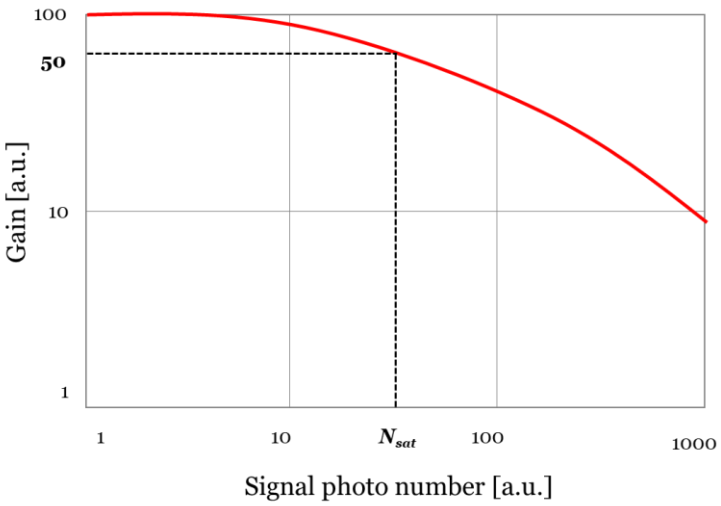

Figure 2.8: Gain saturation curve for an optical amplifier.

To better understand this phenomenon, we can express the energy conservation principle in terms of photon flux, which represents the number of photons per second [28]:

$$\Phi_p^{in} = \frac{P_p^{in}}{h\nu_p}, \Phi_s^{in} = \frac{P_s^{in}}{h\nu_s}, \Phi_s^{out} = \frac{P_s^{out}}{h\nu_s} \tag{2.42}$$

Where Φ_p^{in} is the input flux of pump photons, and Φ_s^{in} and Φ_s^{out} are the input and output signal photon fluxes, respectively. The conservation of photon flux in the amplifier is expressed as [28]:

$$\Phi_s^{out} \leq \Phi_p^{in} + \Phi_s^{in} \tag{2.43}$$

Equality in Equation (2.43) represents the ideal scenario where all pump photons are efficiently converted into signal photons. The inequality reflects realistic conditions where some pump photons do not interact with the activator ions and can be lost due to background absorption or impurities in the medium, or photons are converted into spontaneous rather than stimulated emissions. The inequality also holds when the amplifier is not being pumped ($\Phi_p^{in} = 0$), in which case output signal flux is less than or equal to the input signal flux $\left(\Phi_s^{out} \leq \Phi_s^{in}\right)$, indicating signal attenuation as it passes through the unpumped medium. Combing Equation (2.42), Equation (2.43) can be reformulated in terms of powers [28]:

$$P_s^{out} \leq P_p^{in} + \frac{\lambda_p}{\lambda_s} P_s^{in} \tag{2.44}$$

This power-based formulation provides a more practical representation for engineering applications, directly relating input and output signal powers to the pump power. It shows that the maximum output signal power depends on the ratio of the pump wavelength (λ_p) to the signal

wavelength (λ_s). Since $\lambda_p < \lambda_s$ in most amplifiers and typical operating conditions involve $P_s^{in}/P_p^{in} \ll 1$, the PCE of the amplifier P_s^{out}/P_p^{in} remains below unity.

Equation (2.44) can also be expressed in terms of amplifier gain G. For an amplifier free from spontaneous emission, $G = P_s^{out}/P_s^{in}$, and substituting from Equation (2.44):

$$G \leq 1 + \frac{\lambda_p}{\lambda_s}\frac{P_p^{in}}{P_s^{in}} = 1 + \frac{\Phi_p^{in}}{\Phi_s^{in}} \tag{2.45}$$

Equation (2.45) shows that the upper limit of the gain corresponds approximately to the ratio of the pump flux to the signal flux. Thus, the maximum possible amplifier gain corresponds to the case where each pump photon is converted into one signal photon. In the limit where the input signal power is very high ($P_s^{in} \gg (\lambda_p/\lambda_s)P_p^{in}$), the gain approaches unity, corresponding to a state of medium transparency where the amplifier ceases to amplify the signal and merely transmits it without amplification. The maximum achievable gain is constrained by ensuring that the input signal power does not exceed a threshold where amplification becomes inefficient. This threshold is given by: $P_s^{in} \leq \frac{(\lambda_p/\lambda_s)P_p^{in}}{G-1}$.

The theoretical maximum gain can only be achieved if all pump photons are absorbed by the amplifying medium. In practical amplifiers, this absorption is limited by the finite number of rare earth ions, such as rare-earth, in the medium. In a fully inverted state, the population density of ions in the excited state ($\rho = N_2$) determines the maximum gain for a laser medium of length L [28]:

$$G = \frac{P_s^{out}}{P_s^{in}} = \exp\left(\rho\sigma_{emis}L\right) \tag{2.46}$$

The gain expressed in Equation (2.46) cannot be indefinitely enhanced by increasing the fibre length L or the rare earth concentration ρ, due to the principle of energy conservation, which limits the output signal power P_s^{out}, expressed in Equation (2.44).

The overall performance of an optical amplifier, in terms of maximum gain and output power, is determined by the more restrictive of the two limits given by Equations (2.45) and (2.46),

$$G \leq min\left\{\exp(\rho\sigma_{emis}L)\,, 1 + \frac{\lambda_p}{\lambda_s}\frac{P_p^{in}}{P_s^{in}}\right\} \tag{2.47}$$

$$P_s^{out} \leq min\left\{\exp(\rho\sigma_{emis}L\,), P_p^{in} + \frac{\lambda_p}{\lambda_s}P_s^{in}\right\} \tag{2.48}$$

Optical amplifiers operating in the saturation regime to maximize output signal power are known as power amplifiers. For these devices, two key efficiency metrics are used: Power Conversion Efficiency (PCE) and Quantum Conversion Efficiency (QCE).

The PCE is defined as the ratio of the increase in signal power to the input pump power [2]:

$$PCE = \frac{P_s^{out} - P_s^{in}}{P_p^{in}} \tag{2.49}$$

The maximum achievable PCE is given by [2]:

$$PCE(max) = \frac{\lambda_p}{\lambda_s} \tag{2.50}$$

This relationship indicates that higher PCE values are attainable with longer pump wavelengths. For example, in Erbium-Doped Fiber Amplifiers (EDFAs), pumping within the $^4I_{15/2} \rightarrow {}^4I_{13/2}$ transition band (typically near 1480 nm) yields the highest PCE [2].

Since the maximum PCE depends on both pump and signal wavelengths, the Quantum Conversion Efficiency (QCE) provides a more absolute, wavelength-independent measurement. The QCE is defined as [2]:

$$QCE = \frac{\Phi_s^{out} - \Phi_s^{in}}{\Phi_p^{in}} = \frac{\lambda_s}{\lambda_p} PCE \tag{2.51}$$

The QCE's upper limit is unity, representing the ideal scenario where all pump photons are efficiently converted into signal photons.

These fundamental limitations set the baseline for understanding the performance of optical amplifiers. A wide range of optical fibre amplifiers characteristics can be tailored by varying pump wavelengths, pumping schemes, fibre designs, glass compositions, and other specific parameters. However, the actual performance of amplifiers is often constrained by other physical effects and practical technology limitations. Other physical effects include pump excited-state absorption (ESA), ASE self-saturation, concentration quenching, and inhomogeneous broadening. Technological constraints further limit optical amplifiers' performance, such as the maximum pump power deliverable by laser diodes, the precision in controlling the doping profile within the fibre, the extinction ratio of optical isolators, and intrinsic fibre background losses. These factors significantly impact the design and optimization of amplifiers, influencing their efficiency, gain flatness, and noise performance in specific applications [2].

2.3 ASE Noise and Noise Figure (Temperature)

Due to the inherent noise introduced by amplifiers, which stems from fundamental quantum limitations such as the Heisenberg's uncertainty principle, a crucial parameter called the noise figure (NF) has been established to characterize the noise performance of optical amplifiers. The NF quantifies how much the amplifier degrades the signal quality by measuring the change in SNR as the signal passes through the amplifier. Mathematically, the optical NF of an amplifier is defined as the ratio of the SNR at the input to the SNR at the output [28]:

$$NF = \frac{SNR_i}{SNR_o} = 2n_{sp}\left(1 - \frac{1}{G}\right) + \frac{1}{G} \tag{2.52}$$

Where SNR_i and SNR_o are the input and output $SNRs$ of the amplifier, respectively. G denotes the amplifier gain, and n_{sp} is the spontaneous emission factor. Since amplifiers inherently introduce noise, the output SNR is always lower than the input SNR, making the NF always greater than or equal to unity. This property reflects that optical amplifiers cannot improve the SNR of a signal; they can only degrade it.

2.3.1 Quantum limit of NF

In optical amplifiers, the noise figure approaches a minimum limit when the amplifier gain is significantly high ($G \gg 1$). Under this condition, the NF simplifies to approximately $NF \approx 2n_{sp}$. The ideal case, where the amplifier achieves 100% population inversion ($n_{sp} = 1$), results in a minimum NF of 2 (or 3 dB), commonly referred to as the 3-dB quantum limit [28]. This limit underscores the fundamental nature of noise in optical amplifiers due to quantum effects. It is noteworthy that in amplifiers with lower gains, the NF can fall below 3 dB but remains above 0 dB. This suggests that at low gain levels, the noise contribution of the amplifier becomes less sensitive to variations in gain. However, this quantum limit of the NF, often seen in linear optical amplifiers like EDFAs, does not extend to nonlinear optical amplifiers, such as fibre Raman amplifiers (FRA) or Fiber Optical Parametric Amplifiers. Nonlinear amplifiers have different noise characteristics due to their reliance on nonlinear optical processes, making the standard quantum noise limits inapplicable. These amplifiers introduce noise through mechanisms that are fundamentally different from those in linear amplifiers, requiring alternative approaches to assess their noise performance accurately.

2.3.2 Amplified spontaneous emission (ASE)

A significant noise source in optical amplifiers is amplified spontaneous emission (ASE), which occurs when excited ions in the amplifier medium spontaneously relax to a lower energy state, emitting photons that are not correlated with the signal. These spontaneously emitted photons can be amplified alongside the signal, contributing to noise and reducing the effective gain. ASE can occur at any frequency within the amplifier's emission spectrum, and it is a parasitic effect that consumes gain that would otherwise be available for the signal. The ASE power (P_{ASE}) at a specific frequency v within a bandwidth Δv can be expressed as [28]:

$$P_{ASE} = N_{ASE} h v_s \Delta v \tag{2.53}$$

where N_{ASE} is the number of ASE photons per unit bandwidth, h is Planck's constant, and v is the frequency. The NF can also be expressed in terms of ASE power as:

$$\begin{aligned} NF &= \frac{1}{G} + \frac{N_{ASE}}{G} \\ &= \frac{1}{G} + \frac{P_{ASE}}{G h v_s \Delta v} \end{aligned} \tag{2.54}$$

This expression demonstrates that the NF of an optical amplifier can be directly estimated by measuring its gain G and ASE power output, offering a practical approach to assessing amplifier performance.

2.3.3 Effective Temperature

The concept of effective temperature provides a useful way to describe the noise behaviour of amplifiers, relating the noise performance of the amplifier to a theoretical blackbody source. The effective temperature (T_a) is defined through the relationship [32]:

$$\frac{hvB}{\exp\left(\frac{hv}{k_B T_a}\right) - 1} = \frac{P_N}{G} \tag{2.55}$$

where the left side represents the power density of a blackbody radiation source, and $P_N = hvB(G-1)$ is the minimum achievable amplifier output noise power corresponds to the amplification of one photon in bandwidth B. This equation links the noise power of the amplifier to an equivalent temperature at which a blackbody source would generate the same noise level. Solving for effective temperature T_a corresponding to the minimum amplifier noise [28]:

$$T_a = \frac{h\nu}{k_B} \frac{1}{\log\left(\frac{2-\frac{1}{G}}{1-\frac{1}{G}}\right)} \tag{2.56}$$

In the high gain limit, this simplifies to the minimum effective temperature: $T_a^{min} = h\nu/k_B \log(2)$, which corresponds to the amplifier minimum effective temperature. For example, at a typical telecommunication operating wavelength of 1.55µm, this corresponds to an effective temperature of approximately 13,381 K (or 13,108 ºC). This extremely high effective noise temperature represents a quantum limit on noise in optical amplifiers (It does not reflect the actual physical (thermal) temperature of the device). This conceptual temperature corresponds to the minimum possible noise that arises due to spontaneous emission and quantum fluctuations, even under ideal conditions. In contrast, a hypothetical noise-free amplifier would exhibit an effective noise temperature of zero, indicating no thermal or quantum noise. However, such an ideal state is unattainable in practical amplifiers due to the fundamental nature of spontaneous emission and quantum fluctuations. Achieving the minimum noise power (P_N) and effective temperature (T_a^{min}) requires full population inversion within the amplifying medium, where all ions are in the excited state. This condition maximizes the efficiency of stimulated emission while minimizing the amplifier's noise contribution, approaching the theoretical noise floor dictated by quantum mechanics.

2.4 Rare-earth ions

Most linear optical fibre amplifiers are rare-earth doped fibre amplifiers due to their distinctive spectroscopic characteristics, such as broad absorption and emission cross-sections, insensitivity to the surrounding host material, and long lifetimes of their metastable energy levels. These amplifiers typically use trivalent lanthanide ions, which have an electronic configuration represented as $[Xe]4f^{N-1}5s^2 5p^6 6s^0$, where [Xe] denotes the closed-shell configuration of xenon. In this configuration, electrons are sequentially removed from the 4f and 6s shells according to the subshell filling order dictated by their energetic hierarchy [33].

One notable feature of rare-earth ions is that the 4f electrons are shielded from external fields by the outer 5s and 5p shells. This shielding effect, akin to a protective metal sphere, minimizes the interaction of 4f electrons with external fields, resulting in 4f → 4f laser transitions that display much narrower spectral lines compared to other materials, such as transition metals. This shielding effect, which resembles a protective metal sphere, preserves the atomic-like properties of these ions in both ordered (crystalline) and disordered (glassy) environments [1, 33].

The 4f configuration comprises a multitude of states that enable intra-configurational transitions before the excitation of electrons to higher orbitals like 4d or 5g. The spread of energy levels within the 4f configuration is primarily driven by electron-electron interactions within the atom. When rare-earth ions are embedded in a crystalline host, the symmetric environment of the gas phase is disrupted, leading to a phenomenon known as Stark splitting. This process further divides the energy levels into Stark components, significantly influencing the optical properties of the material. The precise nature of Stark splitting and the resultant energy level configuration play a critical role in determining the performance of rare-earth-doped materials. These factors are crucial for designing rare-earth-doped amplifiers that maintain sharp and consistent emission characteristics, as depicted in Figure 2.9. The splitting occurs in two stages: first, the atomic forces separate the original $4f^N$ configuration into multiple levels characterized by quantum numbers $2S+1_{L_J}$, representing the spin, orbital, and total angular momentum states. Subsequently, the much weaker electrostatic crystal-field Hamiltonian, about 100 times less intense than the atomic forces, further splits each of these free-ion levels into a series of Stark levels.

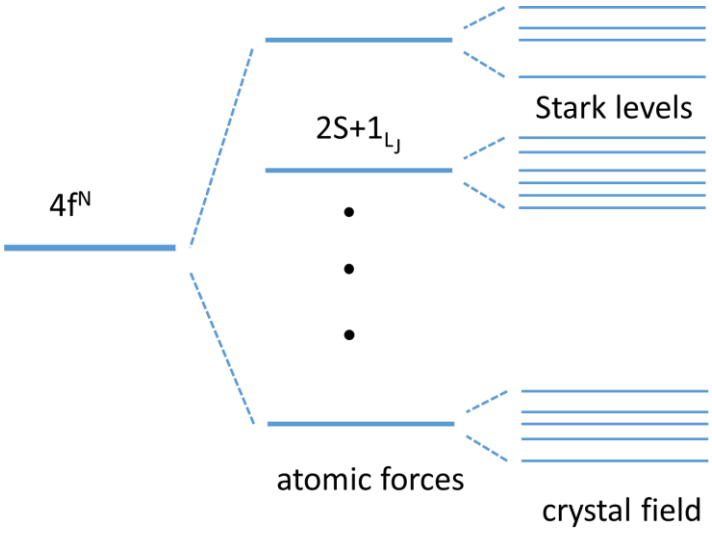

Figure 2.9: Schematic representation of the splitting of the ground configuration under the effect of progressively weaker perturbations, the atomic and crystal field Hamiltonians [2].

Figure 2.10 presents a comparison of the energy levels of Er^{3+} and Yb^{3+} ions in a silica host, highlighting the relatively simple energy structure of Yb^{3+} compared to Er^{3+} and other lanthanides. This simplicity is due to Yb^{3+} having only one missing electron in the 4f shell. The energy structure of Yb^{3+} consists of two main manifolds: an upper and a lower manifold. These manifolds are further split into Stark levels, with the upper manifold having three levels and the lower manifold having four, as shown in Figure 2.10(a).

Form the basis of Yb^{3+}'s energy structure, the ground-state $^2F_{7/2}$ manifold and the excited-state $^2F_{5/2}$ manifold, situated approximately 10,000 cm^{-1} above the ground state. Each of these manifolds is further split into sublevels, with three sublevels in the excited $^2F_{5/2}$ manifold and four in the ground $^2F_{7/2}$ manifold. The lack of closely spaced energy levels minimizes the occurrence of Excited State Absorption (ESA) at pump or laser wavelengths, a process more prevalent in Er^{3+} ions [34, 35]. Er^{3+} ions, as depicted in Figure 2.10(b), show a more complex energy structure where the ground state $^4I_{15/2}$ is split into eight Stark sublevels, and the transition level $^4I_{13/2}$ (corresponding to the transition at 1.5 µm) is split into seven sublevels. Er^{3+} ions at $^4I_{13/2}$ energy level can be excited to higher energy levels (such as $^4I_{9/2}$, $^4F_{9/2}$, and $^4S_{3/2}$) through ESA process, making them more prone to multi-phonon emissions. In contrast, Yb^{3+} has a lower multi-phonon emission rate, further improving its efficiency in a silica host.

Yb^{3+} ions in a silica host absorb light over a wide wavelength range, with two pronounced absorption maxima at 915 nm and 975 nm. These peaks correspond to transitions from the ground state (labelled 'a') to higher energy states ('e', 'f', and 'g') [36]. The emission spectrum of Yb^{3+} ions also covers a broad wavelength range, from 970 nm to 1200 nm, with distinct emission peaks around 975 nm and 1030 nm. The narrow emission line observed at 975 nm is due to the transition from the excited state 'e' back to the ground state 'a', characteristic of a quasi-three-level laser system. However, due to re-absorption at this wavelength, Yb-doped fibres are generally operated as quasi-four-level systems, where the lower energy level is positioned above the ground state to mitigate re-absorption and enhance the system's efficiency.

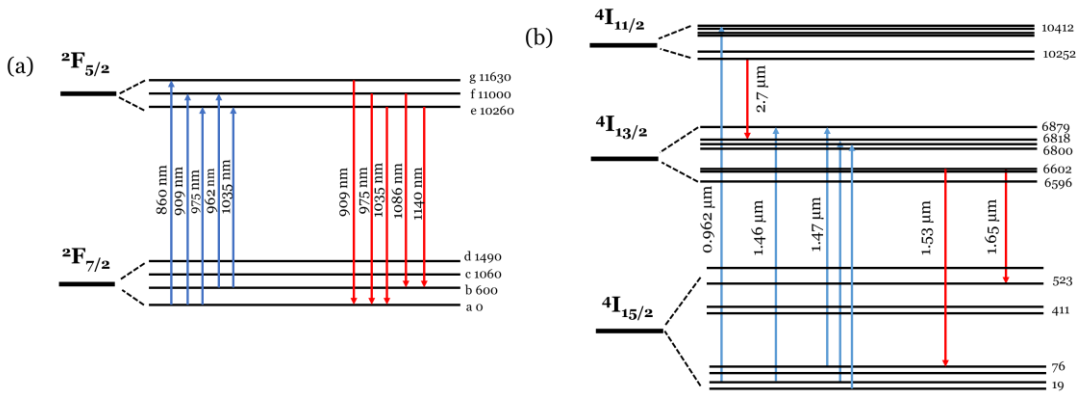

Figure 2.10: Comparison of energy level diagram between (a) Yb^{3+} [34] and (b) Er^{3+} [37] in silica.

The spectroscopic properties of rare-earth ions are strongly influenced by the local glass host environment due to variations in crystal field strength and phonon energy [38]. The phonon interactions between RE ions or other dopants can significantly affect both spectral linewidth characteristics and peak positions [39]. To tailor the spectroscopic properties of rare-earth doped

fibres, such as in Er^{3+}-doped fibre, glass hosts with lower phonon energies, including fluoride, germanate, and tellurite glasses, have been explored [40, 41]. These materials enable longer $^4I_{11/2}$ lifetime in Er^{3+}, promoting efficient emission at longer wavelengths. In addition, in Er^{3+}-doped silica fibres, systematic exploration of alternative co-dopants such as Al^{3+} or P^{5+} has demonstrated potential for further suppression of concentration quenching effects [42, 43]. This concentration quenching manifests as an energy transfer up-conversion (ETU) mechanism resulting from ion clustering within the fibre core, a phenomenon predominantly observed in Erbium-doped systems. Such clustering facilitates non-radiative energy transfer processes, including cross-relaxation and upconversion, which ultimately compromise population inversion and diminish amplification efficiency. Contemporary EDF fabrication could addresses this challenge through strategic incorporation of co-dopants (Al_2O_3 or P_2O_5). Other novel approaches, such as nanoparticle encapsulation have been suggested to isolate Er^{3+} ions and fine-tune their local environments, potentially enhancing emission efficiency [44].

Similar to EDF, the composition of the host glass matrix of YDF substantially influences Yb^{3+} ion characteristics, particularly regarding absorption and emission profiles. Dopants such as phosphorus, aluminium and germanate modify the refractive index properties and enhance Yb solubility, enabling uniform, high-concentration doping without deleterious clustering effects while simultaneously reducing optical losses in the fibre. Notably, Yb^{3+} exhibit distinct spectral behaviour in different co-dopant environments, especially in wavelength regions exceeding 1100 nm [45, 46]. This characteristic facilitates substantial gain within abbreviated fibre lengths—a considerable advantage in practical amplifier and laser applications. In contrast to EDF, Ytterbium benefits from its simplified energy level configuration, which inherently minimizes detrimental effects including excited state absorption and concentration quenching. The dual-manifold structure of Yb^{3+} naturally suppresses ETU processes, resulting in reduced state absorption and concentration quenching in YDFs. This intrinsic advantage renders YDFs exceptionally suitable for high-gain applications requiring minimal fibre length, representing a significant benefit for compact and efficient optical amplification systems.

2.5 Pump scheme of amplifiers

Optical fibre amplifiers can be classified into three main configurations based on their pumping schemes: forward-pumped (co-pumped), backward-pumped (counter-pumped), and bidirectional-pumped (dual-pumped) configurations [47]. the pump signal operates at a specific wavelength to achieve population inversion, which creates gain. The gain spectrum in these systems is influenced not only by the pumping scheme but also by the presence of other dopants in the fibre core, such as germanium and alumina. In the forward-pumping scheme, as illustrated in Figure 2.11(a), both

the input signal and the pump signal travel in the same direction along the fibre. This setup is recognized for producing moderate output power while excelling in terms of noise performance and cost-efficiency, making it especially suitable for pre-amplifier applications [48].

The backward-pumping configuration, depicted in Figure 2.11(b), features the pump signal propagating in the opposite direction to the input signal. While this arrangement yields higher output power compared to forward pumping, it offers only moderate noise performance. Despite this, backward pumping remains cost-effective and is often used in booster amplifiers, where maximizing power output is more important than noise performance.

In the bidirectional-pumping configuration, shown in Figure 2.11(c), two pump signals are used: one travels in the same direction as the input signal, while the other moves in the opposite direction. This approach delivers superior output power and maintains good noise performance. However, it is less cost-effective due to the complexity involved in combining both forward and backward pumping. Bidirectional pumping is therefore typically used in high-performance applications, such as booster and in-line amplifiers, where both high power and low noise are critical, despite the increased economic cost. Each pumping scheme presents unique advantages based on the specific application, with forward-pumping excelling in pre-amplification, backward-pumping offering greater power in booster amplifiers, and bidirectional-pumping balancing high performance with added complexity and cost.

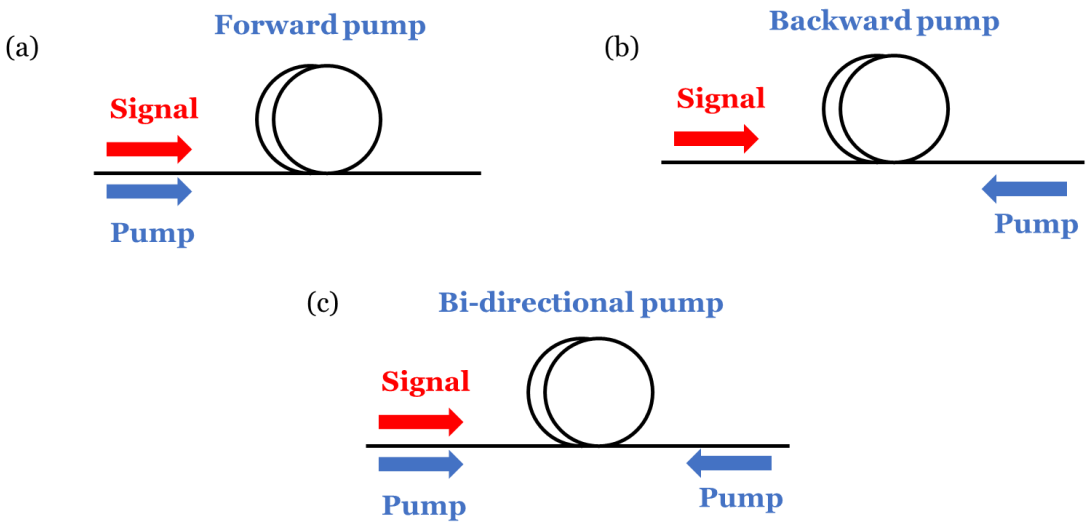

Figure 2.11: Schematic of pump configurations for optical amplifiers: (a) forward pump; (b) backward pump; (c) bi-directional pump.

2.6 Multi-stage (Cascaded) amplifier

In a single-stage amplifier, achieving both high gain and high efficiency often conflicts with the goal of maintaining a low NF. This trade-off arises because the ASE traveling in the backward direction is a primary factor contributing to higher noise, which can degrade the overall NF of the amplifier. To address this issue, the design of multi-stage amplifiers becomes essential, as it has been recognized that backward ASE can be significantly reduced in such configurations. Multi-stage, or cascaded amplifiers, offer a solution by distributing the amplification process across multiple stages, allowing better control over both gain and noise performance [49]. In these amplifiers, the first stage can be optimized for low noise, while subsequent stages focus on maximizing gain and efficiency. This strategic separation of functions reduces the negative impact of backward ASE on the system's NF, improving the amplifier's overall performance. Figure 2.12 illustrates the schematic of a multi-stage (cascaded) amplifier, where the amplification is spread across multiple stages to balance high gain, efficiency, and low noise. This approach is commonly used in advanced optical systems to enhance performance while minimizing unwanted ASE and other noise-related issues.

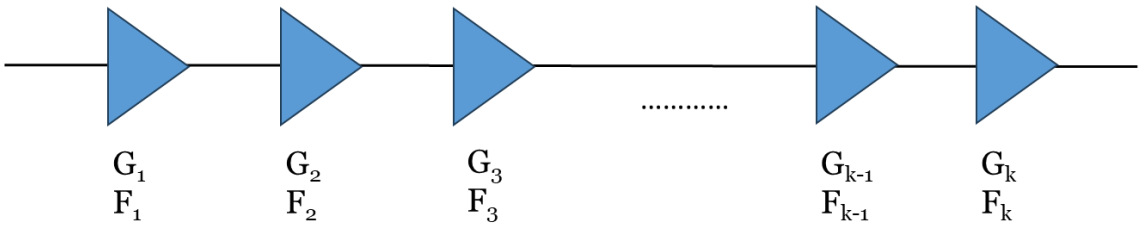

Figure 2.12: schematic of multistage (cascaded) amplifiers.

The gain of a multistage amplifier is determined by cascading the gain at each individual stage. This relationship can be expressed as follows:

$$G = G_1 G_2 G_3 \dots G_k \tag{2.57}$$

In decibels (dB), this is written as [28]:

$$G = G_1 + G_2 + G_3 + \cdots + G_k(dB) \tag{2.58}$$

To illustrate the NF of a multi-stage amplifier, firstly consider a simple case involving two stages connected in series, ff there is no input signal to the amplifier, the noise generated by the first stage will be the only signal at the output of that stage. This noise will then be amplified by the second stage, and the noise generated by the second stage itself will be added to the system. The formula for determining the NF of a two-stage amplifier is as follows:

$$NF = NF_1 + (NF_2 - 1)/G_1 \tag{2.59}$$

Where NF represents the total NF of the two-stage amplifier, NF_1 and NF_2 represents the NF of the first and second stage amplifier respectively. G_1 is the gain at the first stage. From this equation, it is clear that the NF of the first stage has a larger impact on the total NF of the system. A higher gain in the first stage reduces the contribution of noise from subsequent stages to the overall NF.

As the number of amplification stages increases, the overall NF formula for the cascade amplifier can be generalized as follows [28]:

$$NF_{total} = NF_k + G_k \cdot \{NF_{k-1} + G_{k-1} \cdot [\dots NF_3 + G_3 \cdot (NF_2 + G_2 \cdot NF_1)]\} \tag{2.60}$$

Upon analysing this formula, several key conclusions can be drawn: (1). The first stage of amplification should have the lowest NF because its noise will propagate and be amplified by all subsequent stages. Thus, minimizing the noise at the first stage is crucial to keeping the total NF as low as possible. (2). The final amplification stage should have the lowest gain among all stages. This is because the gain of the last stage amplifies the noise contributions from all the previous stages. Lowering the gain in the final stage helps reduce the amplification of accumulated noise. By

carefully designing each stage in the amplifier, particularly focusing on optimizing the noise performance of the first stage and managing the gain distribution, the overall efficiency and noise figure of a multistage amplifier can be significantly improved.

2.7 Overview of optical amplifiers

Enhancing the optical bandwidth of fibre amplifiers is a critical step in boosting the transmission capacity of Dense Wavelength Division Multiplexing (DWDM) systems. While significant progress has been made in optimizing standard single-mode fibre (SSMF) systems, their capacity remains constrained by the limitations of current amplification technology. The widely used EDFAs operate primarily within the C- and L-bands, covering wavelengths from 1530 to 1620 nm. This restricted range results in a capacity ceiling of approximately 10 THz for SSMF transmission systems. To overcome this barrier, researchers are exploring ways to expand the amplification bandwidth beyond these traditional bounds. [50]. A promising solution for near-term advancement lies in extending the amplification range to encompass a broader spectrum, from the O-band to the U-band (1260–1675 nm). This expanded range is particularly attractive because existing telecom silica fibres exhibit low transmission losses (less than 0.4 dB/km) within this wavelength window.

To achieve this broader optical amplification, researchers have investigated various approaches, including the use of different dopants and glass hosts. For example, incorporating phosphorous and aluminium into EDFs has successfully extended L-band EDFA operation up to 1628 nm. [51]. Similarly, bismuth- and tellurite-based EDFAs have expanded amplification capabilities to 1610 nm in the L-band [52, 53].

Bismuth has emerged as a particularly promising dopant for ultra-wideband optical amplification. Its broad near-infrared luminescence properties span multiple transmission bands, including O, E, S, L, and U. Researchers have developed a broadband optical amplifier using bismuth- and erbium-co-doped fibres, achieving operation from 1515 to 1775 nm [5]. In the O-band, BDFAs have demonstrated impressive performance, with one study reporting a flat gain of 25 dB over a 40 nm bandwidth from 1320–1360 nm [54]. More recently, an ultra-broadband BDFA providing over 20 dB gain across a 115 nm bandwidth (1330-1480 nm) has been fabricated, covering parts of the O-, E-, and S-bands. [55].

Other rare-earth elements have also shown potential for broadband amplification. Praseodymium (Pr^{3+}) offers emissions in the 1200-1350 nm range that covers O band [56], while thulium Tm^{3+} exhibits transitions in the S- and U-bands [57, 58]. Moreover, the development of novel optical fibers, such as Hollow Core Fibers (HCFs), with low propagation losses beyond the O- and U-bands, further supports the potential for data transmission across wider wavelength windows. Tm-doped

fibre amplifiers (TDFAs) have been explored for telecommunications at 2 µm [59] and wideband holmium-doped fibre amplifiers (HDFAs) for optical communication over 2050–2130 nm [60, 61]. Additionally, ytterbium (Yb^{3+}) ions, which exhibit broad emission from 975 nm to 1200 nm, are promising for data transmission applications. Recent research has demonstrated the effectiveness of wideband YDFAs for 1 µm data transmission in HCFs. This approach leverages the superior advantages of wide frequency bandwidth at shorter wavelengths, potentially opening new avenues for high-capacity optical communications [62, 63]. Furthermore, both Yb^{3+} and Bi^{3+} have shown excellent performance in fibre laser applications. Yb-doped fibre lasers (YDFLs) and bismuth-doped fibre lasers (BDFLs) have been demonstrated impressive lasing capabilities in the 1-1.3 µm range. [64-66]. This dual functionality - as both amplifiers and laser sources - underscores the potential of these rare-earth elements in advancing optical technologies.

To provide a comprehensive overview of the amplification landscape, it's helpful to consider the gain spectra of various rare-earth-doped fibre amplifiers across a broad wavelength range, as shown in Figure 2.13. The gain spectrum from 1 µm to 2 µm encompasses the operational ranges of several key amplifier types, including those based on ytterbium, praseodymium, erbium, bismuth, thulium, and holmium. This wide span of amplification capabilities is crucial for developing next-generation optical communication systems that can utilize an expanded range of wavelengths.

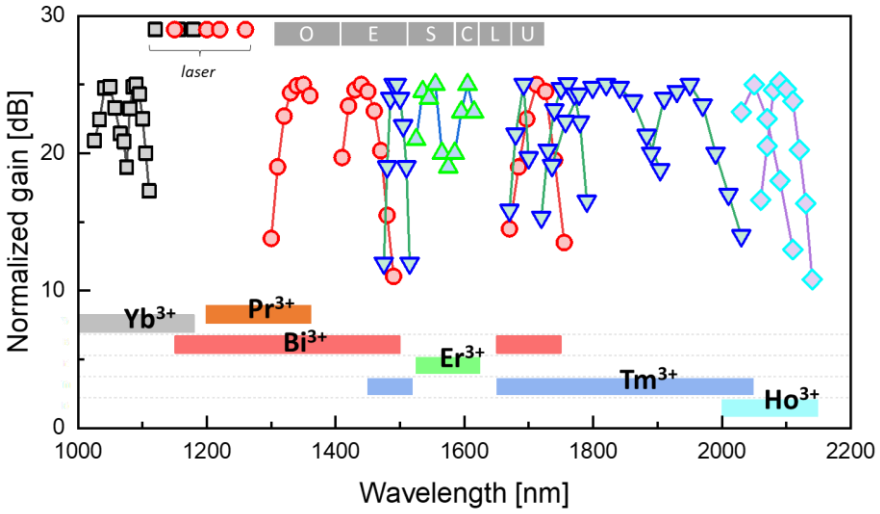

Figure 2.13: Overview of gain spectrum of rare-earth doped fibre amplifiers covering from 1 µm to 2 µm.

Complementing these advancements in doped fibres, researchers are exploring nonlinear amplification techniques. FRAs and fibre optical parametric amplifiers (FOPAs) offer opportunities for high-power optical communication [13, 67]. Hybrid approaches, combining different amplifier types, are also being developed to leverage the strengths of each technology while mitigating

individual limitations. One example is the combination of EDFA with FRA, where EDFA provides high gain in the C-band but relatively lower gain in the L-band. FRA compensates for this deficiency by amplifying light signals via stimulated Raman scattering. FRAs offer the advantage of amplifying signals at various wavelengths by using a pump light wavelength shorter than the signal [68, 69]. Thus, hybrid fibre amplifiers (EDFA + FRA) have drawn huge attention due to the longer span lengths, reduced nonlinearities, larger gain bandwidth and enhanced gain flatness they can provide.

Semiconductor optical amplifiers based on InGaAsP or AlInGaAs heterojunctions offer a unique approach to optical amplification. These devices utilize the recombination of electron-hole pairs to amplify light across a remarkably wide range of wavelengths. This ultra-broad amplification capability makes SOAs particularly interesting for applications requiring flexible wavelength coverage [70]. The key advantages of SOAs include broad amplification bandwidth, compact size, electrical pumping and fast gain dynamics. However, SOAs also face several challenges, such as polarization dependence, relatively lower gain, higher noise levels and nonlinear effects, which have limited their widespread adoption in large-scale optical networks [71]. One way to mitigate these challenges is by integrating SOAs with other types of amplifiers, such as EDFA [72, 73]. This hybrid approach aims to leverage the strengths of each technology while mitigating their individual weaknesses. By combining the ultrabroad bandwidth capabilities of SOAs with the high gain and low noise characteristics of fibre-based amplifiers, significant improvements in optical amplification systems can be achieved, including bandwidth expansion, gain equalization, noise reduction and better polarization management.

To provide a comprehensive overview of the current state of optical amplification technologies, it would be valuable to refer to a summary table of optical amplifiers used in various communication windows, as shown in Table 2. This table includes information on the amplifier type, operating wavelength range, and key advantages or limitations for each technology. This information allows for a quick comparison of different amplification solutions and helps in identifying the most suitable technology for specific application requirements.

Table 2: Summary of optical amplifiers operating in communication window.

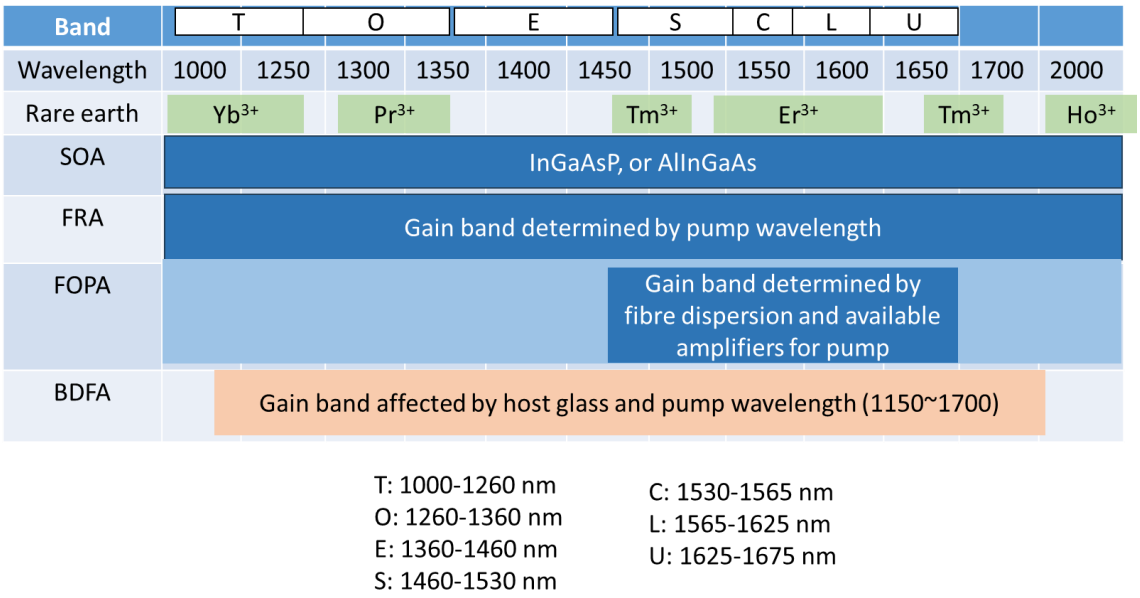

In addition, the data transmission capacity can be also enhanced by exploiting multiple spatial channels in a single optical fibre by SDM technology, various SDM amplifiers (e.g. multicore fibre EDFAs (MC-EDFAs) and few-mode fibre EDFAs (FM-EDFAs)) have been extensively investigated [74]. Especially in few-mode fibre (FMF) based SDM transmission systems, differential modal gain (DMG) is important to avoid power deviation between spatial channels and several techniques have been used to control DMG in FM-EDFAs, e.g. by optimizing the pump launch and using improved EDF with tailored refractive index and Er^{3+} ion concentration [75]. Mode dependent loss (MDL) and differential group delay (DGD) are the other challenges in haul-long SDM transmission systems employing FM-EDFAs. MDL increases the channel leakage loss which leads to a reduced transmission distance while DGD increases the memory of the channel leading to the more complex Multiple Input Multiple Output (MIMO). Thus, various MDL and DGD compensation techniques are required for successful amplified SDM transmission systems.

2.8 Conclusion

In this Chapter, I have discussed the background knowledge for understanding the research presented in this thesis. I began by examining the principles of linear optical amplification, introducing key concepts such as gain, NF, ASE, and PCE. These concepts are crucial in guiding the design and optimization of amplifiers and provide the theoretical framework for many practical considerations in the subsequent chapters. I then explored the spectroscopic characteristics of rare earth ions, focusing on how their 4f energy states are formed and the mechanisms behind parity-forbidden 4f → 4f transitions. The spectroscopic properties of Yb-doped fibres were investigated in

detail, with comparisons to Er^{3+}. Various aspects, including pumping schemes and multistage amplifiers, were also discussed. Finally, I summarized the advancements in optical amplifiers, highlighting the significant improvements in performance over the past few decades. These discussions form the foundation for the research and analyses presented in the following chapters.

Chapter 3 Development of Gain Flattening Filters (GFFs)

3.1 Introduction

Densely spaced wavelength-division multiplexing (WDM) is recognized as one of the most effective technologies for achieving high-data transmission over optical fibres, necessitating the integration of optical amplifiers. However, amplifiers, such as EDFAs exhibit nonuniform gain profiles and saturation characteristics. These issues arise from the stimulated emission of erbium ions, which amplifies input signals but produces a gain spectrum that is not uniform. This uneven gain across different channels can lead to power imbalances among optical signals of varying wavelengths, ultimately reducing transmission distance and narrowing the effective wavelength range.

To mitigate these issues, it is crucial for amplifiers to maintain a flat gain spectrum across the signal waveband. This is typically accomplished by employing spectral filters, specifically GFFs. GFFs are optical filters designed with a loss profile that inversely matches the amplifier's gain spectrum, thereby flattening the overall gain and ensuring more uniform signal amplification across all channels. Various technologies have been developed and proposed for use in GFFs. These include etalon filters [76], dielectric multilayer thin-film filters [77, 78], long-period fibre gratings [79, 80], short-period fibre Bragg gratings [81], Mach-Zehnder silica waveguides [82, 83], and split-beam Fourier filters [84]. Each of these technologies offers unique advantages in tailoring the loss profile to achieve the desired gain flatness, making them integral to modern optical communication systems that rely on WDM for efficient, high-capacity data transmission.

In this chapter, I discuss three key technologies utilized as GFFs in WDM systems: long period fibre gratings (LPFGs), dielectric multilayer thin-film filters, and waveshapers based on liquid crystal on silicon (LCOS) technology. In section 3.2, I focus on LPFGs as efficient spectral filters or other functional devices to improve the gain performance of amplifiers (e.g. mode scramblers). In subsection 3.2.1, I investigate SMF-based LPFGs as low-loss spectral filters with the potential to serve as GFFs, thereby flattening and broadening the gain bandwidth of the multi-stage amplifiers discussed in subsequent chapters. This subsection begins with an overview of the fundamental principles of LPFGs, including phase matching and resonance conditions, the relationship between bandwidth and resonant wavelength, and the influence of physical effects such as geometrical deformation and the photo-elastic effect. I then present simulations of the phase match condition and transmission spectra for two types of LPFGs—conventional SMF-LPFGs and phase-shifted LPFGs—using COMSOL and RSoft BeamPROP software. Following the theoretical discussion, a series of preliminary experiments that demonstrate the practical implementation of LPFGs are

presented in subsection 3.2.1.2. This includes the use of 3D printing and arc-induced periodic tapering technologies to inscribe LPFGs operating at 1.5 µm and 1 µm on SMFs. Additionally, I explore the application of LPFGs on TMFs as mode scramblers, which are critical for mode-division multiplexing (MDM) systems in subsection 3.2.2.

Finally, I discuss two alternative commercially available spectral filtering techniques: dielectric thin-film filters and programmable waveshapers in section 3.3 and 3.4. I discuss the working principles of each technology and evaluate their performance as spectral filters within amplifier systems.

3.2 Long period Fibre Gratings (LPFG)

LPFGs are optical devices with periodic structures on the scale of hundreds of micrometres, that are widely utilized for coupling light between different guided modes. These devices have been extensively studied for their applications in band-rejection filters [85, 86], optical fibre polarizers [86], mode scramblers [87], and optical sensors [88] etc. A particularly significant application of LPFGs is their use as GFFs in amplifiers due to their low insertion loss (IL), minimal back-reflection, and compact design.

In this section, I explore how the transmission spectra of LPFGs can be precisely engineered to achieve accurate gain equalization in amplifiers and to function as mode scramblers in MDM systems.

3.2.1 Single-Mode Fibre LPFGs as Spectral Filters

3.2.1.1 Simulations

SMF based LPFGs couple light from a fundamental core mode to cladding modes after passing through an LPFG with a period of Λ and a length of L, as shown in Figure 3.1.

Figure 3.1: Schematic diagram of a SMF-LPFG.

In principle, energy transfer between guided core mode and forward propagating cladding modes in a SMF occurs only if the resonant condition of the LPFG is satisfied. The associated phase matching condition is given by:

$$\beta_{co} - \beta_{cl,m} = 2\pi/\Lambda \tag{3.1}$$

where β_{co} and $\beta_{cl,m}$ represent the propagation constants of the core and mth order cladding mode, respectively. For mode coupling between the core mode and cladding modes, the resonant wavelength λ_{res} and bandwidth $\Delta\lambda$ [85] can be further expressed by:

$$\lambda_{res} = \left(n_{eff}^{co} - n_{eff}^{cl,m}\right) \cdot \Lambda \tag{3.2}$$

$$\Delta\lambda \propto \lambda_{res}^2/[L \cdot \left(n_{eff}^{co} - n_{eff}^{cl,m}\right)] \tag{3.3}$$

Where $L = N \cdot \Lambda$ is the grating length and N is the number of grating periods. n_{eff}^{co} and $n_{eff}^{cl,m}$ represent the effective refractive indices of core mode and mth cladding mode, respectively.

In order to quantitatively investigate the mode coupling between core and cladding modes, I modelled the impact of a periodic modulation in a SMF. Given the LPFG fabrication technology utilized in the subsequent experiment (i.e., 3D printed technology), according to ref. [89-91], two physical effects (i.e. geometrical deformation and the photo-elastic effect) are considered in my simulations. The geometrical deformation describes the physical deformation of the fibre cross-section when an external load is applied to an optical fibre and the photo-elastic effect represents the refractive index change resulting from strain-induced glass density changes. When considering the micro-bending effect (geometrical deformation), according to *Roark* [92], coupling efficiency between propagation modes is proportional to the curvature power spectrum in a fibre and displacement $y(z)$ of the fibre can be expressed by the following equation when applying a load on a fibre:

$$y(z) = -\frac{W}{8EI\beta^3} e^{-\beta z}(cos\beta z + sin\beta z) \tag{3.4}$$

where W is the applied load, E is the average Young modules of the fibre, I is the moment of inertia of the cylindrical beam, $\beta = (\frac{E_e}{4EI})^{1/4}$ and E_e is the Young modules (1.8×10^{10} Pa is used for optical fibre and 1.3×10^{9} Pa for the fibre polymer coating) of elastic materials that used to apply a load on the fibre.

In relation to the photo-elastic (strain-optic) effect, when a load (F) is applied to the fibre in the Y-axis, the total refractive index change due to the stress at the point (x, y) is equal to the stress-induced birefringence and is given by [90, 93]:

$$(\frac{\Delta n}{n})^S = (\frac{\Delta n_x}{n})^S - (\frac{\Delta n_y}{n})^S = -\frac{n_0^2}{2}(q_{11} - q_{12})(\sigma_x - \sigma_y)_{x,y} \tag{3.5}$$

$$\sigma_x(x,y) = \frac{-2F}{\pi L}\left\{\frac{x^2(b+y)}{[x^2+(b+y)^2]^2} + \frac{x^2(b-y)}{[x^2+(b-y)^2]^2} - \frac{1}{2b}\right\} \quad (3.6)$$

$$\sigma_y(x,y) = \frac{-2F}{\pi L}\left\{\frac{(b+y)^3}{[x^2+(b+y)^2]^2} + \frac{(b-y)^3}{[x^2+(b-y)^2]^2} - \frac{1}{2b}\right\} \quad (3.7)$$

where L is the total length of the fibre, b is the radius of the fibre, q_{11}=3.84×10^{-12} m^2/kg, q_{12}=2.70×10^{-11} m^2/kg are the Pockels piezo-optic coefficients, that can be calculated from Young's modulus and the Poisson ratio. The coordinate system is defined such that the fibre axis lies along the Z-axis, the load is applied in the transverse Y-direction (vertical), and the X-axis represents the horizontal transverse direction. The position (x, y) denotes a point within the fibre cross-section.

With a sinusoidal modulation of the refractive index, the spatial distribution of the core refractive index over the length of the fibre in the grating zone can be expressed as:

$$n_0(z) = n_0 + \Delta n \cdot cos(\frac{2\pi}{\Lambda} z) \quad (3.8)$$

where Δn is the refractive index modulation of the grating.

First of all, I calculated the effective refractive indices of LP_{01} core mode and LP_{11}, LP_{12}, LP_{13} cladding modes in conventional SMF (with core diameter of 8 μm and a relative refractive index difference of 0.005) at different wavelengths using Finite Element Method by COMSOL software. The grating periods were further estimated at different wavelengths according to Equation (3.2). Figure 3.2 shows the relationship between the resonance wavelengths and grating periods. It exhibits a positive correlation between grating period and wavelength. When the grating period is 613 μm, LP_{01} core mode couples to LP_{11}, LP_{12} and LP_{13} cladding modes with resonant wavelength of 1518 nm, 1555 nm and 1626 nm, respectively.

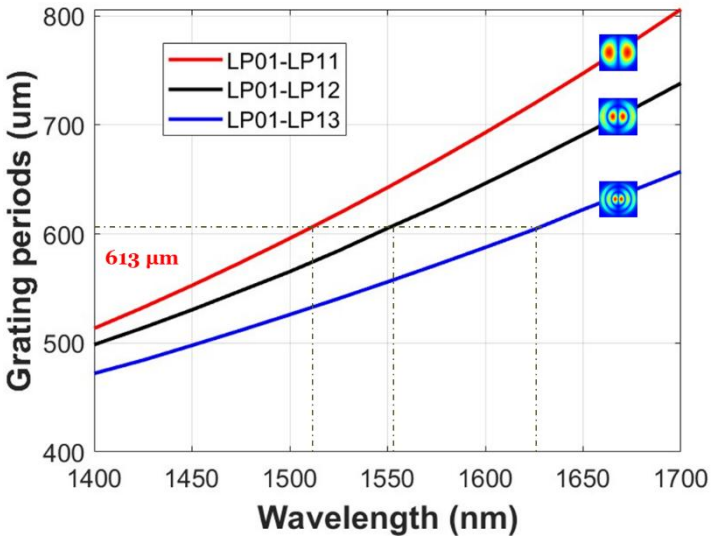

Figure 3.2 Relationship between the resonance wavelengths and grating periods.

Then, I investigated the mode coupling and monitored the transmission spectrum of a conventional SMF-LPFG with a uniform grating period of 613 μm using a finite difference beam propagation method (RSoft BeamPROP). According to Equation (3.5) and (3.8), the effective refractive index modulation (Δn) was estimated to be approximately 1.5×10^{-6} and the displacement of the fibre is calculated to be around 0.02 μm when 6.3 N load is applied across 40 grating periods. The calculated transmission spectrum of a conventional SMF-LPFG is shown in Figure 3.3, exhibits three resonant dips at 1512 nm, 1553 nm and 1636 nm, corresponding to the mode coupling from fundamental LP_{01} mode to LP_{11}, LP_{12} and LP_{13} cladding modes, respectively. This result is roughly consistent with the result calculated by COMSOL shown in Figure 3.2. The transmission associated with these mode couplings are -0.3 dB, -1.5 dB and -3.3 dB, indicating that coupling efficiency increases with higher-order cladding modes.

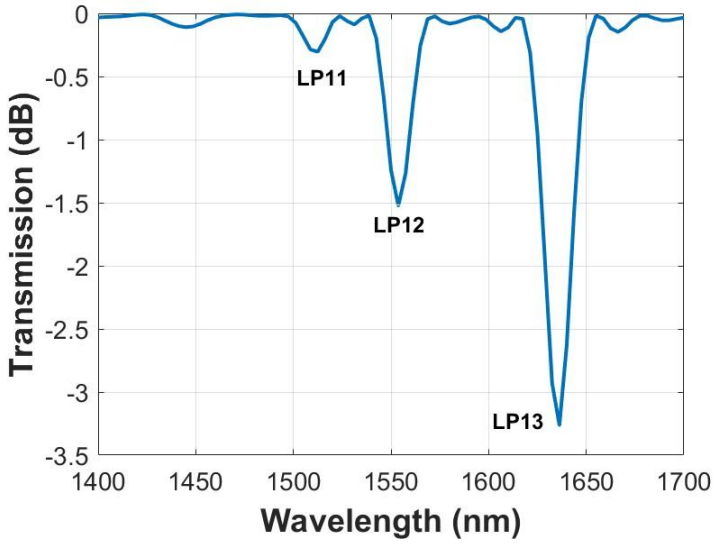

Figure 3.3: Calculated Transmission spectrum of a conventional SMF-LPFG.

A conventional SMF-LPFG usually has a single Gaussian-shaped filter shape within a bandwidth of ~20 nm, making it difficult to flatten the gain spectrum of an amplifier that has multiple non-uniform peaks. One approach to obtain a GFF suitable for the amplifier is to connect multiple LPFGs in series. However, this method is not ideal for applications that require compact modules. An alternative method for achieving a broadband GFF is to use a phase-shifted LPFG. This type of LPFG generally consists of two LPFGs with identical periods and induced index changes, separated by a phase-shifted region in the middle. The separation distance (ΔL) between the two gratings ranges from 0 to Λ, as depicted in Figure 3.4. Since the two grating sections have identical periods, the cladding modes that satisfy the phase-matching condition within the band remain consistent across both sections.

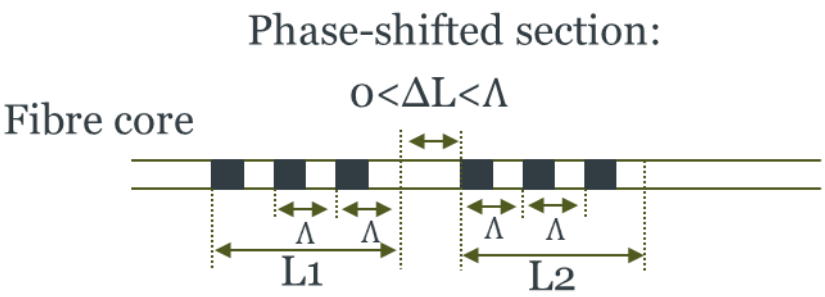

Figure 3.4: Schematic diagram of a phase-shifted LPFG.

In the analysis of phase-shifted LPFGs (ΔL=0), the two LPFGs (LPFG1 and LPFG2) are treated as a single grating with a total length L=L1+L2. The phase shift section (Φ) corresponds to a phase change of 2πΔL/Λ. A parameter q is introduced to measure the position of the phase shift section within the LPFG, defined as:

$$q = x/(L1 + L2) \tag{3.9}$$

When q =0, the phase shift is located at the centre of the LPFG, while q =±0.5 indicates that the phase shift is positioned at one of the ends, reducing the phase-shifted LPFG to a conventional LPFG.

Figure 3.5 shows the calculated transmission spectra for an LPFG with various phase shifts (L=24.6 mm, Φ=0, 0.5π, π, 1.5π). When there is no phase shift in the LPFG, the resonant peak is located at 1553 nm. When a phase shift (π) section is introduced at the centre of the LPFG, two peaks appear at 1544 nm and 1568 nm, symmetrically located 24 nm apart around the central wavelength (yellow curve). This phenomenon results from the introduction of the π phase, which converts destructive interference into constructive interference at the phase-matching wavelength. When the phase shift is not equal to an integral multiple of π, the bandwidth remains relatively constant and the maximum transmission loss at the main peak decreases, while the loss in the side lobe increases, while the spectral response becomes asymmetrical.

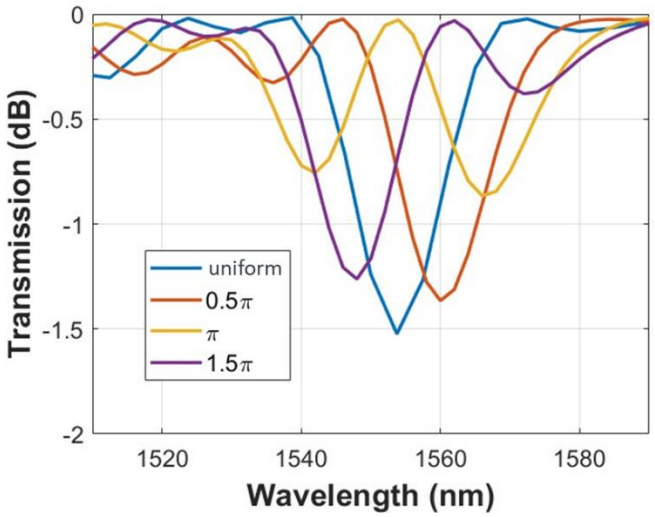

Figure 3.5:LPFG transmission spectrum for different phase shifts (L=24.6 mm, Φ=0, 0.5π, π, 1.5π) with equal-length sections (q=0).

Specifically, a phase shift of less than π (orange curve) causes the spectrum to shift towards longer wavelengths, while a phase shift greater than π (purple curve) results in a shift towards shorter wavelengths comparing to the uniform grating (blue curve). Figure 3.6 demonstrates this effect by displaying the transmission spectrum of a 0.9π-shifted LPFG for different phase locations (q=±0.1, ±0.15, ±0.2).

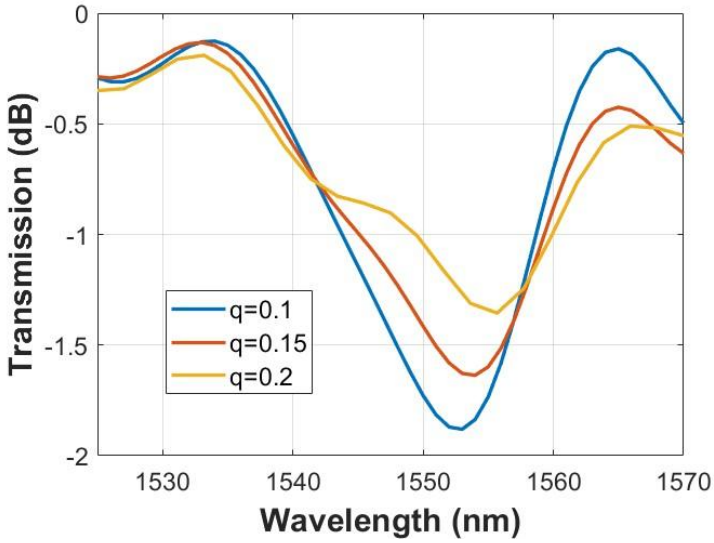

Figure 3.6: Transmission for different phase locations (Φ=0.9π, L=24.6 mm, q=±0.1, ±0.15, ±0.2).

This ability to fine-tune the LPFG spectrum by introducing a phase shift makes it suitable for applications like GFF. For example, consider a GFF designed for a single-stage C-band EDFA, with a 4.6 m EDF under 3 dBm total input power and 100 mW pump power, resulting in an average gain of 16 dB with a gain variation of approximately 2 dB. The target filter's spectrum derived from this

EDFA's gain profile can be divided into two components, resembling those of a conventional LPFG operating in 1528-1538 nm and a phase-shifted LPFG operating in 1538-1565 nm, as illustrated by the blue curve in Figure 3.7. In this design, the conventional LPFG has a grating period of 568 µm with 80 periods, and its peak is located at 1532 nm. The phase-shifted LPFG has a grating period of 615 µm, divided into sections of 7 and 42 periods, with a phase shift of 0.96π. By cascading these two LPFGs, which are positioned far apart, a filter spectrum closely resembling the target filter can be achieved. The difference in transmission between the designed filter and the target filter remains within 0.2 dB across the 1530-1562 nm wavelength range. The maximum attenuation of this filter is 2.4 dB at 1528 nm and 1557 nm, and it can be further fine-tuned by increasing the refractive index modulation depth to achieve a higher attenuation.

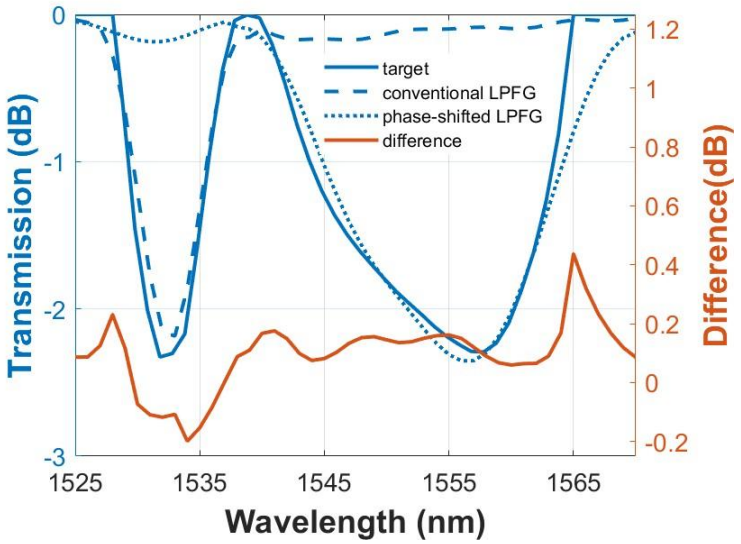

Figure 3.7: Designed C-band GFF transmission spectra.

Based on the investigations conducted on the 1.5 µm GFF designed for a C-band EDFA, a similar design approach can be applied to a 1 µm GFF for wideband YDFA. The phase-matching condition for the SMF-LPFG at 1 µm was first calculated using COMSOL, with fibre parameters based on HI1060 fibre, which has a core diameter of 6 µm and a numerical aperture (NA) of 0.14. Figure 3.8(a) shows the mode coupling from fundamental LP_{01} core mode to LP_{11}, LP_{12}, LP_{13}, LP_{14}, LP_{15}, LP_{16} cladding mode. As the order of the cladding mode increases, the spacing between resonant wavelengths widens for a fixed grating period.

For a dual-stage YDFA operating within the 1025-1075 nm range (where the first stage consists of 3 m of YDF with 980 nm forward pumping at 300 mW, and the second stage consists of 9 m of YDF also forward pumped at 980 nm with 300 mW, and a total input power of -12.9 dBm), I designed a phase-shifted LPFG with a grating period of 252 µm as the GFF for this dual-stage YDFA. The grating was tailored to couple the fundamental core mode (LP_{01}) to the LP_{16} cladding mode, chosen for its

resonant wavelength, which is well separated from other mode couplings, thereby minimizing spectral interference. The phase-shifted LPFG was divided into sections of 5 and 35 periods, with a phase shift of 1.1π. The transmission spectrum of this phase-shifted LPFG closely matches the target filter profile within the 1027-1058 nm range, with the difference between the target filter and the phase-shifted LPFG being less than 1 dB in this wavelength region, as shown in Figure 3.8(b). However, the difference increases to approximately 2 dB at 1060 nm, primarily due to the presence of side lobes in the grating at this wavelength under high modulation depth.

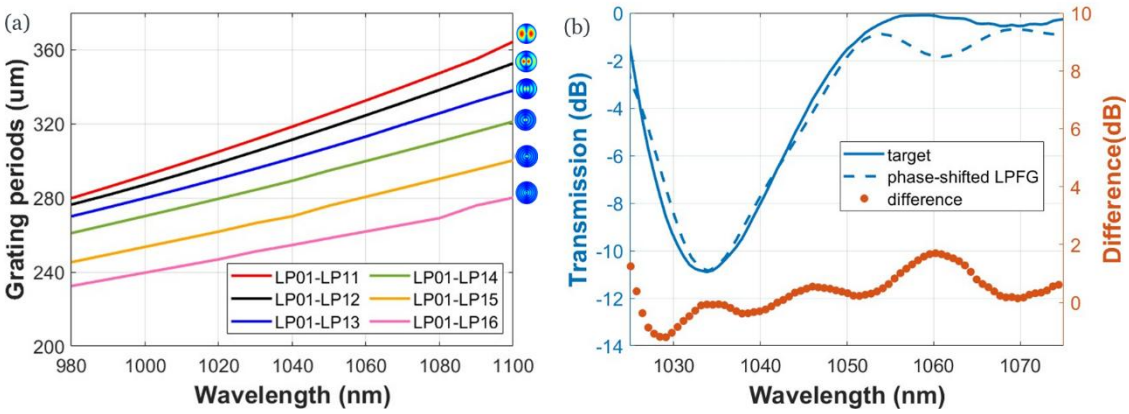

Figure 3.8: (a) Relationship between the resonance wavelengths and grating periods at 1 μm; (b) designed 1 μm GFF transmission spectra.

3.2.1.2 Fabrication and Measurements

Various techniques have been developed to inscribe LPFGs, including UV radiation on photosensitive fibres, CO_2 laser irradiation, electric arc discharge and periodic micro-bends [85, 94-96]. In this experimental section, I will introduce two fabrication methods for LPFGs that are potentially suitable for GFF in amplifiers: mechanically induced 3D-printed LPFGs and arc-induced tapered LPFGs.

3.2.1.2.1 Mechanically induced 3D-printed LPFGs

By taking advantage of affordable and highly flexible 3D printing technology, different lengths of LPFGs were designed using an OpenSCAD software and fabricated by the Stereolithography (SLA) process [97]. In SLA, an object is created by selectively curing a polymer resin in a layer-by-layer fashion using an ultraviolet laser. Here, Dr Kerrianne Harrington has helped me the CAD design and an external 3D printing service was used. In my sample fabrication, a Formlabs Grey Pro Resin is used, which is a photosensitive polymer resin that offers high precision, fine details, moderate elongation and low creep at a minimum layer height of 50 μm. Figure 3.9(a) shows an example of CAD designs with a periodic triangular corrugated surface. The dimensions of the sample are 50 mm (length)×16 mm (width)×3 mm (height) (Note that my supervisor (Dr. Yongmin Jung) first tried

a periodic rectangular corrugated structure but no grating resonance peaks were observed. In order to enhance the photo-elastic effect when applying a compressive force on the fibre, we then modified our design to a triangular corrugated structure). Figure 3.9(b) shows a cross-sectional microscope image of the fabricated LPFG sample. Although there is a slight smoothening effect, a clear periodic triangular shape is observed. The individual layer lines are also visible from the side view of the 3D printed part. The measured average height of the vertices was ~230 µm. Based on the calculated grating periods for the SMF-LPFG, several samples with varying grating pitches were fabricated, including 600 µm, 620 µm, 700 µm, and 740 µm. Additionally, an FMF-LPFG with a pitch of approximately 1173 µm was produced, which will be discussed in the following section as a mode scrambler.

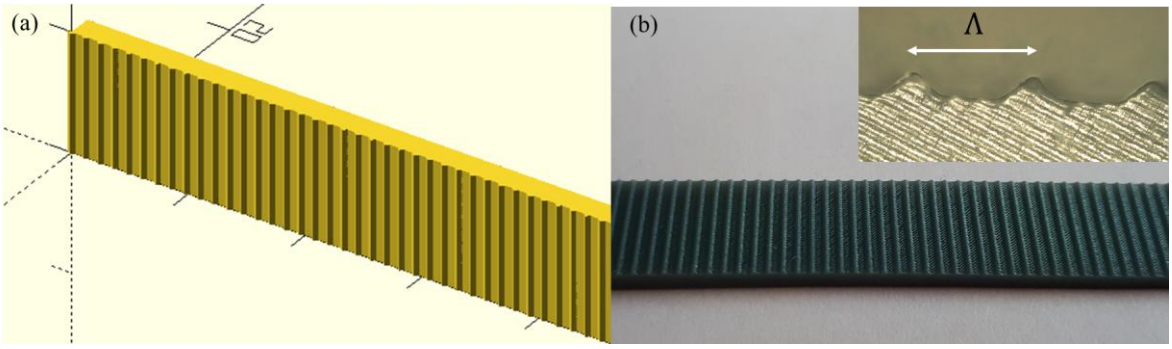

Figure 3.9: 3D printed LPFG device: (a) CAD design using an OpenSCAD software and (b) fabricated sample images (inset: microscope image).

The transmission spectrum of the 3D-printed gratings was measured using a superluminescent diode (Thorlabs, S5FC1050P) as the input source, with the output analysed by an optical spectrum analyser (OSA). The SMF was sandwiched between a flat metal plate and the 3D printed LPFG and a compressive force was applied by adding a static load to the top plate, as shown in Figure 3.10.

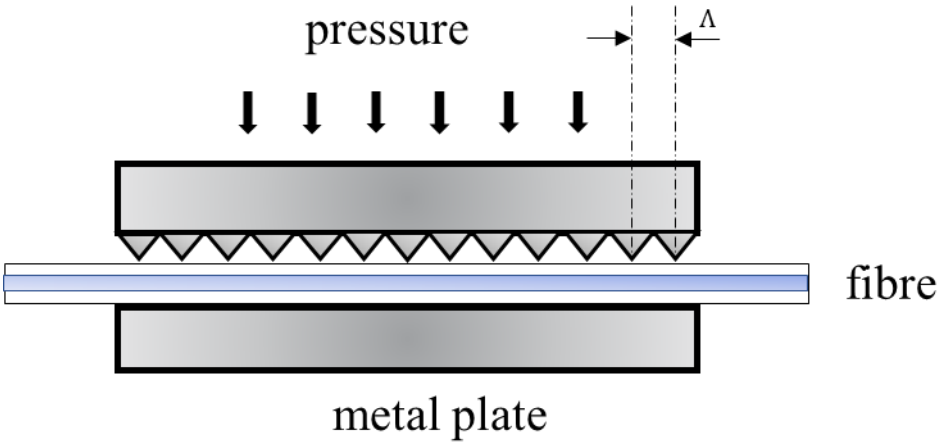

Figure 3.10: Setup of the mechanically induced 3D printed LPFGs.

Figure 3.11 shows the transmission spectra of SMF-LPFGs with grating periods of 600 µm, 620 µm, 700 µm and 740 µm. The three resonant dips for the grating period of 600 µm locating at 1490 nm, 1531 nm and 1619 nm correspond to mode coupling from the LP_{01} core mode to the LP_{11}, LP_{12}, LP_{13} cladding modes, respectively. This measurement is almost consistent with simulations in Figure 3.2. Thus, according to Figure 3.2, the shortest resonant wavelength for each of these four LPFGs, i.e., 1490, 1549, 1603 nm, and 1631 nm (with grating period of 600 µm, 640 µm, 700 µm and 740 µm), correspond to the coupling from LP_{01} fundamental mode to LP_{11}, demonstrating that the resonant wavelength shifts to longer wavelengths as the grating period increases.

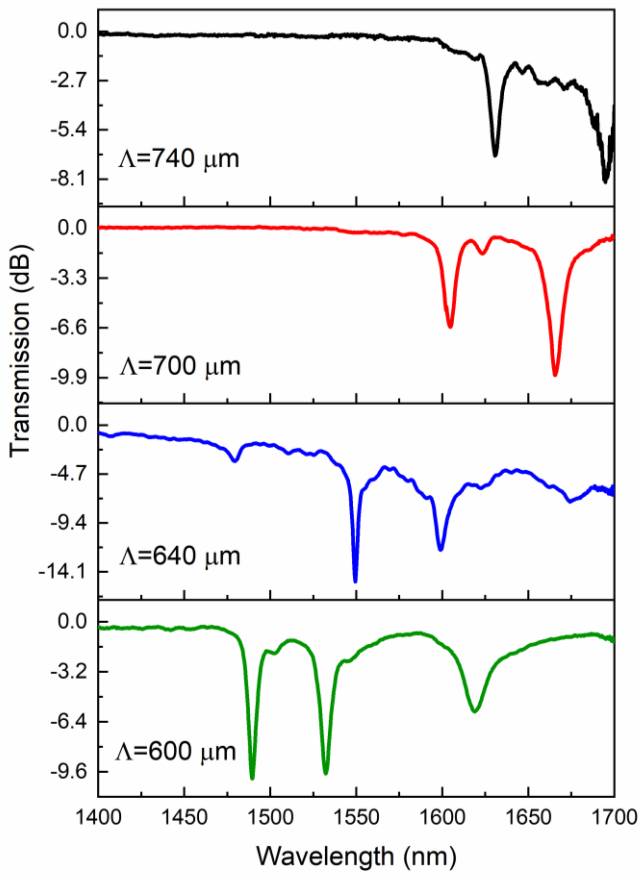

Figure 3.11 Transmission spectra of LPFGs inscribed in SMF with grating period of 600 μm, 640 μm, 700 μm and 740 μm.

Figure 3.12 shows the measured filter spectra of a 600 μm-grating period for different applied loads from W_1 to W_5. Stronger mode coupling can be obtained by applying a heavy load. The out-of-band loss of this filter is typically less than 0.3 dB but it slightly increases when the applied load increases from W_1 to W_5. This phenomenon arises from the increased microbend loss that is induced at each V-groove in a 3D printed LPFG when the applied load on the fibre increases. The actual weight value from W_1 to W_5 was not measured in this experiment due to the too much pressured required to achieve a high attenuation dip.

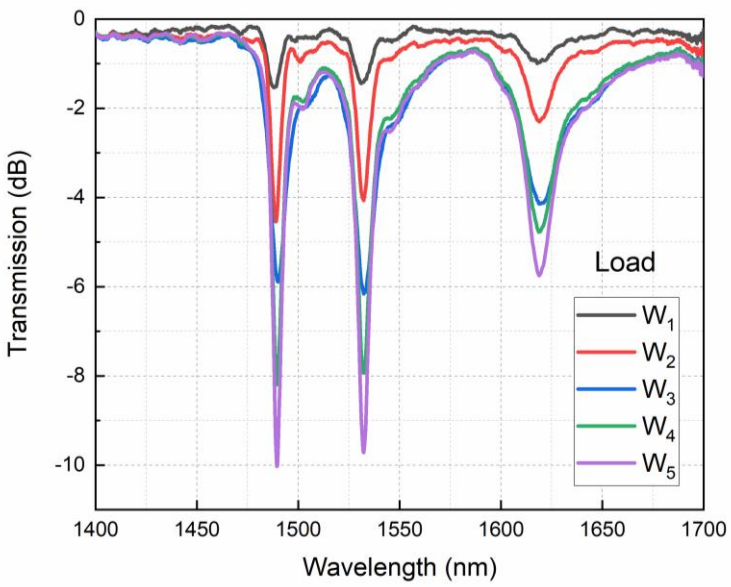

Figure 3.12 Measured filter spectra with applied load increasing from W_1 to W_5 ($\Lambda = 600$ μm).

The polarization dependence of this SMF-LPFG based spectral filter was also characterized. Figure 3.13 shows the transmission spectra with two orthogonal polarization states of the input beam. The resonant wavelength shift is less than 1 nm and the maximum polarization-dependent transmission loss is less than 0.2 dB.

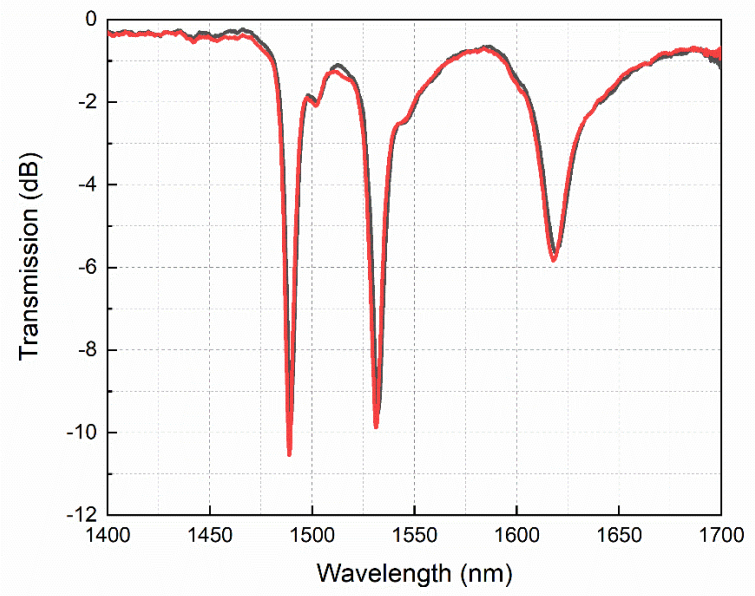

Figure 3.13 Transmission spectra with two orthogonal polarization states of the input broadband beam

By serially cascading these multiple SMF-LPFGs or precisely design a phase-shift LPFG, more complex filter spectra can be readily achievable as in-line spectral filters for efficient gain flattening for fibre amplifiers. One potential issue of this 3D printed SMF-LPFG (mode coupling between core and cladding modes) is that it requires a quite strong perturbation (i.e. heavier mass) to achieve

efficient mode coupling. To be used as a practical device, however, it may be necessary to increase the mode coupling efficiency of the current device by exploring other approaches (e.g. changing the cladding diameter of the fibre, increasing the depth of the V-grooves or trying other elastic materials that have larger Young's modulus).

3.2.1.2.2 Arc-induced tapered LPFGs

Given the limitations of 3D printing technology's resolution (~50 µm), it was not possible to fabricate the LPFGs with grating pitches smaller than 300 µm. To overcome this, a periodic tapered LPFG was developed using a commercial fusion splicer machine (ARCMaster FSM-100P+, Fujikura), which has a maximum moving range of +/−18 mm and a precision of 0.01 µm. A new tapering program was created and saved in the splicer's program store by using the special function of the splicer. The program consists of three main steps: The first two steps involve tapering the fibre to create the down-taper and up-taper sections. During the arc discharge process, the fibre ends are stretched by the ZL and ZR motors, forming a taper at the discharge point. In the third step, the fibre is advanced by a set grating pitch (e.g., 350 µm) using the SWEEP motor, positioning it for the next taper. As the unjacketed fibre is fed into the heat zone from the right side by the ZR motor at a constant speed of 0.04 µm/ms, it is simultaneously pulled from the left side by the ZL motor at a variable speed. The difference in feeding and pulling speeds determines the taper ratio. According to material conservation, the amount of glass fed into the heat zone must equal the amount pulled out, so the pulling speed is calculated using the equation $V_1 = (D_1/D_2)^2 V_2$, where D_1 and D_2 are the cladding diameter of fibre and the local diameter of the taper, respectively, as shown in Figure 3.14(a). By precisely controlling these speeds, the desired taper can be achieved. Figure 3.14(b) provides a microscope image of the LPFG inscribed with periodic tapering, showing a grating pitch of 340.97 µm, with each taper having a waist diameter of 111.86 µm and a length of approximately 200.00 µm.

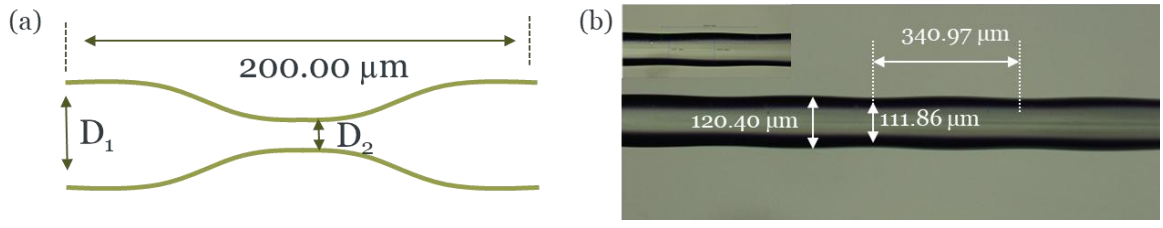

Figure 3.14: (a) schematic diagram of the tapered section; (b) image of the LPFG inscribed by periodically tapering a SMF.

Figure 3.15 shows the transmission spectrum of the inscribed LPFG during grating inscription. Four resonant dips were observed in the transmission spectrum within 980-1150 nm wavelength range, located at 1001 nm, 1028 nm, 1070 nm, and 1137 nm. As the number of grating periods (or tapers)

increased, the attenuation of each dip gradually increases, with the maximum attenuation reaching up to 20 dB at 1000 nm for 30 grating periods. The polarization dependence of this 1 μm-LPFG based spectral filter was also characterized for 40 periods of LPFGs. Figure 3.15(b) shows the transmission spectra with two orthogonal polarization states of the input beam. The resonant wavelength shift is less than 0.1 nm and the maximum polarization-dependent transmission loss is less than 1 dB. Considering the resolution of the splicer machine (0.01 μm) and current successfully fabricated LPFGs using arc-discharge technology [98, 99], we estimate that the shortest achievable grating pitch with this method could be approximately 150 μm.

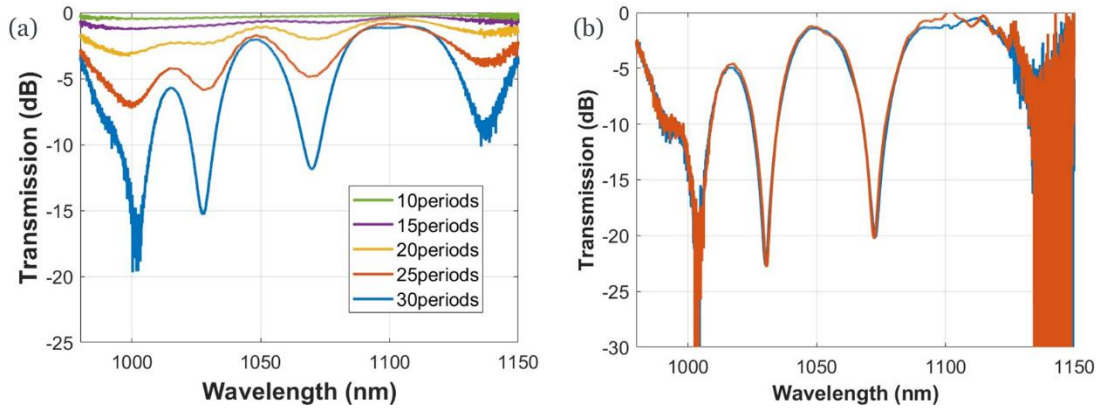

Figure 3.15: (a) Transmission spectrum with a pitch of 340.97 μm while the number of grating periods increases from 10 to 30; (b) Transmission spectra with two orthogonal polarization states of the input broadband beam.

3.2.2 Few-Mode Fibre LPFGs as Mode Scramblers

Mode division multiplexed (MDM) technology [9, 100, 101] has been shown to be a promising approach to increase the transmission capacity of optical fibre with substantial theoretical and experimental work on FMF and multimode (MM) fibre systems conducted over the past decade or so. MDL and DGD are two key parameters in MDM transmission systems and ensuring low net values of both is critical in order to prevent capacity loss/outage and to reduce the computational complexity of the MIMO digital signal processing required at the receiver [102, 103].

Recently, it has been reported that strong mode coupling [104, 105] is highly effective in reducing both the impact of MDL and accumulated DGD and various fibre optic mode scramblers (i.e. devices for inducing effective mode coupling amongst all the guided modes in an optical fibre) have been considered including those based on LPFGs [106-108], phase plates [109], microbends [110] and offset fibre splices/launches [111]. LPFG solutions are particularly attractive, representing one of the most effective ways of promoting strong mode coupling with low loss in optical fibres. There have been several attempts to apply LPFGs in MDM transmission systems (both step-index and

graded-index FMFs) [106-108]. However, it remains a challenge to simultaneously meet all of the performance requirements of a practical mode scrambler in terms of wide bandwidth operation, low IL and a low MDL. It should be noted that LPFGs generally offer a limited optical bandwidth (typically ~10 nm) due to the strict phase matching conditions between modes and multiple LPFGs with different grating pitches are usually required to obtain sufficiently wide bandwidth mode mixing in FMFs. It is to be appreciated that the narrow bandwidths (or strict phase matching conditions) of LPFGs are essentially due to constructive interference from multiple beams diffracted by the periodic refractive index modulation and that greatly increased bandwidths can be achieved simply by reducing the number of these modulation periods (i.e. by shortening the length of the grating). This comes though at a cost in terms of coupling strength. Fortunately though, for mode scrambler applications, only moderate coupling between modes is required i.e. ~50-60% (not >99% as required for many other LPG devices such a mode converters), providing considerable opportunity to design gratings to enable low loss mode coupling devices with appreciable optical bandwidth (~100's nm).

Here I systematically analyse how the optical bandwidth of the LPFG varies with design and propose a short grating device for low loss, low MDL and wideband mode scrambler for MDM transmission system based on FMFs. With a commercially available 3D printing technology, any corrugated structures can be readily fabricated in a low cost and highly flexible manner and 3D printed mechanical induced fibre gratings are examined in my experiment as a convenient means for creating various lengths of gratings in a FMF. As an exemplary demonstration, I experimentally demonstrate a mode scrambler for two mode group fibre supporting LP_{01} and LP_{11} modes and wideband mode coupling was confirmed with a low IL and a low MDL.

3.2.2.1 Simulations

Similar to the mode coupling in SMF-LPFGs (i.e. mode coupling between core mode and cladding modes), TMF based LPFGs couple light from a fundamental core mode (LP_{01}) to LP_{11} core mode. According to Equation (3.2) and (3.3), the bandwidth of a LPFG is proportional to the resonance wavelength and inversely proportional to the grating length and the effective index difference between two spatial modes. First of all, I calculated the effective refractive indices of the LP_{01} and LP_{11} modes in the TMF by Finite Element Method with Comsol software. A simple step-index TMF (core diameter of 19.8 μm and a relative refractive index difference of 0.005) that I have in experiments was used in the modelling. The resonant wavelength and bandwidth factor are further estimated according to Equation (3.2) and (3.3). As shown in Figure 3.16(a), the effective refractive indices of the LP_{01} and LP_{11} modes decrease with the increase of wavelength while their difference increases. Thus, the resonant wavelength decreases with the grating period according to Equation

(3.2) and the resonant wavelength locates at 1550 nm when the grating period is 1226 µm. Figure 3.16(b) shows the dependence of the bandwidth factor on the resonant wavelength when the grating length is 10 cm. It is clearly seen that the grating bandwidth increases with resonance wavelength.

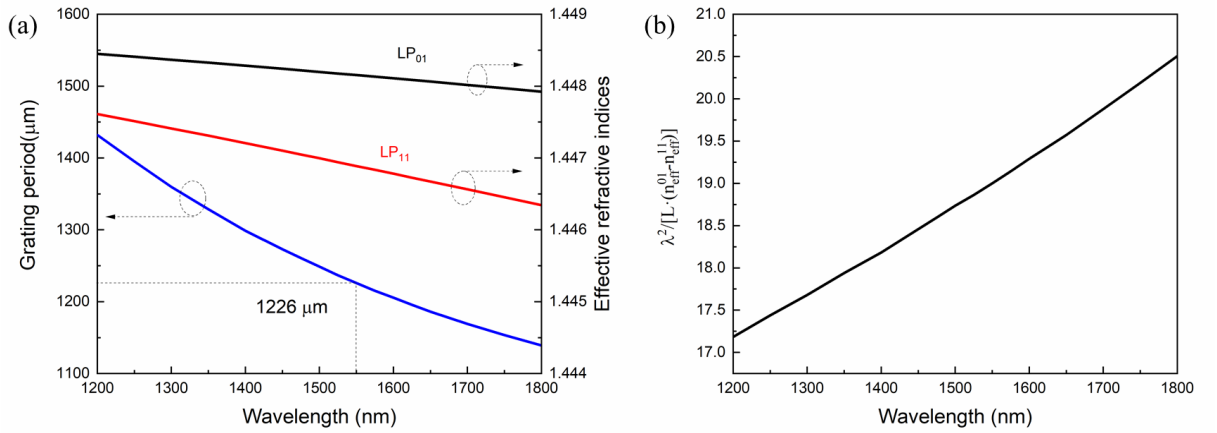

Figure 3.16: (a) The relationship between wavelength and grating period and effective refractive indices of LP_{01} and LP_{11} modes; (b) Dependence of the bandwidth and wavelength.

Then, I have investigated the mode coupling and bandwidth change with grating length using a finite difference beam propagation method (RSoft BeamPROP). The grating period (Λ) of the TMF based LPFG was selected to be 1226 µm to match the phase matching condition between the LP01 and LP_{11} modes at 1550 nm. According to Equation (3.5) and (3.8), the effective refractive index modulation (Δn) is estimated to be ~1×10^{-4} and the displacement of the fibre core is calculated to be ~0.25 µm when 6.3 N load is applied with 10 grating periods to achieve 60% mode coupling. Figure 3.17 shows the beam propagation distribution at the resonant wavelength. Under initial pure LP_{01} mode excitation, the power in the fundamental mode is gradually transferred on propagation along the grating to the LP_{11} mode. Around 60% mode coupling efficiency is observed after propagation through 1.226 cm of fibre grating. As shown in Figure 3.18, Under LP_{11} mode excitation, the same coupling efficiency can be obtained from the LP_{11} to the LP_{01} mode and that is why the LPFGs can be used as an effective mode scrambler for FMFs.

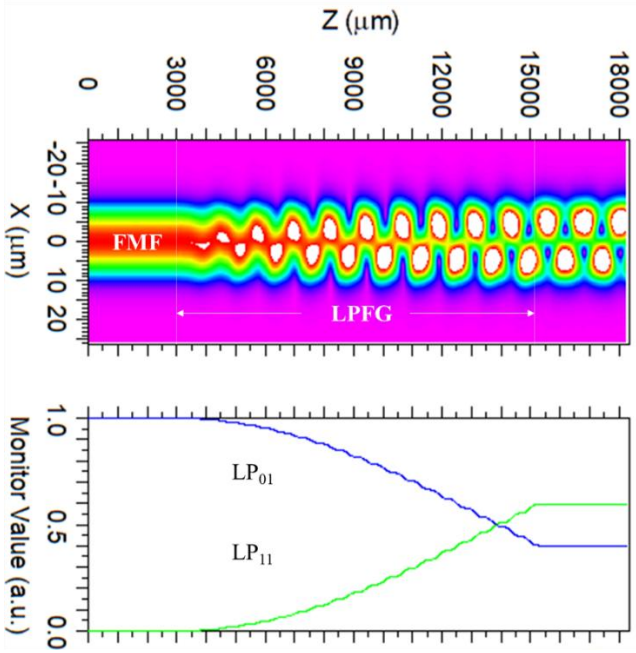

Figure 3.17: Beam propagation simulation of a broadband TMF mode scrambler.

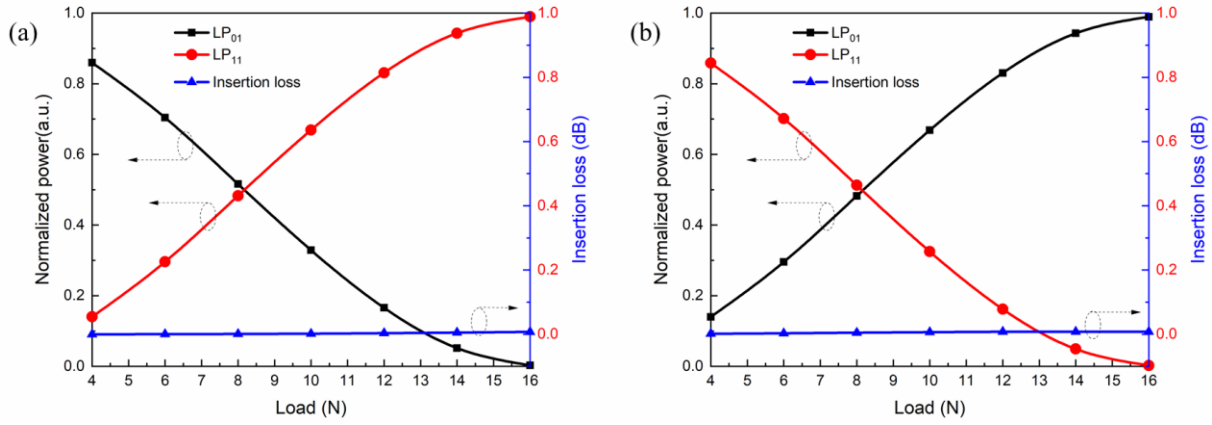

Figure 3.18: Simulated mode coupling properties of the mode scrambler under pure (a) LP_{01} and (b) LP_{11} mode excitations at different loads.

I have investigated how the optical bandwidth varies according to the grating length while maintaining the overall coupling efficiency at 60% (i.e. 4 dB coupling) at 1550 nm. Figure 3.19(a) shows the calculated transmission spectra and 3 dB-bandwidths (i.e. >50% coupling efficiency) of the LPFGs with various grating lengths. In the case of a 9.808 cm LPFG, the 3-dB bandwidth was only 15 nm but it increased gradually with a decrease in grating lengths. Notably the increase in bandwidth increases exponentially with reduced grating length for gratings with lengths in the few centimetres regime and the 3-dB bandwidths of 1.226 cm and 0.618 cm LPFGs were 135 nm and 260 nm, respectively. In Figure 3.19(b), the black line follows the analytical prediction of Equation (3.3) from simulated results (black dots). The red line is the IL of LPFGs and it decreases with an

increase in grating length. The maximum IL is found to be less than 0.02 dB and 0.06 dB for LP_{01} and LP_{11} mode excitation, respectively. This result indicates that short LPFGs represent a very effective way to realize broadband mode scramblers for FMFs.

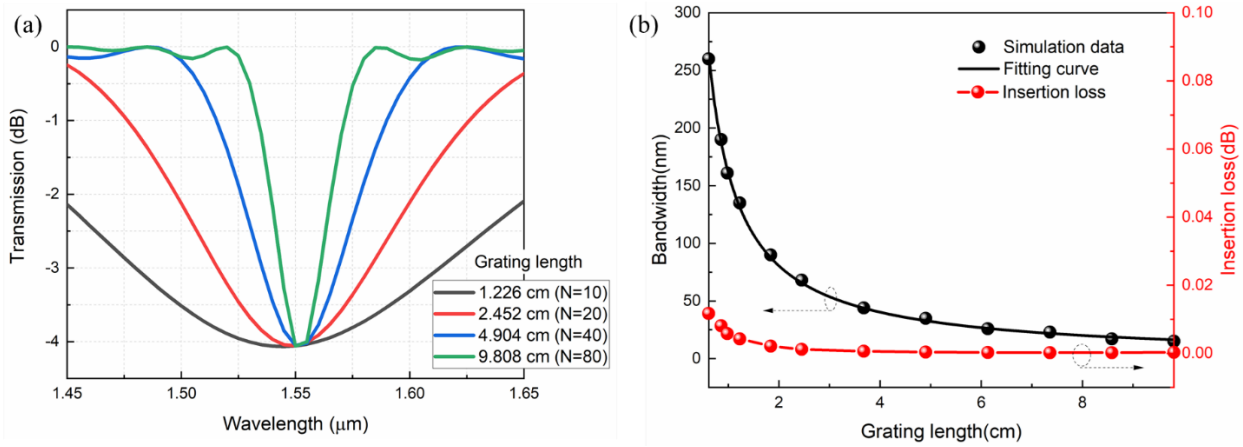

Figure 3.19: (a) Calculated transmission spectra and (b) 3 dB-bandwidths of the LPFGs with different grating lengths (for a fixed coupling strength of 60% at 1550 nm).

3.2.2.2 Experiments

First of all, the transmission spectrum of the 3D-printed TMF-LPFG was measured using a superluminescent diode (Thorlabs, S5FC1550P-A2) and an optical spectrum analyser. In order to make sure of pure LP_{01} mode excitation and detection, the TMF (having the same specifications as my simulation) was spliced with conventional SMFs at both input and output ends. The TMF was sandwiched between a flat metal plate and the 3D printed LPFG and a compressive force was applied by adding a static load to the top plate. Figure 3.20(a) shows the transmission spectra of the LPFGs with different grating lengths (10 cm, 5 cm, 2.5 cm, 1.25 cm). For the 10 cm long LPGF, the 3dB-bandwidth was only ~ 11 nm at 2.78 N total load. Notably more and stronger side lobes were observed with increased grating length, which is due to the fact that a longer grating has a narrow bandwidth and stronger sidelobes due to the Fourier transformation of the uniform grating distribution. As the grating length is decreased, however, we see a significant increase in optical bandwidth, which is in good agreement with my simulations. The 3dB-bandwidth of the 1.25 cm long LPFG was ~ 100 nm (from 1494 nm to 1594 nm), covering the whole C-band. The polarization dependence of 1.25 cm LPFG was also characterized by changing the input polarization via a fibre-loop polarization controller at the input SMF and just a minor transmission shift (2 nm) was observed.

In order to further confirm the 3-dB energy transfer between the LP_{01} and LP_{11} mode, a time-of-flight (or impulse response) measurement of the 1.25 cm-long LPFG was carried out. A mode-locked femtosecond pulsed fibre laser was launched into my mode scrambler and the output signal was

detected by a digital sampling scope after propagating through a 10 km-length of the TMF. As each mode of interest possesses a distinct group velocity and the light in different modes will arrive at the end of the fibre at different times and I can readily distinguish different spatial modes with their DGDs (DGDs) and identify the relative power distribution excited by the LPFG. As shown in Figure 3.20(b), an almost equal power distribution was observed between the LP_{01} and LP_{11} modes with the LPFG under a load of 1.5 N load and the mode coupling efficiency remains relatively constant over the C-band from 1535 nm to 1560 nm, which is in good agreement with the transmission spectra in Figure 3.20(a).

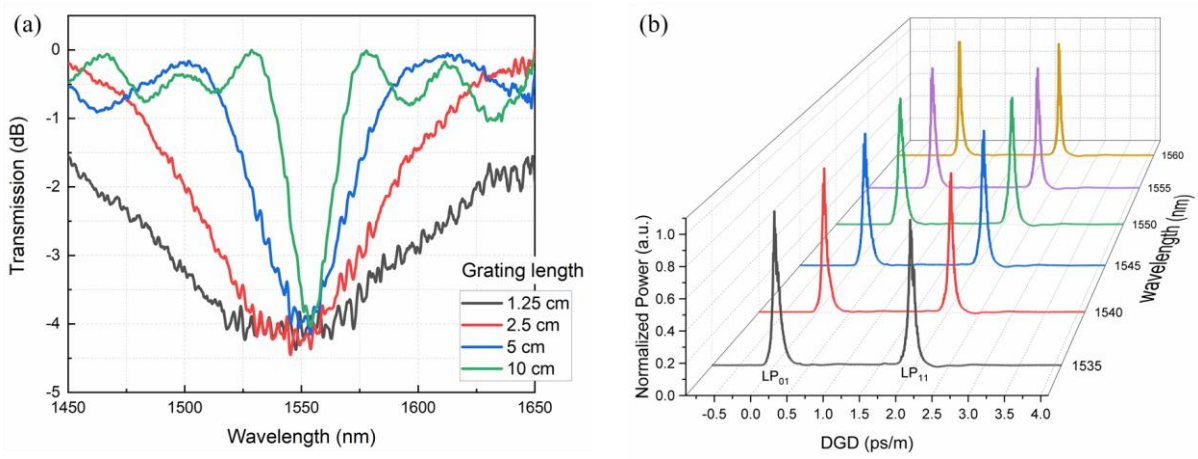

Figure 3.20: (a) Measured LPFG transmission spectra with different grating lengths and (b) the impulse response of 1.25 cm-long LPFG.

To further characterize the mode mixing properties of the device, a time-of-flight measurement was carried out in conjunction with mode selective excitation using a mode multiplexer based on phase plates [112]. Under LP_{01} mode excitation, as shown in Figure 3.21(a), most of the light power was in the LP_{01} mode but the power in LP_{01} is gradually coupled to LP_{11} mode with applied load. The coupling efficiency reaches ~50% when the load is 1.5 N and a periodic power oscillation was found between two spatial modes as the load is further increased. The IL was less than 0.2 dB at loads under 2.25 N. Under LP_{11} mode excitation, interestingly, the mode conversion efficiency strongly depends on the lobe orientation of the LP_{11} mode (i.e. whether the LP_{11a} or LP_{11b} mode is excited). For LP_{11a} mode excitation (i.e. vertical orientation which is the same direction as the external force), as shown in Figure 3.21(b), optical power gradually shifted from the LP_{11} to LP_{01} mode and the coupling efficiency can reach to ~50% at 1.5 N and ~80% at 3 N, which is consistent with the LP_{01} excitation case. The IL for LP_{11a} mode excitation was less than 0.2 dB for loads under 2.25 N. Under LP_{11b} excitation (i.e. horizontal orientation), however, there is barely any mode coupling from the LP_{11b} to LP_{01}, as shown in Figure 3.21(c). This phenomenon arises from the asymmetry of the LPFG, where the load is applied vertically at the top of the fibre and the fibre experiences unidirectional lateral offset or deformation [89]. Therefore, the efficiency of mode coupling is maximized when

the direction of the local deformation matches the lobe direction of the LP_{11} mode. I believe that this aspect can be addressed by creating a more symmetric grating using other fabrication techniques such as ultraviolet light inscription, CO_2 laser irradiation, arc discharge or periodic tapering.

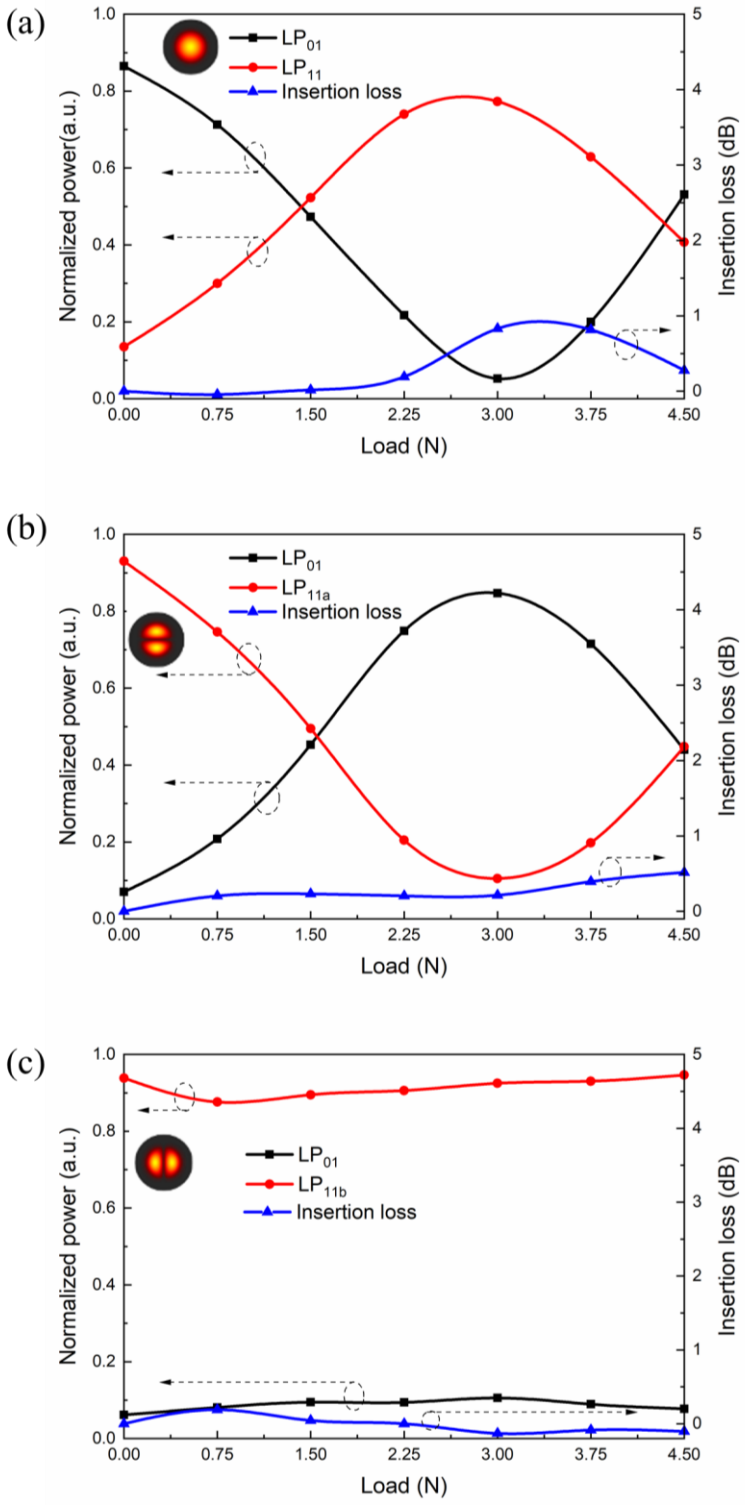

Figure 3.21: Experimental mode coupling properties of the mode scrambler under pure (a) LP_{01}, (b) LP_{11a} and (c) LP_{11b} mode excitation at different loads.

3.3 Dielectric Thin-Film Filters

Dielectric thin-film filters are optical filters that utilize multiple layers of dielectric materials deposited on optical surfaces, typically with thicknesses in the range of a few hundred nanometres. These filters selectively transmit or reflect specific wavelengths of light and are commonly used in WDM transmission systems as GFFs [113, 114]. One of the key advantages of dielectric thin-film filters is their capability to achieve a desired loss profile through interference within a single filter, which results in low IL, ease of manufacturing, and considerable design flexibility [115]. Recent advancements in thin film deposition technology have led to the development of high-precision systems that make these filters commercially available with exceptional accuracy. This technological progress enables the customization of dielectric thin-film filters to meet specific application requirements.

In this section, I will briefly discuss the fundamental working principles and characteristics of the dielectric thin-film filters we designed. Figure 3.22 illustrates an example of such a filter, configured as a series of a Fabry-Perot interferometers, or etalons. In this setup, each cavity is formed by multiple layers of dielectric thin films, where light undergoes multiple reflections and transmissions, either enhancing or reducing the transmission at specific wavelengths. By precisely controlling the thickness and refractive indices of these layers, interaction between light and coatings can be manipulated, thereby enabling the selective transmission or reflection of specific wavelengths.

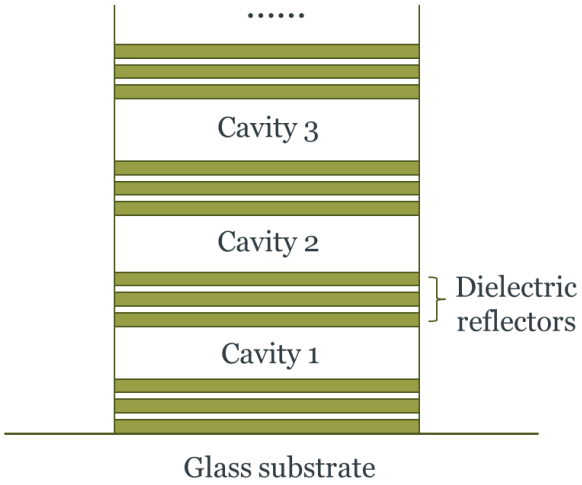

Figure 3.22: An example of thin-film resonant dielectric thin-film filter.

In my subsequent study on gain-flattened wideband YDFA, I employed customized dielectric thin-film filters from the IRIDIAN, specifically designed for 1 μm wavelength applications. As depicted in Figure 3.23, the transmittance characteristics of these filters demonstrate a strong alignment between the designed (solid blue line) and measured (dashed blue line) curves, indicating that the

filters effectively achieve the intended transmittance profile. The difference curve (orange) reflects the flatness of the filter, which remains within the specified tolerance of 0.5 dB, further confirming the precision of the design. Additionally, the IL was maintained at less than 1 dB, underscoring the filter's efficiency and suitability for gain flattening in wideband YDFA applications.

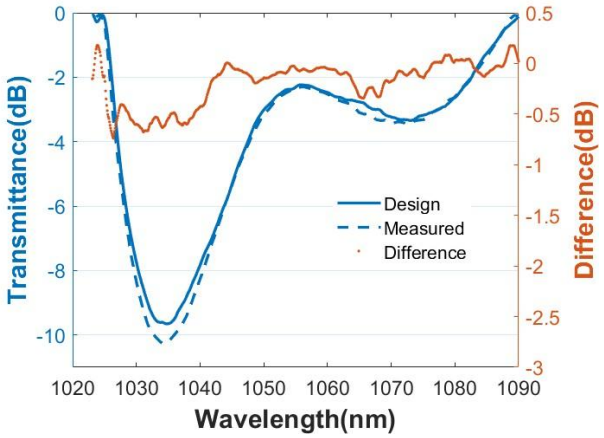

Figure 3.23: Designed characteristics of dielectric thin-film filter based GFF.

3.4 Programmable Waveshapers

A programmable waveshaper is an advanced spectral filtering tool, leveraging mature and commercially available technology based on advanced LCoS and it is widely employed in communications, pulsed lasers used in medical and industrial settings, and optical sensors [116-119]. Figure 3.24 shows the schematic of optical design of LCoS-based programmable optical processor. In this system, an input signal is first dispersed by a conventional grating, separating its spectral components before they reach the LCoS optical processor. This processor is composed of a matrix of reflective liquid crystal elements, each capable of applying individual phase shifts to the reflected signals through voltage control. This mechanism enables precise beam steering of the signal components, allowing independent control of each wavelength. Consequently, the system can switch or filter specific wavelengths without affecting others, providing capabilities for spectral attenuation, dispersion, and optical switching.

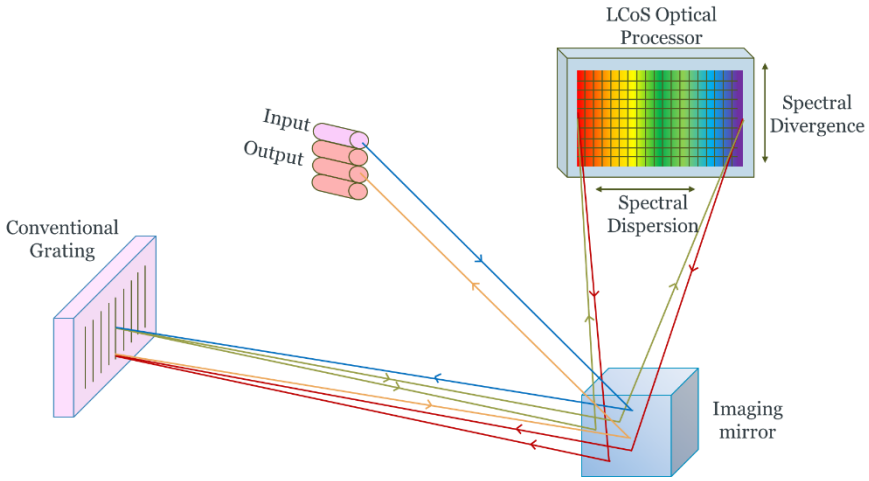

Figure 3.24: Schematic of optical design of LCoS-based Programmable Optical Processor

In the preliminary laboratory demonstration experiment, the waveshaper was utilized as an ideal filter component due to its precise programmability. Figure 3.25 illustrates examples of filter profiles generated by the Finisar waveshaper for gain flattening in 1.5 µm and 1 µm amplifiers This waveshaper provides a maximum attenuation of up to 35 dB, with a high resolution that spans from 10 GHz to 5 THz (0.08 to 40 nm). More details about the performance of these filters in the context of amplifier applications will be discussed in Chapter 4 and Chapter 5. While this device is well-suited for laboratory experiments due to its precision, Although the waveshaper's precision makes it highly effective for laboratory experiments, its significant IL of 4.5 dB limits its practicality for real-world applications.

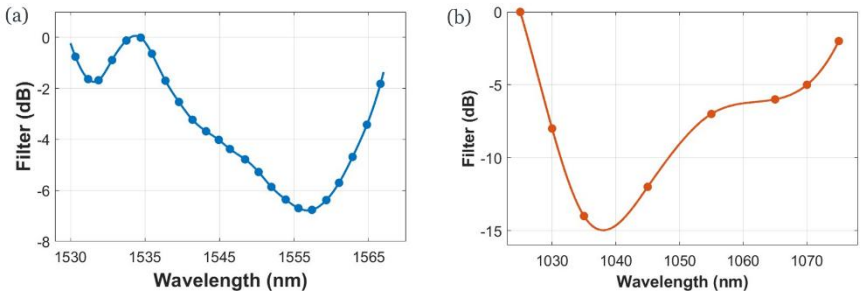

Figure 3.25: Filter that could be generated from programmable waveshaper at (a) 1.5 µm and (b) 1 µm.

In the telecommunication experiment, the waveshaper was also employed to generate a multi-channel comb source. Figure 3.26 illustrates the process of creating a multi-channel seed source filtered from an ASE spectrum at 1 µm for YDFA. The ASE spectrum (depicted in Figure 3.26(a)) was processed through a comb filter generated by the waveshaper (as shown in Figure 3.26(b)), finally generating a multi-channel comb source, as shown in Figure 3.26(c). Due to the waveshaper's high adjustable attenuation, the OSNR of the multi-channel source can be fine-tuned to exceed 30 dB.

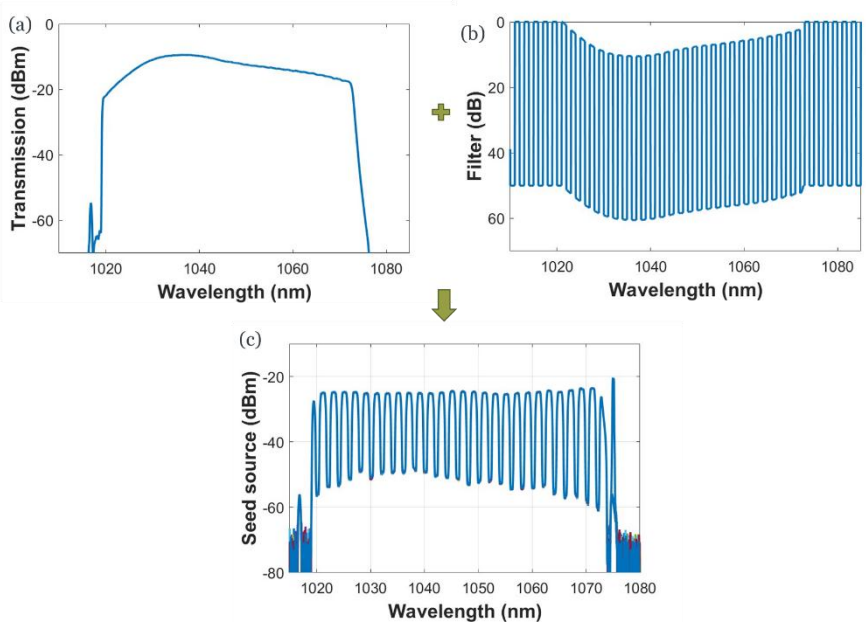

Figure 3.26: (a) measured ASE spectrum at 1 μm; (b) Filter spectrum generated from 1 μm waveshaper;(c) multi-channel seed source spectrum after filtered by comb filter.

3.5 Conclusion

In this chapter, I have explored three types of technologies for GFFs. First of all, LPFGs have been investigated as efficient spectral filters with the potential to serve as effective GFFs in multi-stage amplifiers and functional devices. In SMF based LPFG, mode coupling from LP_{01} fundamental mode to LP_{1m} cladding modes was demonstrated as a flexible and efficient spectral filtering method. Simulations of both conventional and phase-shifted LPFGs highlighted their capability to flatten and broaden the gain bandwidth in amplifiers. In the experiment, with a simple 3D printed technique, 600-740 μm grating pitch LPFGs were successfully fabricated, and clear resonance peaks were observed with more than 10 dB filter strength at 1.5 μm. The arc-induced tapered technique was explored for higher resolution fabrication of LPFGs at 1 μm, with a conventional LPFG featuring a 255 μm grating pitch achieving more than 20 dB attenuation at each resonant dip.

Furthermore, FMF based LPFGs have been tested as low-loss broadband mode scramblers using 3D-printed LPFGs. The optical bandwidth of the LPFGs was substantially improved by shortening the device length (i.e. number of periods of index modulation) and >260 nm bandwidth was predicted in our simulation with a 0.613-cm long LPFG. In my experiment, a 1.25-cm long LPFG was successfully fabricated using a commercial 3D printing technique and 100 nm bandwidth was confirmed over the C band with a low IL (0.2 dB) and low MDL (0.1 dB). This short fibre grating approach can be further applicable to optical fibres with a larger number of spatial modes (both step-index and graded-index profiles) and should be able to provide an efficient way of mode scrambling for successful MDM transmission.

The chapter also discussed dielectric thin-film filters and programmable waveshapers based on Liquid Crystal on Silicon (LCoS) technologies. These commercially available technologies have been successfully demonstrated as GFFs and multi-channel comb filters in my following research on gain-flattened wideband YDFA.

In summary, the technologies discussed in this chapter each contribute unique advantages to the development of spectral filters and GFFs in optical amplifiers. LPFGs offer a compact and low-loss solution with customizable spectral characteristics, dielectric thin-film filters provide high precision and low IL, and programmable waveshapers deliver flexible, programmable filtering capabilities, particularly suited for laboratory use. Overall, these technologies address the challenges of gain flattening in WDM systems, contributing to more efficient and reliable data transmission in optical networks. Their practical implementation in advanced optical systems will be further investigated in the following chapters.

Chapter 4 Wideband Erbium-Doped Fibre Amplifiers (EDFAs)

4.1 Introduction

With the surging global demand for bandwidth-intensive services—such as high-definition streaming, cloud computing, and real-time data analytics—the backbone of the internet relies more than ever on high-capacity optical communication systems. At the foundation of these systems lies Wavelength Division Multiplexing (WDM), a pivotal technique enabling the simultaneous transmission of multiple optical signals at distinct wavelengths through a single optical fibre. A key component in WDM systems is the erbium-doped fibre amplifier (EDFA), whose broad spectral amplification range facilitates the concurrent enhancement of multiple wavelength channels without the need for optical-electrical-optical conversion, thereby significantly enhancing transmission efficiency and system scalability [120, 121]. Effective amplifier deployment requires careful engineering to ensure signal integrity, operational reliability, and long-term system performance. The characteristics of amplifiers directly influence essential network parameters including maximum transmission distance, bit error rate (BER), and overall channel capacity. Understanding these relationships is fundamental to designing optimized amplifiers for optical networks that meet ever-increasing bandwidth demands [122, 123].

A primary performance requirement for optical amplifiers is providing sufficient gain to compensate for signal attenuation resulting from fibre losses, connector insertions, and various passive components throughout the transmission path. For WDM applications, spectral uniformity represents an equally critical parameter. Amplifiers must deliver consistent gain across their operational bandwidth to prevent channel power imbalances that would degrade the optical signal-to-noise ratio (OSNR) in certain channels and restrict effective transmission capacity.

Beyond gain considerations, the noise figure (NF) constitutes a fundamental parameter quantifying noise introduction during the amplification process. Minimizing this parameter is essential as it directly influences the OSNR—a key determinant of BER and maximum transmission distance. Although the quantum-limited theoretical minimum stands at 3 dB, this ideal amplifier remains unattainable in practical implementations.

The required gain and NF levels and amplifier types vary significantly depending on system architecture and position within the optical link. Optical amplifiers must meet stringent performance criteria to ensure reliable signal transmission across various network architectures, as

outlined in industry standards like Telcordia GR-1312-CORE [124]. Pre-amplifiers, positioned immediately before optical receivers, are optimized for low noise rather than high output power. These typically require 20-30 dB gain to boost weak incoming signals (approximately -30 dBm/channel) to levels sufficient for detection, while maintaining NF below 5 dB to preserve OSNR. Metropolitan networks spanning distances up to 200 km often employ compact pre-amplifiers, prioritizing cost and size efficiency over ultimate noise performance.

Booster amplifiers, located immediately after transmitters, provide moderate gain (10-20 dB) with high output power (≥+17 dBm per channel) to launch signals into the fibre span with sufficient strength to overcome span attenuation. These are typically deployed when the transmitter power alone is insufficient for long-reach or high-loss segments. Data centre interconnections, operating over short to medium distances (10–80 km), utilize high-output booster amplifiers to overcome transceiver limitations, requiring flat gain profiles and excellent thermal stability in dense equipment environments.

In-line amplifiers are deployed at periodic intervals (typically every 80-100 km) in long-haul systems to counteract accumulated fibre loss. These usually provide 20-25 dB gain, with balanced noise and power characteristics to maintain signal quality through multiple spans. Long-haul submarine cable systems demand exceptionally low NF (typically below 5 dB) and high-gain in-line amplifiers at regular intervals to preserve OSNR over thousands of kilometres. These undersea systems also require extraordinary reliability and power efficiency due to the significant challenges associated with maintenance in submarine environments.

Traditional amplifier designs have primarily relied on single-stage configuration, incorporating co-directional, counter-directional, and bi-directional pumping techniques. However, the growing demand for higher gain, increased output power, and lower NF has driven the development of multi-stage EDFAs. Unlike a simple assembly of single-stage amplifiers, multi-stage amplifiers represent an advancement in optical fibre design that optimizes EDFA properties for specialized applications. Achieving a low NF requires maintaining a high population inversion throughout the fibre, which is typically accomplished by using shorter EDFs to maintain a high population density and reduce the forward ASE. However, shorter EDFs often result in insufficient gain and output power. Multi-stage EDFAs resolve this issue by using the first stage as an efficient pre-amplifier with low NF, while subsequent stages serve as power boosters. Additionally, multi-stage configurations can incorporate additional optical components, such as GFFs, between stages to expand the gain bandwidth and improve gain uniformity across different wavelengths.

Actually, multi-stage EDFAs have been used in a wide range of applications from conventional transmission systems to optical switch or local area network (LAN) fibre distribution. For example,

they have been as power booster, pre-amplifier and optical repeaters in long haul optical fibre transmission systems [28, 125]. Thus, on the investigation of multi-stage EDFAs in this chapter, I will only provide a brief discussion on the gain flattened C-band and C+L band dual-stage EDFA (DS-EDFA), will help establish the theoretical and experimental foundation for my subsequent research on wideband YDFAs. To provide a standardized performance benchmark, the analysis of amplifier performance in this thesis assumes small signal amplification with NF below 6 dB as target specifications.

In section 4.1, I will explore C-band EDFA through simulation and experiment and have shown that fibre amplifiers with high gain, good gain flatness and low NF can be achieved in a DS-EDFA configuration. In section 4.2, I will further extend C-band DS-EDFA to C+L band DS-EDFA spanning from 1530nm to 1610 nm (optical bandwidth of 80 nm) with an optimized GFF in simulations.

4.2 Gain Flattened C-band EDFA

4.2.1 Simulations

In order to quantitatively investigate the general trend of the DS-EDFA, the numerical software Optisystem is used to design the gain flattened C-band EDFA. First of all, I have simulated a simple SS-EDFA with 24 WDM channels from 1530 nm to 1567 nm. Figure 4.1 shows schematic of a SS-EDFA with an ideal GFF (without any IL) at the end of setup. A 980 nm laser diode (LD) with 100 mW power was used as a pump source in a forward pumped configuration. Two isolators were inserted at both input and output ports in order to improve the noise characteristics by reducing the ASE into the active fibre. Insertion losses of the isolators (1 dB each) and WDMs (0.5 dB each) were considered in the simulation. I use parameters of the EDF from Fibrecore (I-12 980/125) in the simulation that has a core radius of 1.6 µm, NA of 0.22 and peak absorption of 11.9 dB/m at 979 nm. Table 3 shows the parameters used in my simulation.

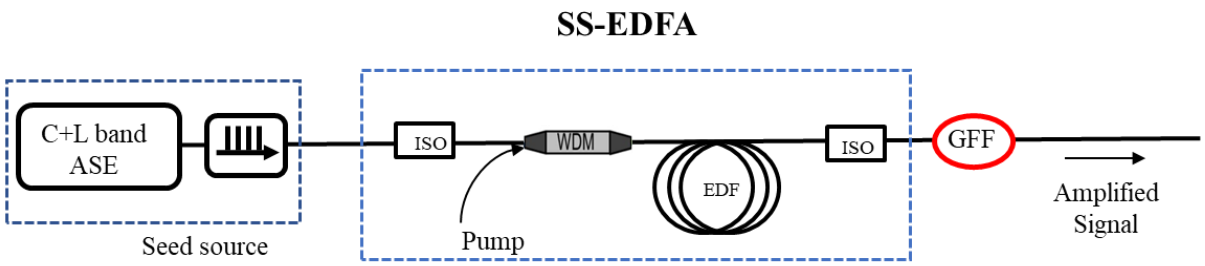

Figure 4.1 Schematic of a SS-EDFA.

Table 3: Parameters used in the simulation

Parameters	Values

Channels	24
Signal wavelengths	1530 nm-1567 nm
Input signal power	-30 dBm
Pumping power	100 mW
Pumping wavelength	980 nm
Core radius of EDF	1.6 μm
NA of EDF	0.22
Er^{3+} doping concentration of EDF	18×10^{24} m^{-3}

Figure 4.2 shows the gain and NF spectra with various fibre length in 1530-1567 nm. The gain peak (top figure) shifts to longer wavelengths as the gain fibre length increases. This shift is primarily due to signal reabsorption at shorter wavelengths, resulting in a change in gain bandwidth. My simulations indicate that an EDFA using a 7-meter fibre length exhibits a relatively flat gain spectrum, as shown by the purple curve. The minimum gain flatness (difference between maximum gain and minimum gain), approximately 6.4 dB, is achieved at this 7-m's fibre length, with a maximum gain of 31.6 dB. The bottom graph depicts the NF, which shows a slow but steady increase with longer fibre lengths. Despite this increase, the NF remains consistent, staying within a range of 4 to 5 dB across the entire wavelength spectrum. Given the balance between gain and NF performance, a 7-m fibre length provides optimal performance for a SS-EDFA.

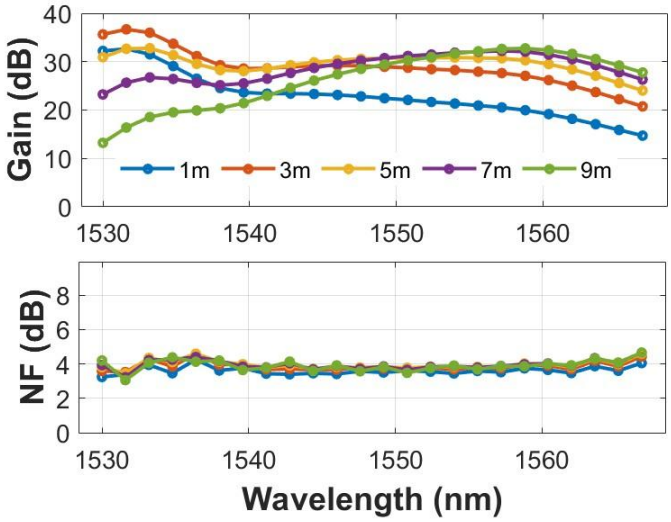

Figure 4.2: Gain and NF spectra for SS-EDFA with various fibre lengths within the wavelength range of 1530–1567 nm.

Figure 4.3(a) shows the gain spectrum of a SS-EDFA without any GFFs. The ASE spectrum (red lines) and output signal powers of 24 WDM channels (green lines) were not so flat in the C-band as expected. After EDF, by employing an optimized GFF, the power spectrum was flattened and the gain variation of EDFA was reduced to 0.4 dB as shown in Figure 4.3(b). The blue line shows the GFF spectrum and the maximum attenuation strength of the GFF was ~7 dB. Note that the optimized

GFF can be determined by the iterative method from Optisystem in order to minimize the ratio between minimum and maximum gain (ripple) and to provide the inverse transfer function in the system. Figure 4.4 depicts the gain and NF characteristics of EDFA without and with a GFF, respectively. The maximum gain was decreased from 31.5 dB to 25.0 dB whilst NF was slightly increased from 5.3 dB to 5.7 dB by employing the GFF. Note that any optical loss or attenuation after the output of the amplifier does not affect NF significantly (because both signal and noise powers will be attenuated) and only 0.3 dB NF degradation is observed in this particular simulation.

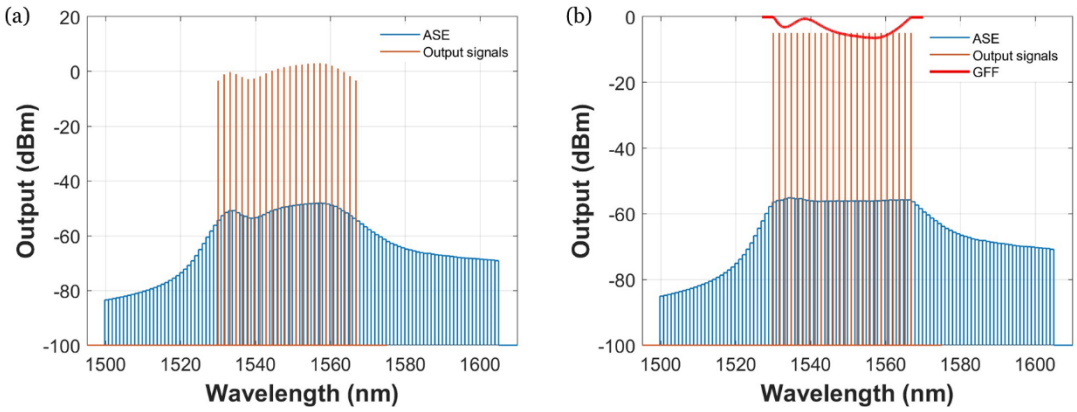

Figure 4.3 Output power spectrum (orange line) and noise spectrum (blue line) of EDFA (a) without and (b) with GFF.

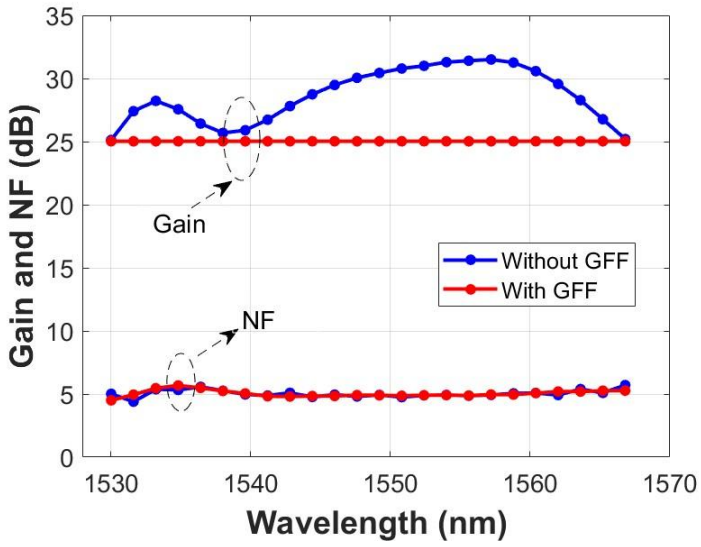

Figure 4.4 (a) Gain spectrum and (b) NF spectrum pf EDFA without (blue line) and with a GFF (red line).

As a more practical amplifier configuration, a DS-EDFA was analysed with a GFF and Figure 4.5 shows the schematic of a DS-EDFA. In addition to the two isolators at input and output ends, a mid-stage isolator was inserted between the two stages to prevent ASE from the 2nd stage going back into the 1st stage. In this configuration, each EDF (EDF1 and EDF2) is forward pumped by a 980 nm

pump laser with 30 mW and 100 mW pump power, respectively and an ideal GFF is incorporated between two amplifier stages. By taking account of minimum ΔG, maximum gain and NF, the fibre lengths of EDF1 and EDF2 in a dual-stage amplifier are chosen to be 2 m and 14 m (with the minimum ΔG), respectively.

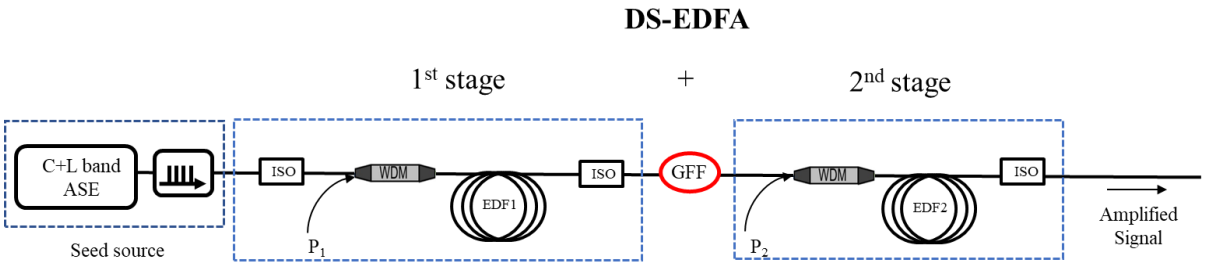

Figure 4.5 Schematic of a dual-stage EDFA.

Figure 4.6 (a, b) depicts the gain spectra of a DS-EDFA without and with a GFF. The gain variation of the amplifier was greatly improved from 6 dB to 0.5 dB by employing an optimized GFF between two amplifier stages. The gain spectrum is flattened to be ~30.5 dB and the maximum strength of GFF was ~9.8 dB. The NF was slightly increased from 5.3 dB to 5.6 dB (i.e. 0.3 dB increasement), as shown in.

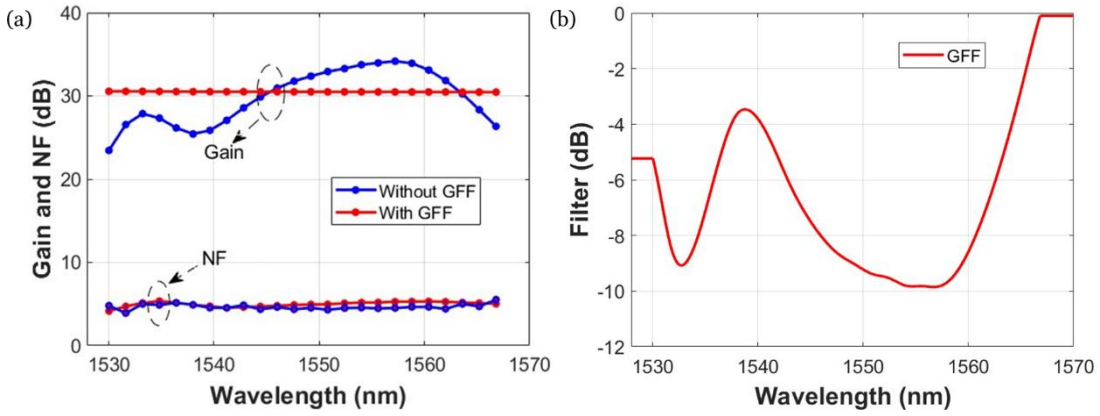

Figure 4.6: The gain and NF spectra of a dual-stage EDFA without (blue curve) and with a GFF (red curve); (b) GFF spectrum.

4.2.2 Experiments

Based on the simulation results, a SS-EDFA was firstly constructed and characterized in the experiment. I used an in-house incoherent 50 WDM channels as a seed source which was constructed from a C+L band ASE source and two cascaded 100/200 GHz interleavers. Figure 4.7 shows the input spectrum from the multichannel seed source which produced 24 WDM channels in 1530-1567 nm region. The average power was kept at -30 dBm per channel with ~5 dB intensity variation. The spliced loss between the EDF and SMF was ~ 0.1 dB and IL of isolators and WDM coupler were ~1 dB and ~0.5 dB, respectively. A Programmable WaveShaper (Finisar 4000S,

operating wavelength range=1527.4-1567.5 nm, attenuation control range=0-30 dB, attenuation setting resolution=0.01 dB, polarization dependent loss= 0.2 dB) was used as a programable GFF at the end of SS-EDFA and the average IL of the waveshaper was ~6.5 dB. The input and output spectra were measured by an OSA with resolution of 0.2 nm. Gain and NF spectra between experimental results and numerical simulation were compared with different fibre lengths and are shown in Figure 4.8. The simulation results matched quite well with the experimental data of the SS-EDFA without a GFF. Under 100 mW of forward pump power, a SS-EDFA with a fibre length of 6 m shows gain peak at 1532nm with ~8.4 dB gain variation but the gain peak of a SS-EDFA with a fibre length of 8 m shifted to 1560 nm and the gain variation was ~ 7.2 dB. NF of both cases were less than 3.6 dB. Comparison of gain and NF spectrum of SS-EDFAs with and without GFF is shown in Figure 4.9 (a), where the average gain is flattened from 32.1 dB to 19.7 dB with less than 0.5 dB gain variation and maximum NF slightly increased from 3.6 dB to 4.2 dB. Note that the decrease in average gain is mainly due to the IL of the waveshaper used in our experiment (~6.5dB) and it can be further improved by the dual-stage amplifier design or low loss fibre optic GFFs in the future. The attenuation spectrum of the GFF is shown in Figure 4.9(b) and the maximum attenuation value was ~ 6.7 dB at 1558.4 nm.

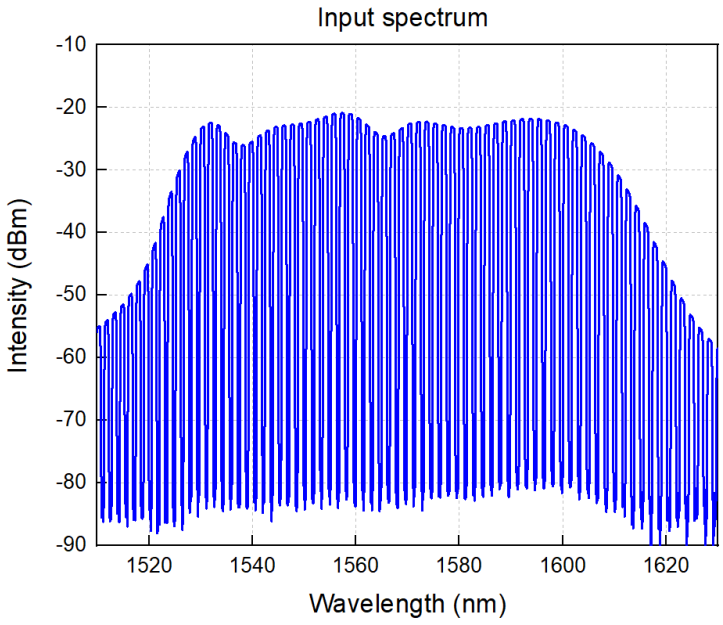

Figure 4.7 Input spectrum from the multichannel seed source with average power of -30 dBm per channel. (1530-1567 nm, resolution: 0.2 nm).

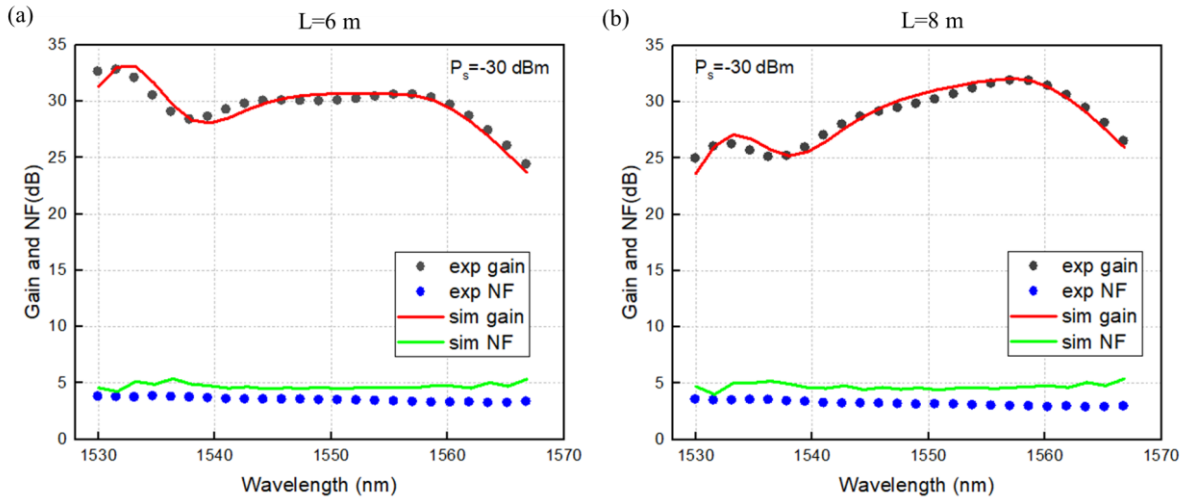

Figure 4.8 Comparison of gain and NF between experimental results and numerical simulation for (a) L= 6 m; (b) L=8 m.

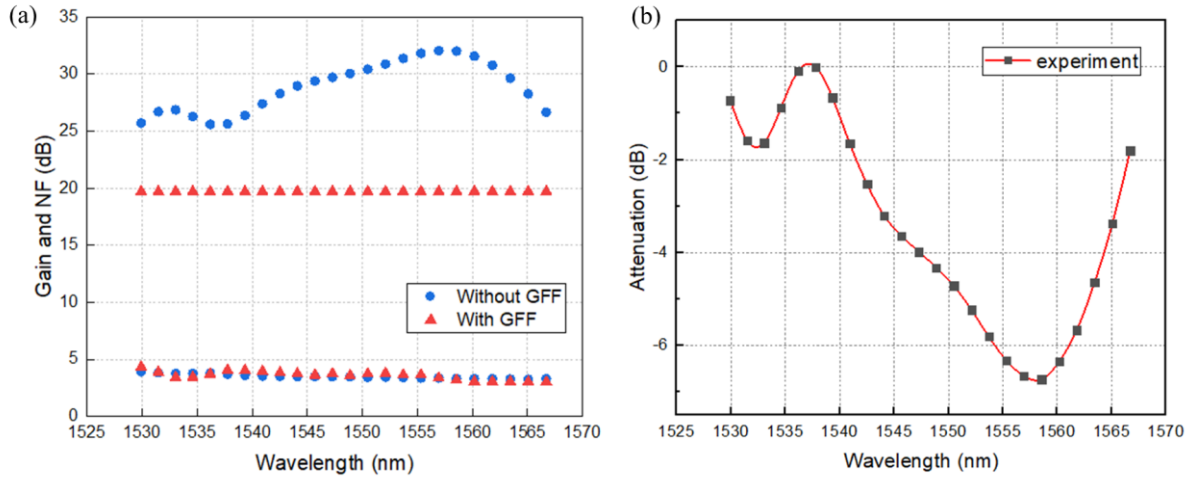

Figure 4.9 (a) Gain and NF spectrum with and without the GFF; (b) Spectrum of GFF that was imported to waveshaper.

DS-EDFA was further characterized with the insertion of a GFF interstage. The EDF1 of the 1st stage EDFA has a relatively short fibre length of 2 m to have a low NF value but EDF2 was chosen to be 7 m to compensate the loss from the GFF and to achieve high output power. The pump power of the1st and 2nd stage EDFA was kept to 30 mW and 100 mW, respectively. Figure 4.10(a) shows the gain and NF spectrum with and without the GFF. The maximum gain and NF are 29.9 dB and 6.3 dB without having any GFF function (shown in blue circles) but the gain was flattened to be 26.8 dB after employing a GFF having a maximum attenuation of 7.9 dB (shown in Figure 4.10(c)). Gain flatness was improved from 7.8 dB to 0.6 dB. The NF showed the maximum value of 6.5 dB at 1531.6 nm but was degraded from 4.8 to 6 dB at 1556.6 nm due to the high attenuation of the GFF at this wavelength. Figure 4.10(c) plots the output spectrum with >15 dB's OSNR of the gain-flattened DS-

EDFA at a resolution of 0.2 nm, where the spectral envelope follows the envelope of the input signal spectrum.

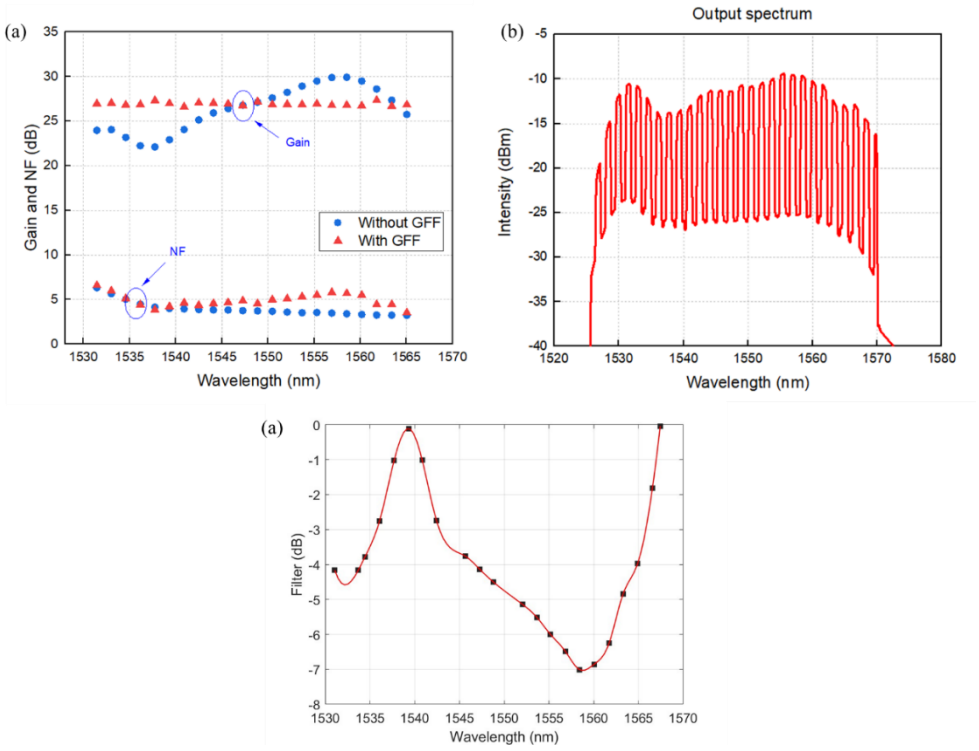

Figure 4.10 (a) Gain and NF spectrum of DS-EDFA with and without GFF; (b) Output spectrum of gain flattened DS-EDFA (resolution: 0.2 nm); (c) GFF spectrum that was imported to waveshaper for DS-EDFA.

4.3 Gain Flattened Wideband (C+L) EDFA

As illustrated in Figure 2.7, a higher population inversion (>80%) is required for C-band EDFA, while efficient amplification in the L-band typically needs around 40% inversion. However, by maintaining the average population inversion in the range of 50-60 %, it is possible to achieve amplification over a significant portion of the C+L band with improved gain flatness (often referred to as an 'extended C-band EDFA'), although this comes at the expense of reduced peak gain. A multistage amplifier incorporating GFFs can provide an efficient solution for achieving broadband amplification under these conditions. To evaluate this feasibility, a simulation was conducted using 41 WDM channels spanning from 1530 nm to 1610 nm, as illustrated in Figure 4.5. A 10 m fibre length was employed in each stage of the amplifier to ensure sufficient gain in the L-band region. In order to purely characterise the performance of EDFA, the IL of GFF was considered to be ideal (0 dB).

Under a population inversion of 50-60%, the amplifier achieves its highest gain in the spectral region between 1550 nm and 1575 nm, which leads to strong saturation of the amplifier, as indicated by the blue line in Figure 4.11(a). Consequently, placing a GFF within this specific spectral window has a significant effect on both gain flatness and the enhancement of the gain bandwidth. As shown in

top of Figure 4.11(a), the gain spectrum is effectively flattened to approximately 30 dB across the 1530 nm to 1610 nm range, providing an impressive 80 nm bandwidth. This represents a substantial improvement compared to conventional EDFAs, which typically have a bandwidth of only 35 nm (from 1530 nm to 1565 nm). The gain flatness is also improved to less than 1.3 dB, highlighting the efficiency of the gain-flattening strategy. However, as shown in bottom of Figure 4.11(a), this improvement in bandwidth and gain flatness comes with a trade-off, as the NF is significantly degraded from 4.6 dB to 10 dB. That's primarily due to the high peak attenuation of the GFF, which reaches up to 38 dB in this case. Considering the programmable waveshaper that we have in the lab, I also simulated the performance of a dual-stage EDFA while taking into account the characteristics of the C+L band waveshaper (Finisar 1000B/X), which operates in the wavelength range of 1524.33–1613.0 nm. The waveshaper's specifications include an attenuation control range of 0-40 dB, an attenuation setting resolution of 0.01 dB, IL of 6 dB, and a polarization-dependent loss (PDL) of 0.6 dB. In the simulation, the IL of the GFF was set to 6 dB to accurately reflect real-world conditions. While the gain spectrum was consistent with previous results, the NF showed greater degradation, reaching up to 17 dB due to the high IL and strong attenuation from the waveshaper and GFF. Given this large NF, I did not proceed with further experimental validation. To mitigate this issue and achieve better overall performance in a gain-flattened C+L band EDFA, it may be necessary to employ a GFF with reduced IL or add another amplifier stage. This would help distribute the gain more evenly and lessen the negative impact of the GFF and IL on the NF, resulting in a more balanced amplifier design. I have applied this concept in my subsequent investigations of YDFA.

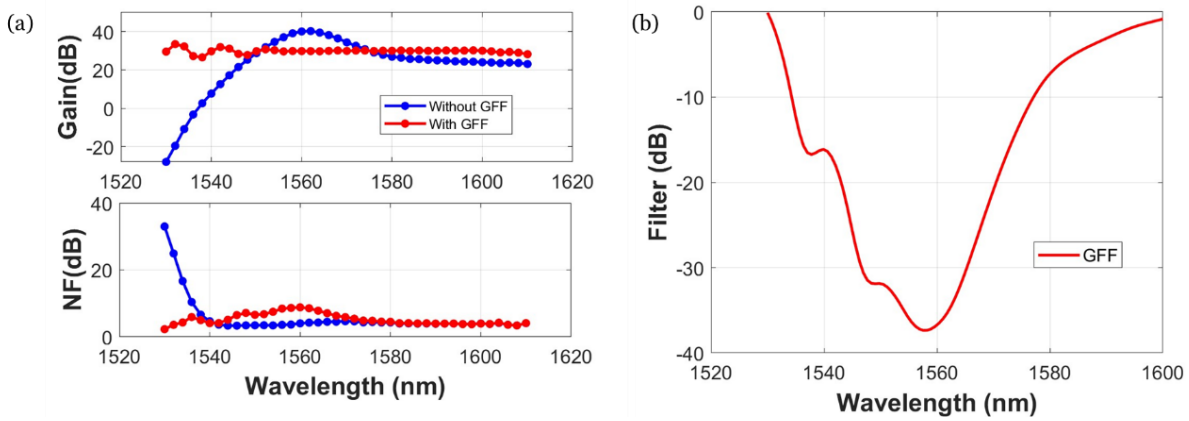

Figure 4.11: (a) Gain spectrum and NF spectrum of C+L band dual-stage EDFA without GFF (red line) and with GFF (blueline); (b) GFF spectrum in 1530-1600 nm.

4.4 Conclusion

In this chapter, I designed and analysed a multi-stage EDFA with the goal of expanding the gain bandwidth of the existing C-band EDFA. Initial simulations of a single-stage C-band EDFA demonstrated that the gain flatness could be significantly improved by incorporating an optimized GFF. By doing so, the gain variation was reduced from 6 dB to 0.5 dB. Notably, the maximum GFF attenuation was ~9.8 dB, and the NF experienced only a minimal increase (~0.3 dB). These findings were validated experimentally, where the gain was flattened to 26.8 dB with a gain variation of less than 0.6 dB, while the NF increased only slightly from 6.3 dB to 6.6 dB. This highlights the effectiveness of GFFs in achieving a flatter gain spectrum with minimal impact on noise performance.

To further extend the bandwidth, I employed a stronger GFF, which successfully increased the amplifier's bandwidth to 80 nm, spanning from 1530 nm to 1610 nm in theory. However, this was accompanied by a significant degradation in the NF, which increased to 17 dB, largely due to the higher attenuation introduced by the GFF and the IL of the waveshaper. This underscores the trade-off between bandwidth extension and noise performance when using stronger GFFs. To address this, future work should focus on optimizing these filters to minimize attenuation, or alternatively, consider the use of three-stage amplifier configurations to distribute gain more effectively across the C+L band while reducing the negative impact on the NF.

This research demonstrated that through the use of optimized GFFs and multi-stage configurations, it is possible to significantly enhance the gain flatness and bandwidth of EDFAs. While the introduction of GFFs can slightly degrade noise performance, these effects can be mitigated by thoughtful design choices, such as employing additional amplifier stages or optimizing filter parameters. The findings in this chapter lay a solid foundation for my subsequent work on broadband YDFAs, particularly for long wavelength amplification, and provide a basis for exploring even wider amplification ranges with minimal trade-offs in NF and gain performance.

Chapter 5 Wideband Ytterbium-Doped Fibre Amplifiers (YDFAs) in the 1025-1075 nm Range

5.1 Introduction

As discussed in Chapter 1, the low-loss hollow-core fibre (HCF) operating at 1 µm (0.30 dB/km @1060 nm) offers significant potential for 1 µm data transmission systems, emphasizing the need for a compatible wideband 1 µm fibre amplifier. In this chapter, I present the first experimental realization of YDFAs specifically designed for optical communication at 1 µm and the first demonstration of 1-µm transmission system using the broadband YDFA.

I first discuss in Section 5.2 the general design considerations for developing wideband YDFA for 1 µm telecommunications applications. The initial numerical design involved simulations of both single-stage and dual-stage YDFAs to evaluate their amplification effectiveness. Prior to characterizing the amplifier performance, the components were assessed by measuring the absorption spectrum of the ytterbium doped fibre (YDF) and evaluating the performance of wavelength-division multiplexers (WDM) and optical isolators. Subsequently, the amplifier's performance in terms of gain, NF, and gain variations was characterized within the 1020-1080 nm range. Additionally, a >100-Gb/s transmission system operating in the 1020-1080 nm with a 16.3 THz's bandwidth was demonstrated using the broadband YDFA. To achieve a wideband gain-flattened YDFA, a gain flattened dual-stage YDFA (DS-YDFA) was designed by incorporating a programmable waveshaper interstage, as discussed in Section 5.3. The numerical design and experimental validation of a wideband gain-flattened YDFA in a dual-stage configuration (similar to a gain-flattened EDFA) were undertaken, operating in the wavelength range from 1025-1075 nm. An average gain of 20 dB was successfully achieved with less than 1-dB spectral gain variation and a NF of less than 5.7 dB across the full bandwidth.

5.2 Single-and Dual-Stage YDFAs

The design considerations for wideband YDFAs are similar to those for wideband EDFAs. A simple single-stage YDFA (SS-YDFA) consists of a Wavelength Division Multiplexer (WDM) that combines the input signal and the pump, and two isolators placed at both the input and output. These isolators stabilize signal amplification by eliminating unwanted back reflections from the output port. Additionally, a certain length of Ytterbium-Doped Fibre (YDF) serves as the active gain medium to amplify the signal, as illustrated in Figure 5.1(a). To extend the bandwidth without sacrificing gain

and NF performance, a dual-stage amplifier configuration is proposed, as shown in Figure 5.1(b). In this configuration, the amplified signals from the output of the first stage amplifier are coupled to the input of the second stage amplifier.

In this subsection, I undertake the numerical design and experimental validation of a YDFA in both single-stage and dual-stage configurations, similar to the configurations used for EDFAs. Numerical simulations of YDFAs operating in the 1020-1110 nm range were conducted to identify the amplifier's effective amplification bandwidth. Following this, experimental validation was performed.

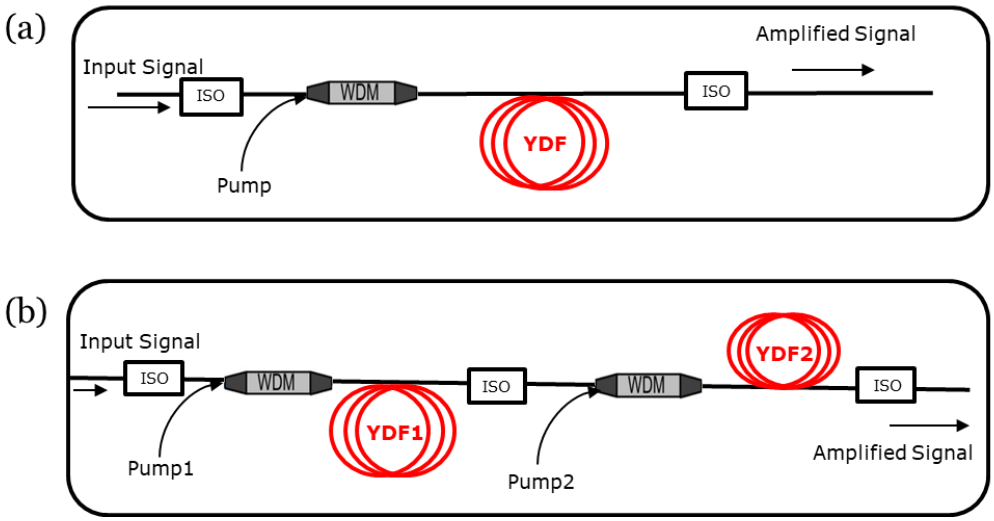

Figure 5.1 Schematics of (a) single-and (b) dual-stage YDFA. WDM: wavelength division multiplexer; ISO: isolator; YDF: ytterbium doped fibre.

5.2.1 Simulations

In order to numerically analyse and investigate the wideband YDFA, a fibre amplifier simulation tool (OptiSystem) was used to design the broadband YDFA. Firstly, a SS-YDFA was simulated to identify its effective amplification bandwidth. 91 WDM channels at wavelengths between 1020-1110 nm with a 1 nm channel spacing were considered as the seed source (-20 dBm/ch), and the YDF was forward pumped by a 980 nm LD with 300 mW of pump power. The fibre specifications of the commercial YDF from iXblue were considered in the simulation, i.e., a core/clad diameter of 6/125 µm, NA of 0.12 and a doping concentration of 3200 ppm. Note that relatively low doping concentration was chosen for convenience in achieving the target amplifier bandwidth with a reasonable device length. The IL of the isolators (1 dB) and WDM couplers (0.5 dB) were also considered in the simulation. The optimum length of YDF was determined based on the calculated gain and NF spectra when the fibre length was varied to yield the widest gain bandwidth. Figure 5.2 shows the layout of the SS-YDFA from Optisystem.

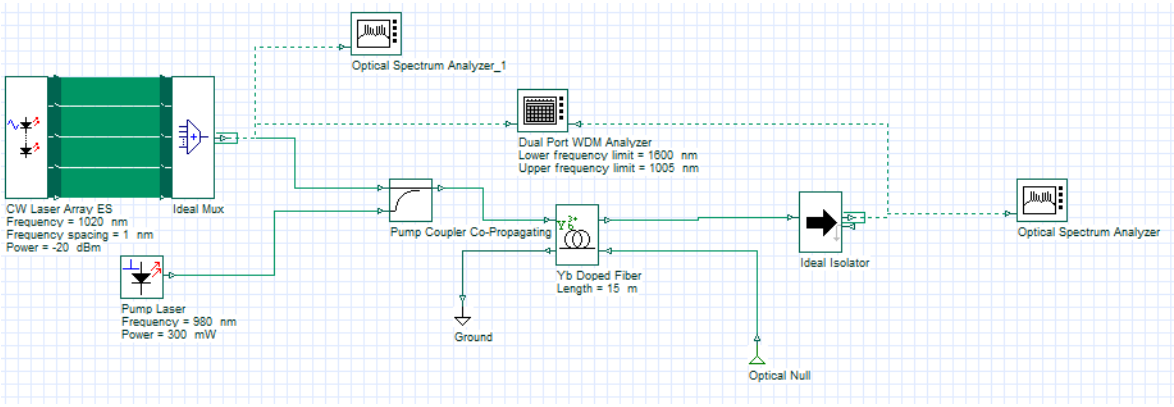

Figure 5.2: Layout of the SS-YDFA from Optisystem.

The results of the simulations are shown in Figure 5.3(a), the gain peak shifts to longer wavelengths as the gain fibre length increases because of signal reabsorption at shorter wavelengths, accompanied by a concurrent alteration in gain bandwidth. My simulations indicate that an amplifier incorporating a 9 m length of YDF exhibits a reasonably flat gain spectrum over a 10-dB bandwidth of ~87 nm ranging from 1023 to 1110 nm with >10 dB gain. In this case, while the NF increases rapidly at short wavelengths (Figure 5.3(b)) due to signal reabsorption, the NF in the wavelength range of interest remains relatively low (e.g. <4.3 dB from 1023-1110 nm).

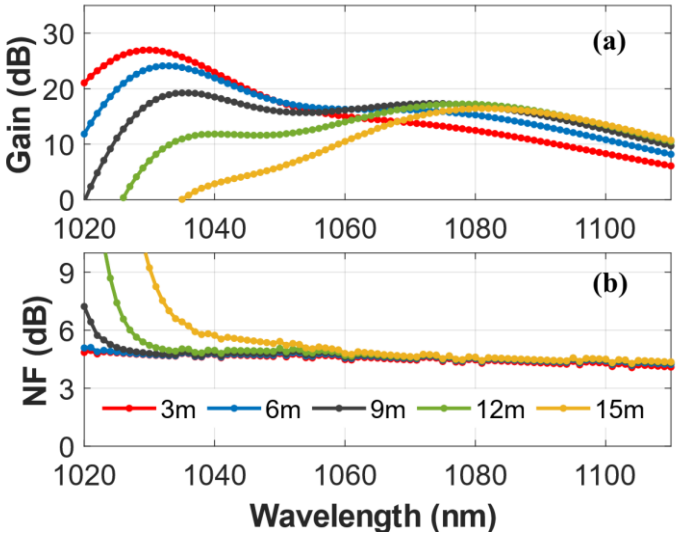

Figure 5.3: The (a) gain and (b) NF spectra of the SS-YDFA.

Subsequently, I explored a DS-YDFA to increase the overall gain. A DS-YDFA without a GFF was first simulated to investigate the impact of different fibre lengths on the gain and NF and to identify the optimum fibre length for maximum bandwidth. Note that the NF of a multi-stage amplifier is primarily determined by the 1st stage amplifier [120], hence a relatively short YDF length (3 m) was used in the 1st stage amplifier in our DS-YDFA to ensure that a high inversion is maintained across the entire length and to minimize the buildup of forward propagating ASE. Figure 5.4 (a, b) shows

the gain and NF spectra for different lengths of YDF used in the 2nd stage amplifier. 300 mW of pump power was considered in each stage. Despite the slight differences in fibre lengths, the general trend of the gain and NF spectra was similar to that of the single-stage amplifier in Figure 5.3(a, b). When the fibre lengths were 3 m and 9 m for YDF1 and YDF2, respectively, we achieved a 10-dB bandwidth (72 nm wide) ranging from 1025 to 1097 nm with a gain of more than 17 dB. The estimated NF across the wavelength range of 1025-1097 nm was less than 4.7 dB. Increasing YDF2 to 12 m resulted in an even flatter gain spectrum and an increased bandwidth of 78 nm (1028-1106 nm).

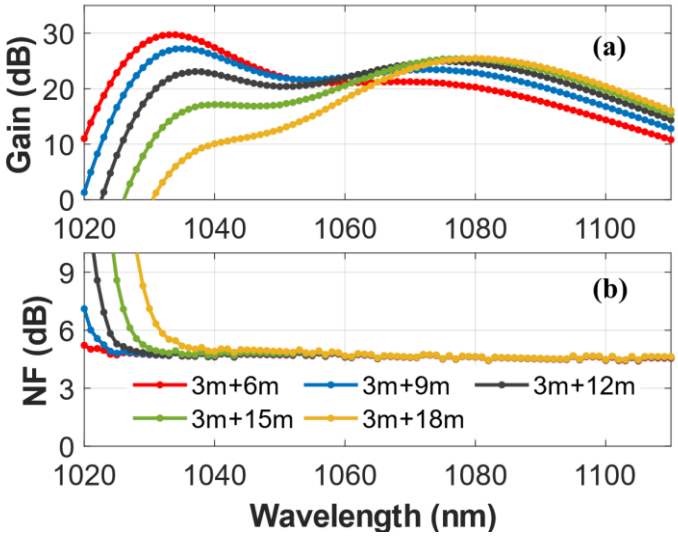

Figure 5.4: The (a) gain and (b) NF spectra of the DS-YDFA without a GFF

5.2.2 Experimental Results

Due to the lack of commercial multi-channel seed sources at 1 µm, a tunable laser source (TLS) (Toptica, DL pro) was used to provide input signals. The operating wavelength of the TLS ranges from 1020 to1080 nm with a linewidth of 300 kHz. An optical attenuator (ATT) was put after the TLS to adjust the input signal power. In my experiments, optical isolators based on a yttrium iron garnet (YIG) Faraday rotator [126] were initially employed as the input, output, and interstage isolators. Figure 5.5(a) shows the measured isolation and transmission spectrum of the YIG-based optical isolator. It exhibits high IL in the short-wavelength region due to the material absorption, with an IL of approximately 3-4 dB around 1020 nm. This high IL is the main reason for the large NF of the YDFA at short wavelengths, as shown below. Figure 5.5(b) shows the IL (dB) and transmission (%) as functions of wavelength of the thin-film based WDM coupler. This coupler is customized for high transmission beyond 1011 nm and low transmission at 1018 nm at the transmission port (blue line), while exhibiting opposite characteristics at the reflection port (red line).

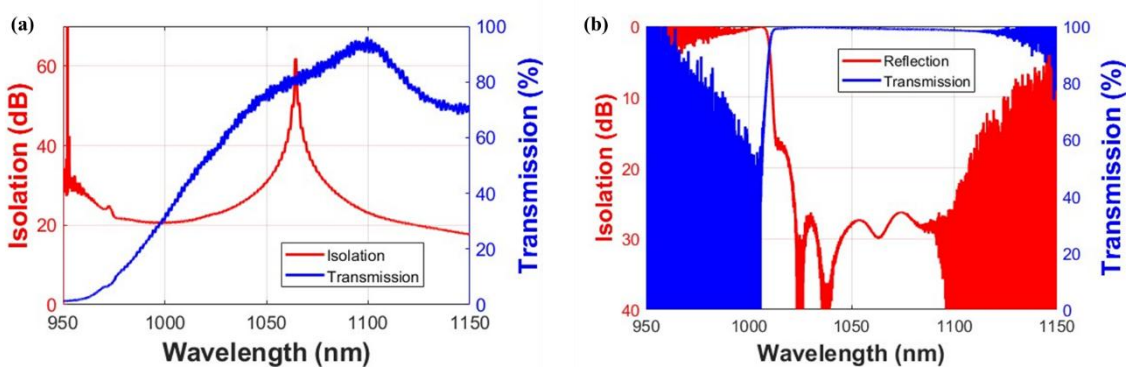

Figure 5.5: (a) Isolation and transmission spectrum of YIG based optical isolator; (b) IL and transmission as functions of wavelength of the thin-film based WDM coupler.

A single-mode YDF with a core diameter of 6 μm and a numerical aperture of 0.12 was used as the active gain medium (iXblue, IXF-YDF-6-125). The cutback method was employed to measure the absorption spectrum of YDF, using YDF lengths of 8.8 cm, 7.4 cm, and 6.1 cm. As shown in Figure 5.6(a), the average absorption spectrum indicated that the YDF exhibited a core absorption of 273.3 dB/m at 977 nm (corresponding to the core absorption of ~74 dB/m at 915 nm). The measured splice loss between the active and passive fibres (HI1060) was ~ 0.15 dB. Then, the ASE spectrum of the SS-YDFA was measured for various fibre lengths to provide a preliminary estimation of the gain bandwidth. Note that the ASE spectrum was measured under forward pumping at a pump power of 300 mW, and the output end of the fibre was angle cleaved (>8 degrees) to eliminate back reflections. As expected, as shown in Figure 5.6(b), the forward propagating ASE is strongly dependent on the active fibre length, and the ASE peak redshifts with longer fibre lengths, which is a typical characteristic of rare earth doped fibre amplifiers. Using a 12 m of YDF, a relatively flat emission spectrum was obtained, and the measured 10 dB-bandwidth was 65 nm, spanning from 1032 nm to 1097 nm.

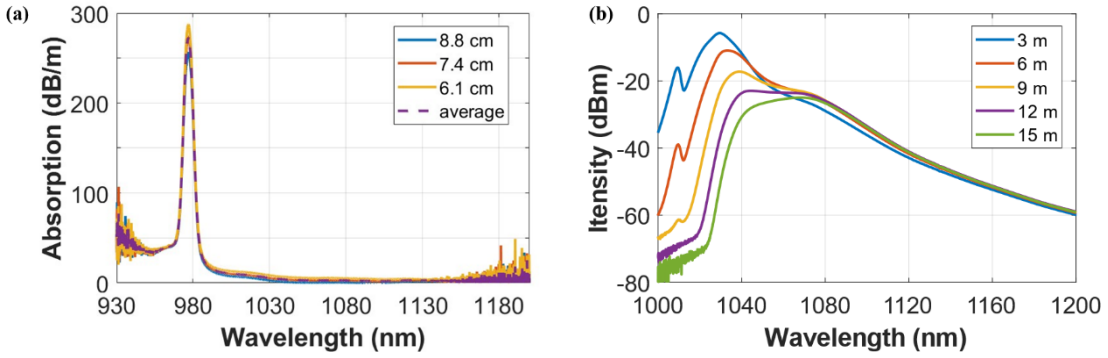

Figure 5.6: (a)Absorption spectrum of single-mode YDF; (b) ASE spectra of the SS-YDFA with different fibre lengths.

Based on the above ASE measurement and simulation results, a SS-YDFA was firstly constructed. To compare the experimental results with simulations, gain and NF spectra were measured for

different active fibre length. Figure 5.7(a) shows the measured gain and NF spectrum (scattered dots) compared with simulations (lines) for 3 m of YDF. Since the IL of YIG based isolators used in this experiment varies from 3 dB to 1 dB with wavelength, an average IL of 1.5 dB was considered in simulations. The gain increases with pump power, while the NF shows a negligible change when increasing the pump power. Under 300 mW pump power, the YDFA exhibits a peak gain of 31.2 dB at 1030 nm, as shown by blue data, and the measured gain shows 86% agreement with simulated data. The NF exhibits the maximum value of 8.6 dB at 1020 nm not only because of the ASE reabsorption at short wavelength but also due to the large IL of isolators at this wavelength. The NF performance could be optimized by replacing the YIG based isolators to erbium gallium garnet (TGG) Faraday rotator based optical isolators in the following experiment. Gain and NF at 1020 nm were also measured for different length of YDF, as shown in Figure 5.7(b). As the length of YDF increases from 2 m to 6 m, gain at 1020 nm decreases from 31.4 dB to 14.5 dB and NF degrades from 8.2 dB to 9.7 dB. This result aligns with the ASE measurements for different fibre lengths, as shown in Figure 5.6(b).

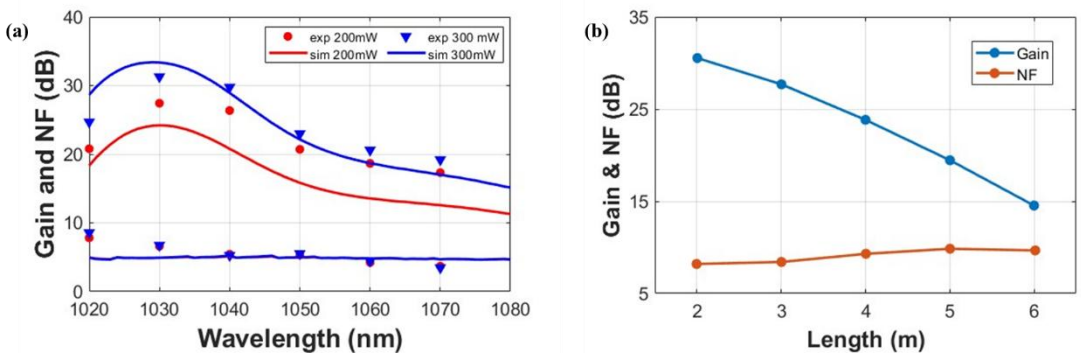

Figure 5.7: (a) Measured gain and NF spectrum in comparison with simulations for 3m of fibre length; (b) Measured gain and NF at 1020 nm versus different fibre length under 300 mW pump.

Since the gain-spectrum of amplifier depends on the input signal power, I have also characterized the gain and NF performance for different input signal power (-20 dBm/ch and -5 dBm/ch) at 300 mW of pump power and 3 m of the YDF length, as shown in Figure 5.8. This device provides higher gain at lower input power (-20 dBm/ch) compared to higher input power (-5 dBm/ch), particularly in short wavelength region below 1040 nm. This is because, at higher input signal power levels, the amplifier tends to saturate due to the depletion of the excited ion population, resulting in decreased inversion and gain, and increased NF. Comparing the gain at -20 dBm/ch input signal power, which shows a 13.4 dB gain variation (defined as the maximum gain minus the minimum gain), a relatively flat gain of average 20 dB with 4.4 dB's gain variation was observed for -5 dBm/ch input signal power. Note the gain saturates at high input power, the NF remains relatively stable due to the simultaneous saturation of ASE. Referring to the ASE spectrum shown in Figure 5.6(b),

where 12 m of YDF exhibits a relatively flat emission spectrum beyond 1040 nm, the performance of YDFA with 12 m's YDF was characterised in the following.

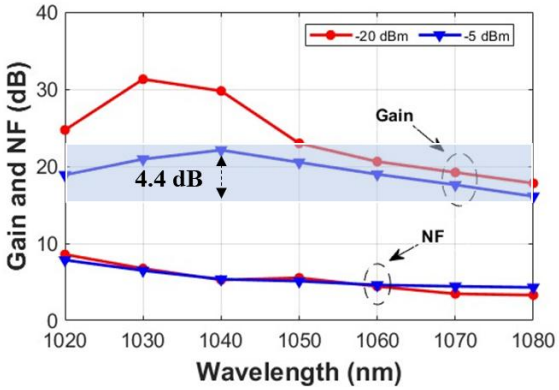

Figure 5.8: Gain and NF spectrum with different input signal power when pump power is 300 mW and YDF is 3 m.

First, the ASE spectrum of the 12 m's SS-YDFA under different pump power was measured, as shown in Figure 5.9(a). The ASE intensity level increase as the pump power increases from 100 mW to 500 mW and peak intensity slightly red shifts as the power increases. The intensity difference clearly depends on the pump power. The ASE spectrum at 400 mW pump power (purple curve) shows a relatively flat ASE with 3-dB bandwidth of 44 nm, spanning from 1037 nm to 1081 nm. Figure 5.9(b) illustrates the gain and NF spectrum of 12 m's SS-YDFA at different pump power (300 mW, 400 mW and 500 mW) in the 1040-1080 nm wavelength range. Gain increases with higher pump power levels. For each pump power level, the gain remains relatively flat across the wavelength range. For example, at 400 mW pump power, the gain is consistently around 20 dB across the wavelength range, with only a 3 dB variation. The NF remains consistently the same for each pump power level, with a maximum NF of 7.4 dB at 1040 nm.

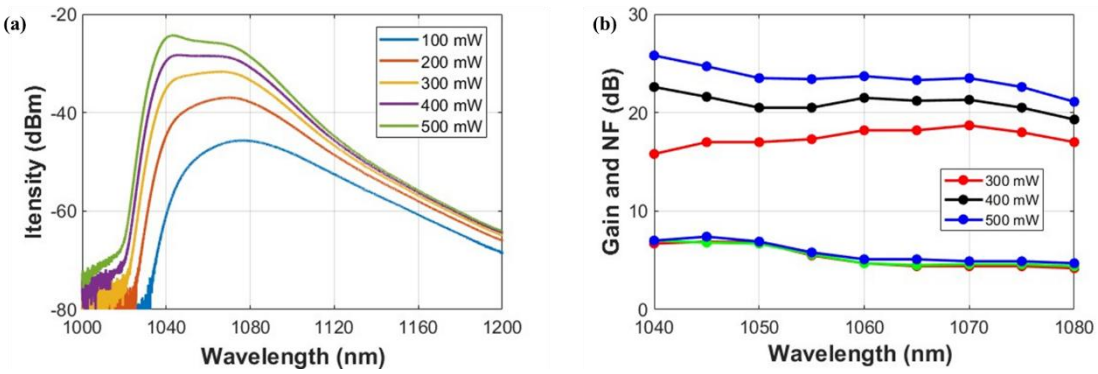

Figure 5.9: (a) ASE spectra of the 12 m's SS-YDFA under different pump power; (b) Gain and NF spectrum of 12 m's SS-YDFA with different pump power in 1040-1080 nm.

Based on the above measurement results and further simulation, a DS-YDFA was constructed using the predicted optimized fibre lengths (3 and 9 m) and the amplifier performance was characterized

in terms of the maximum gain, gain flatness and NF. Figure 5.10 plots the gain and NF performance of the DS-YDFA across the wavelength range of 1020 nm to 1080 nm for both the 1st stage (red line) and the 2nd stage (blue line). The 1st stage (red line) demonstrates a peak gain of around 30 dB at 1030 nm, with the gain gradually decreasing to around 18 dB at 1080 nm. By cascading a 2nd stage amplifier, the DS-YDFA (blue line) demonstrates a flatter gain profile, with a 10-dB bandwidth of 51 nm in the range of approximately 1026-1077 nm. The NF remains relatively consistent for each stage, with a maximum NF of 9.5 dB at 1020 nm. This indicates that the DS-YDFA provides a more consistent gain across the entire wavelength range, particularly enhancing gain performance at longer wavelength.

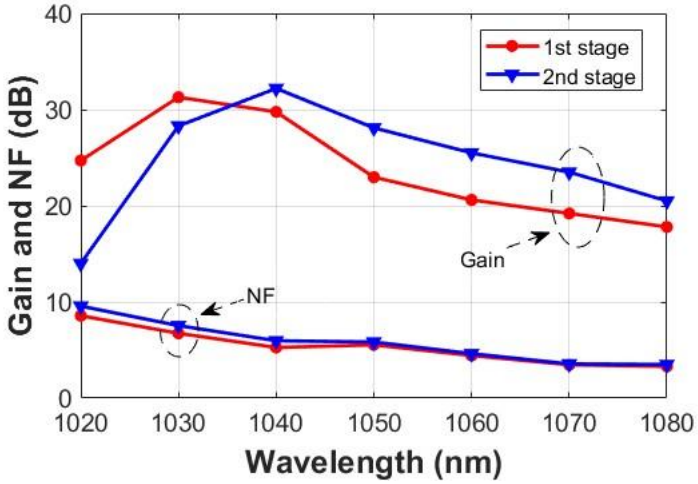

Figure 5.10 Gain and NF spectrum of a DS-YDFA in 1020-1080 nm.

5.2.3 Data Transmission Experiments at 1 µm

This subsection shows the first implementation of an error-free data transmission system at 1 µm. Using the record-low-loss single-mode NANF and in-house built wideband YDFA that shows above, a >100-Gb/s data rates over 2.24 km's NANF was achieved. The Nyquist 4-ary pulse amplitude modulation (PAM4) and capacity-maximized discrete multitone (DMT) formats were both adopted, through which the penalty-free capabilities of the NANF in terms of both bit error rate (BER) and capacity were investigated across 1020-1080 nm (i.e., a bandwidth of 16.3 THz).

I have designed and fabricated the YDFA that used in the following data transmission experiment. This transmission experiment was conducted in collaboration with Dr. Yang Hong (currently at Nokia Bell Labs Paris Saclay) and was completed while he was at the University of Southampton. The components used to interconnect SMF-HCF were fabricated by Dr. Yongmin Jung using micro-optics.

5.2.3.1 Experimental setup

Figure 5.11 shows the experimental setup of the NANF-based 1-µm transmission system. A TLS operating from 1020 to 1080 nm was used as the optical carrier to modulate a 20G-class 1-µm LiNbO3 Mach-Zehnder modulator (MZM). The MZM exhibited a 3-dB bandwidth of around 17 GHz, which was the main factor that limited the achievable data rates demonstrated in this work. An ATT was used to adjust the power to -5 dBm for all investigated wavelengths, after which an in-house built dual-stage YDFA was adopted as the booster amplifier. The amplified signal then went through either a 2.24-km long NANF or another ATT with an identical loss to the NANF at each wavelength (referred to as the back-to-back link, B2B, in the following). At the receiver, a tunable filter with a 3-dB bandwidth of 1 nm was adopted, after which a 90:10 coupler was used to monitor the input signal to the photodetector (PD). The PD exhibited a responsivity of ~0.3 A/W in the 1-µm band. Figure 5.11(b) shows the monitored optical spectra of the signals after MZM at all investigated wavelengths.

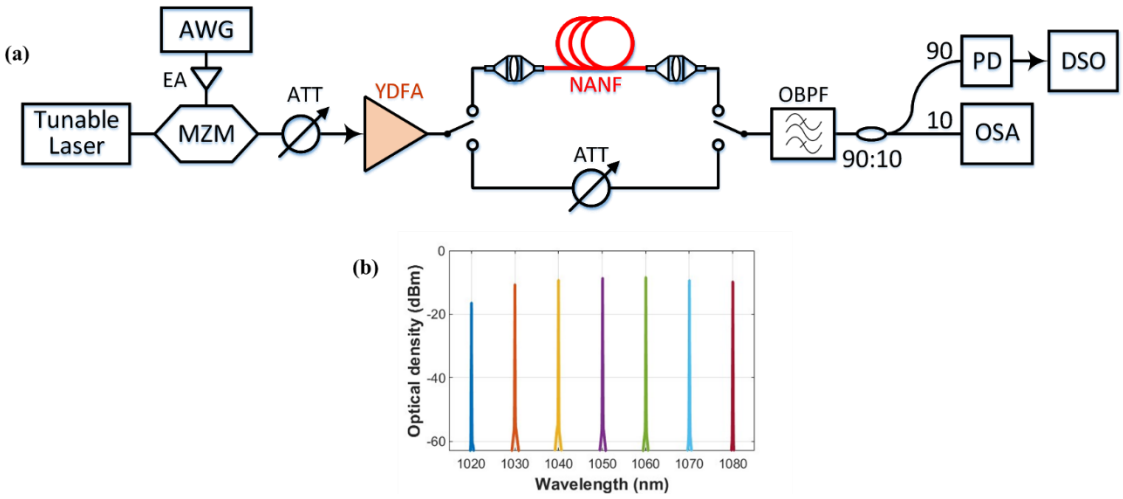

Figure 5.11: (a) The experimental setup of the NANF-based 1 µm transmission system; (b) the received optical spectra at different wavelengths.

The NANF used for the transmission experiment had a core diameter of 29.2 µm, which was surrounded by five nested tubes. The thicknesses of the outer and inner tubes were 755 and 750 nm, respectively. The fabricated NANF exhibited a record-low loss at 0.35 dB/km across 1023-1100 nm, as shown in Figure 5.12, and its cross-section scanning electron microscope (SEM) image is shown in the insert figure.

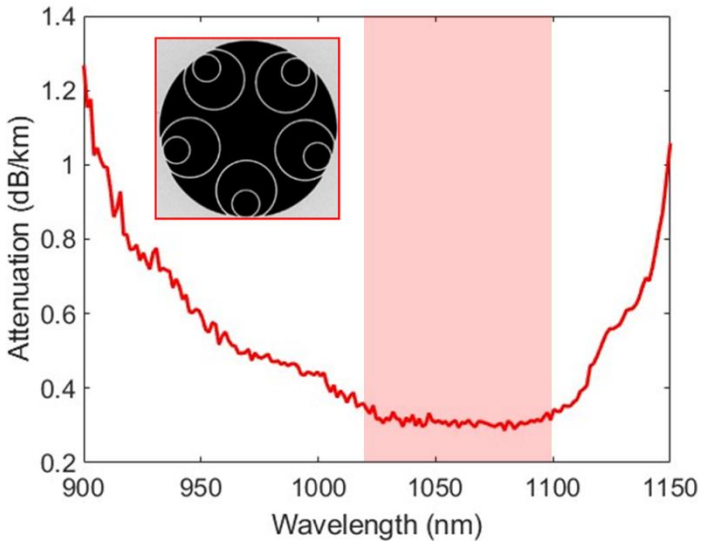

Figure 5.12 Attenuation spectrum of the NANF in 900-1150 nm.

To inter-connect the NANF with the SMF (Corning HI 1060), two micro-lenses with different focus lengths were used to mitigate the mode field diameter mismatch between two fibres (Hi1060 fibre: ~6.2 µm, NANF~20 µm). Figure 5.13(a) shows an illustration of a fibre optic collimator. The SMF was angle-cleaved to reduce the Fresnel back reflection from glass/air boundary. The total IL of the SMF-connectorized NANF was measured to ~7dB which was relatively high due to the available micro-lenses in the lab and the IL could be further optimized. Figure 5.13 shows a photo of a sealed fibre optic collimator.

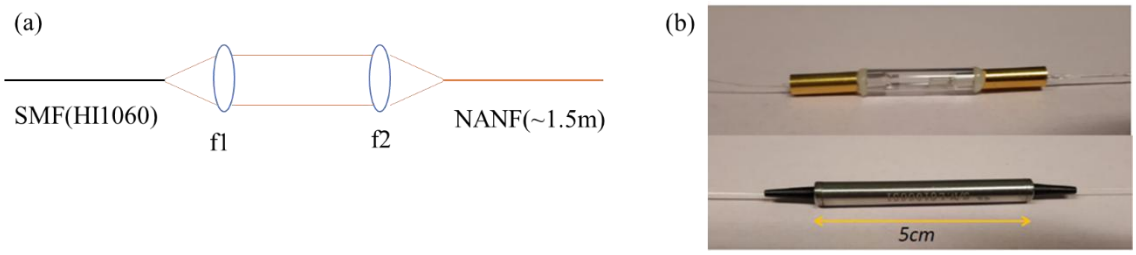

Figure 5.13: (a) An illustration of a fibre optic collimator; (b) Photo of a sealed fibre optic collimator.

To achieve optimal performance in terms of gain and NF for the YDFA at an input power of -5 dBm/channel, the dual-stage YDFA used in the transmission experiment was specifically designed. Under this input power level, increasing the input signal power generally allows for a more uniform gain profile, especially at shorter wavelengths, which is achieved by reducing the fibre length in each stage [127]. Therefore, in this design, the two stages of the YDFA were configured with YDF lengths of 3 m and 4.5 m, respectively. To ensure high output power, both stages employed forward pumping at a wavelength of 980 nm, with pump powers of 300 mW and 350 mW, respectively. As shown in Figure 5.14, the YDFA provided a gain higher than 22 dB across the spectral region of

interest, except at the shortest wavelength of 1020 nm, where the gain was around 19.5 dB. Due to the high IL of isolators and WDM, the NF remains below 10 dB across the wavelength range.

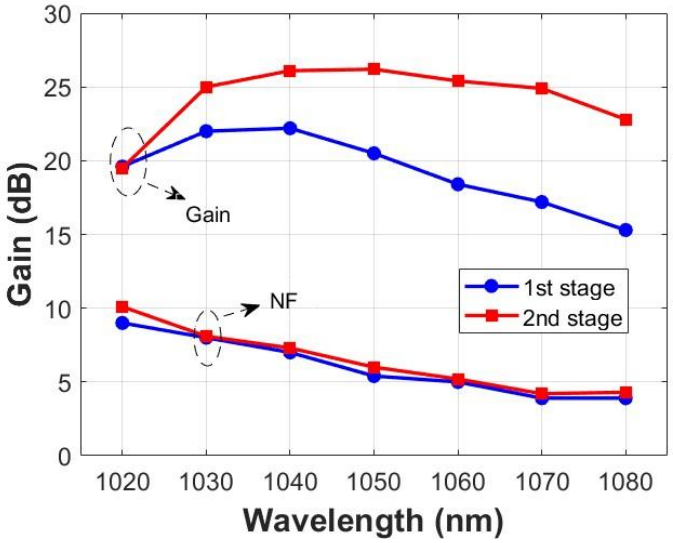

Figure 5.14: Gain profiles of the YDFA under an input power of -5 dBm.

5.2.3.2 Experimental results

We first experimented with 90-Gb/s Nyquist PAM4 across the wavelength range of 1020 to 1080 nm. Figure 5.15 shows that the BER performance was almost identical to the back-to-back (B2B) configuration when transmitting over a 2.24-km length of NANF. Furthermore, the BER performance across different wavelengths was broadly comparable, except at the shortest wavelength of 1020 nm, where the YDFA's gain was lower (see Figure 5.14). Nevertheless, the BERs of the 90-Gb/s Nyquist PAM4 transmission were well below the hard-decision forward error correction (HD-FEC) limit of 3.8×10^{-3} across the entire wavelength range of 1020-1080 nm. The slightly higher BER of the B2B case at 1080 nm, compared to the NANF transmission, is due to system instability. Without loss of generality, we take the 1060-nm case as an example and present the corresponding normalized electrical spectra of the detected signals and recovered eye diagrams in Figure 5.16(a) and (b), respectively. As expected, both the spectra and eye diagrams exhibited negligible differences between the NANF and B2B cases, owing to the low chromatic dispersion of the hollow-core NANF.

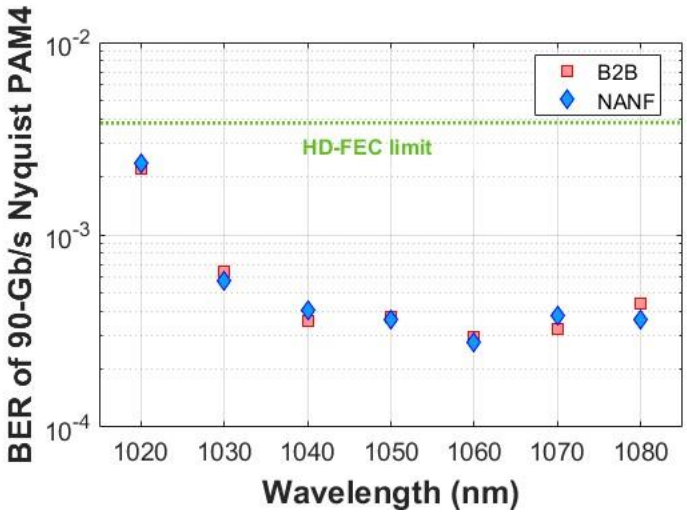

Figure 5.15: BER of the 90-Gb/s Nyquist PAM4 transmission over 1020-1080 nm.

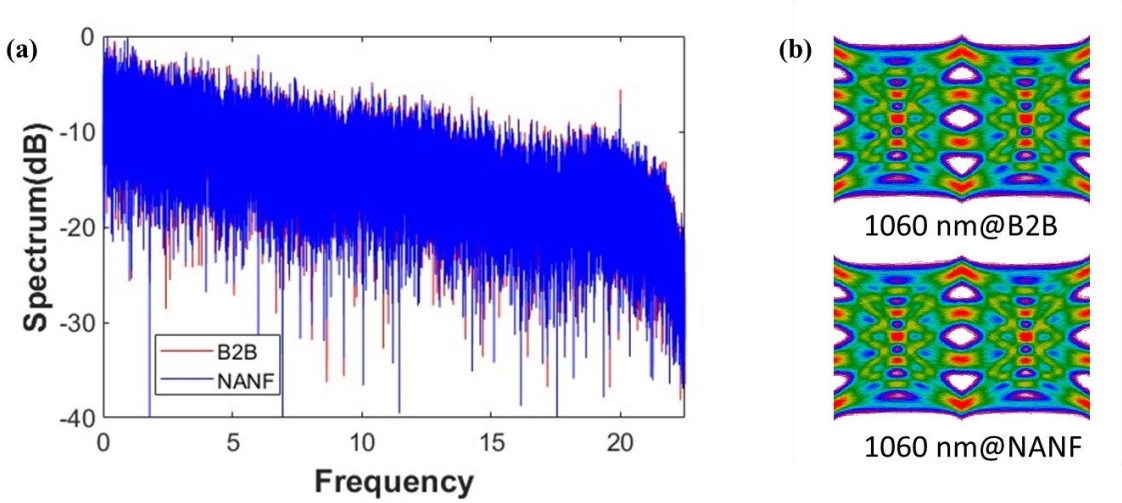

Figure 5.16: (a) normalized electrical spectra of the detected signals at 1060 nm in NANF and B2B cases, and (b) the corresponding recovered eye diagrams in the two cases.

To combat the limited bandwidth of the MZM in our NANF-based 1-µm system and maximize the transmission capacity, we further investigated the performance of the adaptively loaded DMT format. Figure 5.17 shows the achievable capacities and the corresponding BERs at different wavelengths in the NANF and B2B cases. Comparable capacities were achieved at all wavelengths in both cases, validating the penalty-free transmission in the NANF. While maintaining BERs below the HD-FEC limit, the capacities across the spectral range of 1020-1080 nm were all above 100 Gb/s, exceeding 110 Gb/s over 1030-1080 nm. Figure 5.18(a) shows the SNR profiles at 1060 nm for both the NANF and B2B cases. As expected, the two profiles are comparable and both exhibit a staircase behaviour to combat the high-frequency roll-off induced by the MZM. For reference, the constellation diagrams of 16QAM to 128QAM in the NANF case are presented in Figure 5.18(b). It is also worth noting that the demonstrated rates here were mainly restricted by the bandwidth of the MZM, rather than the NANF.

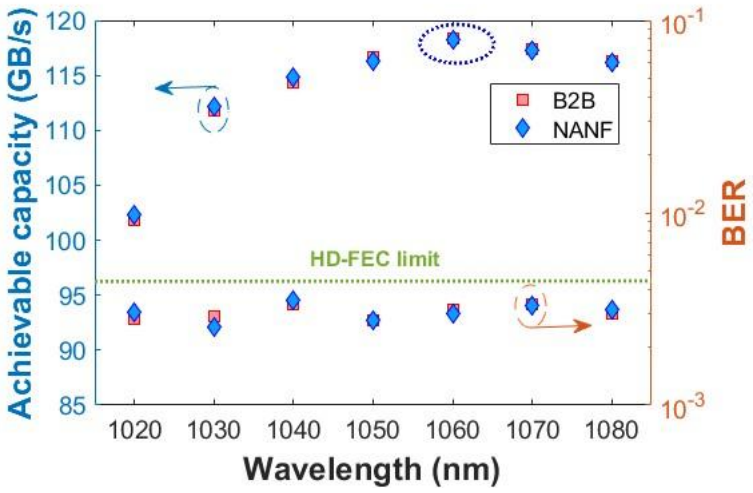

Figure 5.17: Achievable capacity and the corresponding BER versus wavelength in the NANF and B2B cases.

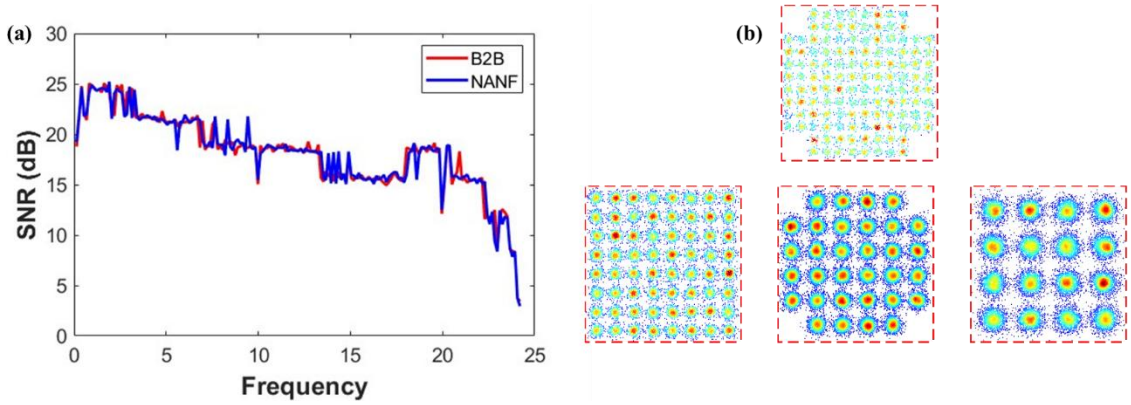

Figure 5.18: (a) the SNR profiles of the adaptively loaded DMT transmission at 1060 nm; (b) constellation diagrams of 16QAM to 128QAM in the NANF.

The performance of YDFA in the transmission was characterised using B2B method. ATT1 was used to vary the input power to the YDFA, thereby adjusting the OSNR of the amplified optical signal at the PD. ATT2 was used to fix the input power to the PD in all cases for a fair comparison. To minimize the impact of the limited bandwidth of the MZM, the data rate of PAM4 was reduced to 80 Gb/s. Figure 5.19(a) shows the BER of the 80-Gb/s Nyquist PAM4 transmission versus different OSNR at 1020 nm and 1060 nm. The BERs at both 1020 nm and 1060 nm were below the HD-FEC limit when the OSNR was greater than 30 dB. Figure 5.19(b) plots the relationship between OSNR and SNR for two different wavelengths, 1020 nm and 1060 nm. It shows that both wavelengths perform similarly across the range of OSNR values, that SNR increase linearly as OSNR increases. Notably, 1020 nm has a marginally higher SNR at higher OSNR values as OSNR increases up to 30 dB.

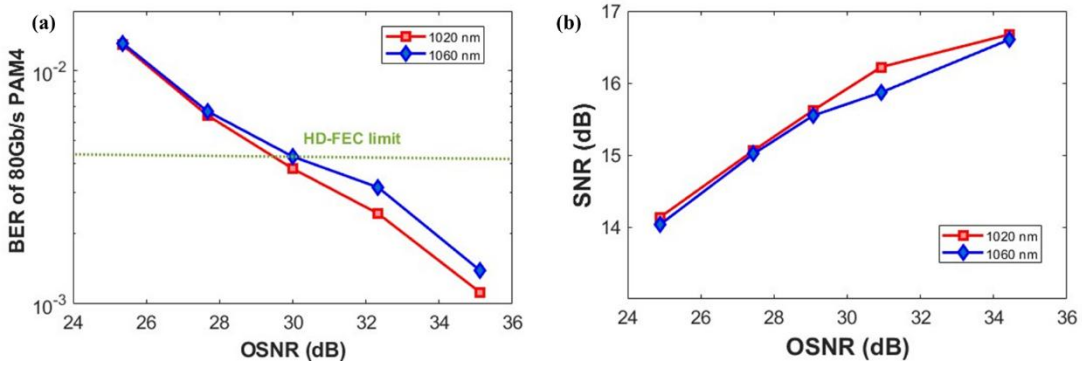

Figure 5.19: (a) BER of the 80-Gb/s Nyquist PAM4 transmission versus different OSNR using B2B method at 1020 nm and 1060 nm; (b) the SNR versus OSNR at 1020 nm and 1060 nm.

5.3 Gain-Flattened Dual-stage YDFA

In order to obtain a wideband gain-flattened YDFA, a gain flattened dual-stage YDFA (DS-YDFA) was designed, as shown in Figure 5.20. Like conventional gain flattened dual-stage EDFAs, the DS-YDFA consists of two sections of rare earth doped fibre, separated by an interstage isolator (ISO2) and a GFF. The ISO2 was applied to reject the backward ASE from the 2nd stage amplifier that would otherwise deplete the population inversion in the 1st stage amplifier. Two wavelength division multiplexing (WDM) couplers were used to combine the pump and signal wavelengths. The GFF was placed in between the amplifier stages to flatten the gain spectrum of the amplifier and to minimize its impact on the NF and output power [120]. A single-mode YDF with a core diameter of 6 µm and a NA of 0.12 was used as the active gain medium (iXblue, IXF-YDF-6-125). This choice was made to ensure good NF performance at short wavelengths in our dual-stage YDFA (DS-YDFA). Two single-mode LDs operating at a pump wavelength of ~980 nm were used to provide 300 mW of forward pumping power for each stage. The DS-YDFA's performance was measured with a power meter and an optical spectrum analyser at 0.2 nm resolution.

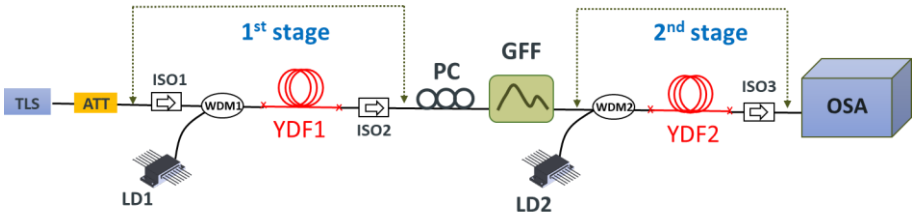

Figure 5.20: Schematic of the DS-YDFA with an interstage GFF.

5.3.1 Simulation

First, I simulated a gain-flattened DS-YDFA by applying an idealized GFF without IL whose profile was determined by the iterative optimization of fibre parameters to minimize the difference between the maximum and minimum gain (ΔG) and to provide the inverse spectral shape required in the amplifier system. Figure 5.21 depicts the gain and NF spectra of the DS-YDFA with and without this idealized GFF, respectively. In the absence of the GFF (blue line), the gain spectrum of the amplifier showed a narrow high gain peak around 1032 nm and the gain variation (ΔG) in the 1025-1090 nm wavelength range was ~10.5 dB. By employing an optimized interstage GFF, the gain spectrum (red line) was flattened to be 21.7 dB on average with less than 0.3 dB gain variation, while the NF was slightly increased from 4.4 dB to 4.6 dB (0.2 dB increment) at 1035 nm and 1075 nm due to the use of the strong GFF required (the maximum filter loss was10.3 dB) at these wavelengths, shown in Figure 5.21(b).

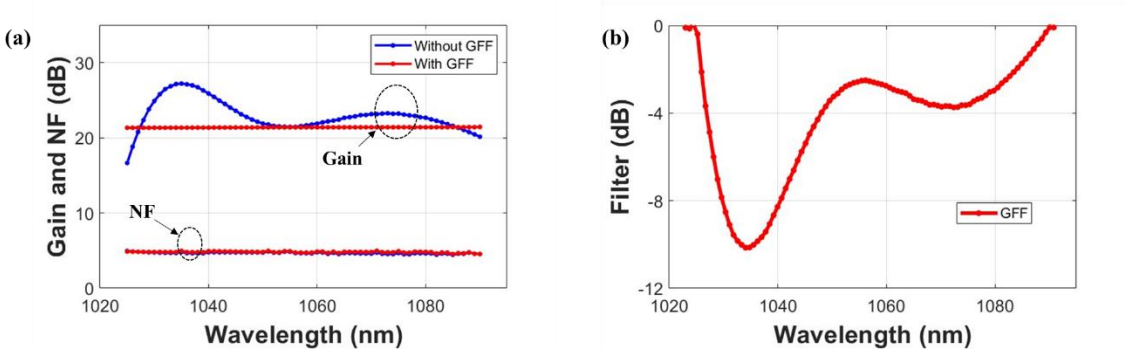

Figure 5.21: (a) Simulated gain and NF spectra of the DS-YDFA without (blue line) and with a GFF (red line); (b) the GFF spectrum used in our DS-YDFA.

5.3.2 Experimental results

Initial experiments employing YIG Faraday rotator-based optical isolators revealed significant absorption at shorter wavelengths, specifically around 1025 nm, resulting in an IL of approximately 3-4 dB as mentioned above. This high IL constrained the wideband operation of YDFAs towards the 1025 nm region, limiting their effectiveness and spectral range. To overcome this limitation, I transitioned to using terbium gallium garnet (TGG) Faraday rotator-based optical isolators. These

isolators exhibited superior transparency in the 1 µm wavelength region, demonstrating less than 1 dB IL across the entire spectral range of interest, as shown in Figure 5.22. The reduction of IL enabled more efficient and broader operation of YDFAs, enhancing its performance of gain and NF.

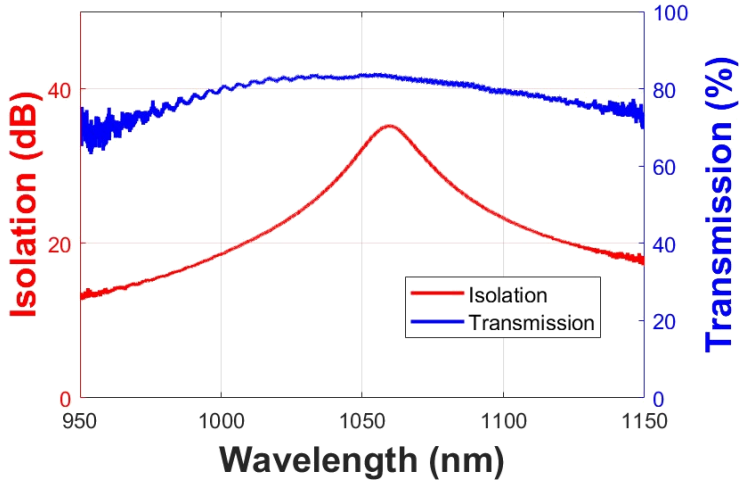

Figure 5.22: isolator characterization.

As discussed in 5.2.1, using YDF lengths of 3 meters for YDF1 and 9 meters for YDF2 results in a flat gain region from 1025 to 1097 nm. Extending YDF2 to 12 meters achieves an even flatter gain spectrum from 1028 to 1106 nm. However, due to the limited spectral coverage provided by the Gain Flattening Filter (GFF) available for the experiment (i.e., 1019-1076 nm), we intentionally selected YDF1 and YDF2 to be 3 meters and 9 meters, respectively. Due to the lack of commercial multi-channel seed sources at 1 µm, signals with wavelength tuning from 1025 to 1075 nm with a linewidth of 300 kHz for amplification. By adjusting the optical attenuator, the input signal power measured at the input of the isolator and TLS (Toptica, DL pro) was used to provide input of −20 dBm. TGG Faraday rotator based optical isolators with high transparency in the 1 µm region were selected, and <1 dB IL was observed over the full spectral range of interest. A 1 µm waveshaper (Finisar 1000s) operating in the range of 1019-1076 nm was used as a programmable GFF to provide good flexibility in controlling the filter spectral profile. The measured IL of the waveshaper was ~6 dB, with a dynamic attenuation range of 35 dB and PDL of ~2 dB. An additional polarization controller was inserted before the waveshaper to reduce the impact of the PDL from the waveshaper on our measurements. Figure 5.23 shows a photo of the DS-YDFA setup (the waveshaper not included in this photo) together with the pump LDs.

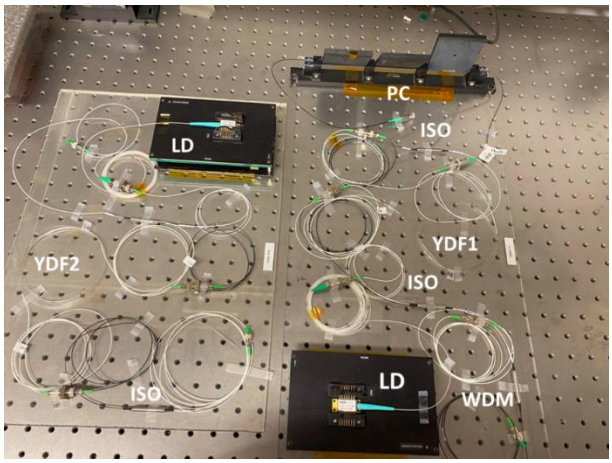

Figure 5.23 Photo of the DS-YDFA setup (the waveshaper not included in this photo) together with the LDs.

Figure 5.24(a) shows the measured gain and NF spectra of the DS-YDFA with and without the GFF at the input power of -20 dBm. Without the GFF, the DS-YDFA provided a maximum gain of 32.2 dB at 1040 nm and a gain variation of 14.8 dB. By configuring the waveshaper using the attenuation profile shown in the inset figure in Figure 5.24(a), featuring a peak attenuation of 15 dB at 1037 nm, the gain spectrum was effectively flattened with an average gain of 20 dB and a gain variation of <1 dB across the 1025-1075 nm bandwidth. The maximum NF was 4.9 dB at 1025 nm without the GFF, whereas the maximum NF of the gain-flattened DS-YDFA was found to lie at 1040 nm with a slight increase to ~5.7 dB due to the large IL of the waveshaper on top of the GFF attenuation at this wavelength. Note that the current GFF (i.e. the 1 μm programmable waveshaper) used in our experiment has relatively large IL (~6 dB) and PDL (~2 dB), but this could be addressed in the future by using static GFFs such as dielectric filters, chirped fibre Bragg gratings or long-period fibre gratings [128-130], which would further improve the NF. Figure 5.24(b) shows the output spectrum of the gain-flattened DS-YDFA in the 1025-1075 nm wavelength range at a seed wavelength sweeping step of 5 nm. The measured OSNR was >25 dB.

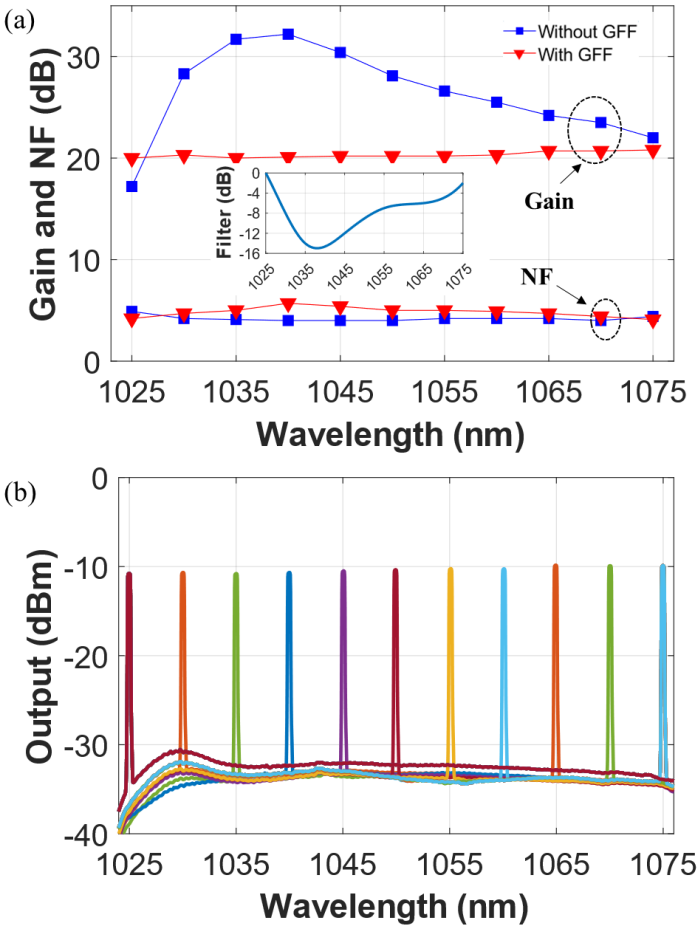

Figure 5.24: (a) Measured gain and NF spectra of DS-YDFA with and without a GFF (inset: applied GFF profile) and (b) amplified output spectra of the gain-flattened DS-YDFA under -20 dBm/ch input signal.

5.4 Conclusions

In this chapter, I have demonstrated and extensively tested the performance of wideband YDFAs in both single-stage (SS-YDFA) and dual-stage (DS-YDFA) configurations. These amplifiers are intended for use as high performance amplifiers in potential future telecommunication networks utilizing hollow-core fibres operating around 1 µm. General design considerations for wideband optical fibre amplifiers have been discussed at first and design approaches used are similar to those used for EDFAs. Then, I have explored simulation, and experimental validation of a SS- and DS-YDFA. The simulation of a SS-YDFA with a 9 m YDF length exhibited a flat gain spectrum over an 87 nm bandwidth (1023-1110 nm) with a gain of >10 dB. The NF remained relatively low (<4.3 dB) within the wavelength range of interest despite a rapid increase at shorter wavelengths due to signal reabsorption. Simulations of a DS-YDFA without a GFF indicated that optimal fibre lengths (3 m for the first stage and 9 m for the second stage) provided a bandwidth of 72 nm (1025-1097 nm) with a gain >17 dB. Extending the second stage fibre to 12 m increased the bandwidth to 78 nm (1028-

1106 nm). In the experiment validation, due to the lack of commercially available wideband seed source, a TLS operating in 1020-1080 nm was used as the seed source. Comparison between simulations and experiments was carried at first. The SS-YDFA with a 12 m YDF showed a flat emission spectrum with a 3 dB bandwidth of 40 nm (1040-1080 nm). Next, a DS-YDFA with YDF lengths of 3 m and 9 m at each stage, respectively, was characterised in terms of gain, NF and gain flatness. The results indicate that the DS-YDFA provides a more consistent gain compared to a SS-YDFA. The DS-YDFA shows improved performance with a flatter gain profile and consistent NF across the measured wavelength range, demonstrating its advantage over the SS-YDFA. Using the fabricated broadband DS-YDFA, a penalty-free transmission system was demonstrated in the 1 μm band. Despite the bandwidth limitation imposed by the 20G-class MZM, both 90-Gb/s Nyquist PAM4 and >100-Gb/s adaptively-loaded DMT transmission with the corresponding BERs below the HD-FEC limit were achieved over a bandwidth of 16.3 THz (1020-1080 nm) after transmission in the NANF.

Incorporating a GFF between the amplifier stages in the DS-YDFA effectively flattened the gain spectrum, minimizing the gain variation and improving the amplifier's overall performance. Theoretically, a gain bandwidth of 65 nm (~17.4 THz) from 1025 nm to 1090 nm with a 21.7 dB average flat gain (<1 dB variation) could be achieved. In our proof of principle experiments, a 1 μm waveshaper was used as a programmable GFF and a 50 nm gain bandwidth (1025-1075 nm) was successfully achieved, limited only by the operating wavelength range of the waveshaper. The measured average gain was 20 dB with <1 dB gain flatness, and the measured noise figure was less than 5.7 dB for signals between 1025 and 1075 nm. Importantly, the 50 nm optical bandwidth of the gain-flattened YDFA is ~13.7 THz in the frequency domain, which is almost 3.1 times greater compared to that of the C-band erbium doped fibre amplifier (~4.4 THz). While further improvements in performance can be anticipated, our results clearly demonstrate the promising potential of data transmission in the 1 μm spectral region, which could provide new opportunities for future optical transmission systems.

Chapter 6 Wideband YDFA in the 1071-1110 nm Range

6.1 Introduction

As discussed in Chapter 5, I have demonstrated a broadband gain-flattened YDFA with a bandwidth of 50 nm in the 1025-1075 nm range (~13.7 THz), as illustrated by the black circles in Figure 6.1. This is a substantial improvement in bandwidth compared to a C-band erbium-doped fibre amplifier (EDFA) (~4.4 THz), surpassing the EDFA by a factor of approximately 3.1. However, there is still considerable potential for further improvement by extending the gain bandwidth to longer wavelengths, which can be achieved by using approaches similar to those used in L-band EDFAs, including use of longer gain fibres, increased pump powers, pump wavelength optimisation and multistage designs. Despite this potential, the efficiency of long wavelength band YDFA (beyond 1075 nm) is limited by the low emission cross-section of YDFs [24]. This necessitates use of a high-power pump laser diode (>1 W), and the pump wavelength typically needs to operate away from the high absorption peak at 976 nm to balance the gain distribution over a longer length of gain fibre. In this regard, cladding-pumping offers a more attractive solution for long-wavelength band Yb-amplifiers as it uses readily available, low-cost multimode pump diodes with high output power and provides higher PCE compared to core-pumping. This is due to the reduced pump brightness in the core and hence lower level of population inversion along the amplifier length. This is favourable for amplifying signals at longer wavelengths and ultimately results in higher gain and higher PCE than core pumped approaches for longer wavelength amplification [131, 132]. This pump scheme is cost-effective and compatible with a wide range of commercially available pump wavelengths (e.g., 915 nm and 940 nm) and avoids the use of fibre Bragg grating for pump wavelength stabilization due to the relatively flat absorption of YDFs from ~910 nm to ~950 nm.

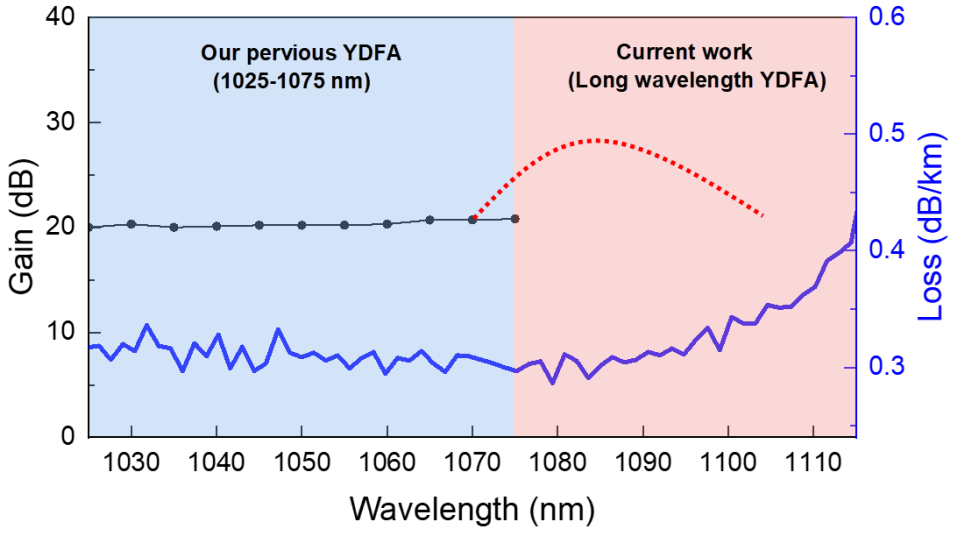

Figure 6.1: Propagation loss of HCF at 1 μm and YDFA performance in this window.

In this chapter, I presented a broadband YDFA designed for long-wavelength operation. In section 6.2, I firstly performed simulations of the SS-YDFA operating in the 1020-1120 range, comparing the performance of gain, NF and PCE under core-and cladding pumping scheme. I systematically simulated the PCE of the cladding-pumped YDFA under various conditions of input power, pump power, and pump wavelength. Due to the lack of available multi-channel seed source at long wavelengths and available MM pump diode, I also analysed the gain and NF performance of the cladding-pumped YDFA under 915 nm pumping with a single-channel seed source. In section 6.2.2, I conducted preliminary experiments, measuring the ASE spectrum for different fibre lengths and corresponding pump powers to compare with the simulation predictions discussed in section 6.2. Due to the lack of the commercially available seed source in 1070-1110 nm, I built a Yb-doped fibre ring laser to serve as a tunable laser seed source for amplifier characterization. I then characterized a simple, single-stage YDFA operating within the 1070-1110 nm range, measuring gain and NF spectra for various fibre lengths under optimized pump power. The experimental data were compared with the simulation results, and the amplifier's performance was analysed under input powers of -20 dBm/ch and -5 dBm/ch, respectively. These results validate the effectiveness of the MM cladding-pumping scheme for YDFA operation at long wavelengths, demonstrating its potential for extending the bandwidth in 1 μm transmission systems.

6.2 Single-Stage Cladding-Pumped YDFA

6.2.1 Simulations

Firstly, I employed a commercial fibre amplifier simulator (Optisystem) to evaluate the gain, NF performance and PCE of the YDFA in 1070-1120 nm. In simulations, I consider the double-clad YDF with a telecom-type fibre geometry that is practical and compatible with standard SM fibre components at 1 μm. The fibre had a core/cladding diameter of 6/125 μm and a core NA of 0.12, consistent with the single-core YDF. I assumed the YDF has a dopant concentration of 3200 ppm and typical transition cross-sections in [24]. The insertion losses for each isolator and the pump/signal combiner were assumed to be ideal (0) hereto evaluate the effectiveness of the approach. I compared the gain and NF performance of the SS-YDFA under core-pumped and cladding-pumped configurations, operating in 1020-1120 nm wavelength range. 51 WDM channels were considered as input signals with -20 dBm/ch power. Both core-pumped and cladding-pumped configurations were simulated with 1 W of pump power, with optimized fibre lengths of 20 m and 30 m, respectively. 980 nm was considered as the pump wavelength. As shown in the gain spectrum of Figure 6.2 (top), the core-pumped YDFA (blue curve) exhibited a higher gain at shorter wavelengths, peaking at 30 dB around 1035 nm. In contrast, the cladding-pumped YDFA (red curve) demonstrated a more stable gain across a broader wavelength range, maintaining a gain above 20 dB and reaching a maximum of 37 dB at 1080 nm within the 1040-1120 nm range. This stability contrasts with the core-pumped YDFA, which showed slightly lower gain at longer wavelengths. Regarding NF performance, as shown in the bottom of Figure 6.2 , the core-pumped YDFA consistently exhibited lower NF compared to the cladding-pumped configuration, with NF value remaining below 4.5 dB across the entire wavelength range for the core-pumped YDFA (blue curve), and maximum NF value of 7.8 dB for the cladding-pumped YDFA (red curve).

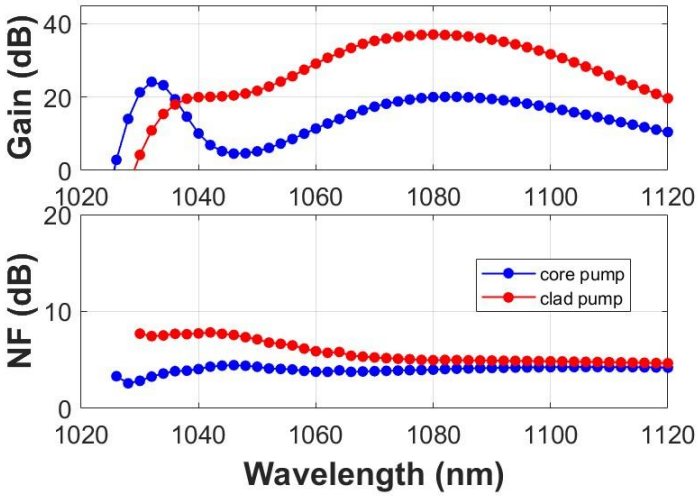

Figure 6.2 Gain and NF spectra of core and cladding-pumped YDFAs, respectively.

Next, I compared the optical PCE of the core-pumped and cladding-pumped YDFA, as illustrated in Figure 6.3. The PCE increased with increasing input power, ranging from -11.2 dBm to 8.8 dBm, for both configurations. Notably, the cladding-pumped YDFA consistently demonstrated higher PCE across all input power levels, reaching approximately 35% at the maximum input power of 8.8 dBm. This superior performance is attributed to the reduced pump brightness in the core, which leads to a lower level of population inversion a but a more uniform distribution along the amplifier's length. This characteristic is advantageous for amplifying signals at longer wavelengths, ultimately resulting in higher gain and PCE compared to core-pumped YDFA for long-wavelength amplification[131, 132].

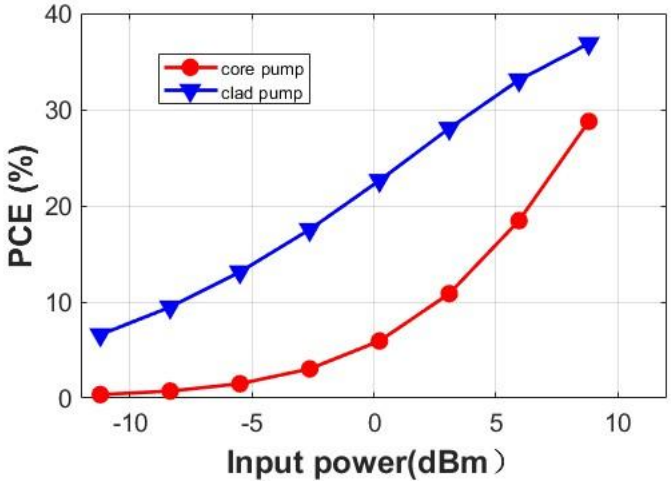

Figure 6.3: PCE as a function of input power (dBm) for core pump and cladding-pump schemes.

Figure 6.4 illustrates the optical PCE and output saturation power as functions of total pump power for different input signal levels. For a total input power of -6.2 dBm (red curve), equivalent to an input power of -20 dBm per channel, the PCE increases with increasing pump power and stabilizes around 24% in the 6-16 W pump power range. At a higher input power of 8.8 dBm (blue curve), the PCE starts at approximately 45% with 2 W of pump power and peaks at 50% with 4 W of pump power. The output saturation power is 33 dBm at 4 W of pump power. It is noteworthy that the YDF used in this study was not specifically designed for telecommunication applications. We believe that even higher PCE and output saturation power could be achieved with a YDF featuring a small core and higher NA, as this fibre design enhances the pump-signal overlap and improves pump confinement within the core, thereby increasing the efficiency of pump absorption and energy transfer [133].

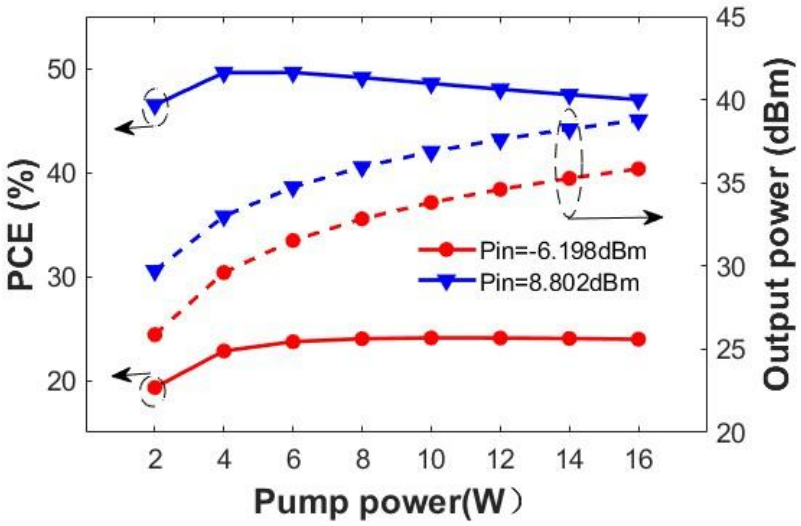

Figure 6.4 Optical PCE and output saturated power as a function of total pump power for different input signal power.

Figure 6.5 shows the PCE as a function of input power for three different pump wavelengths: 915 nm, 980 nm and 1030 nm. All three pump wavelengths exhibit a similar trend, with a steady increase in PCE as input power increases. The 980 nm and 915 nm pump wavelengths display comparable performance across the entire input power range. However, the PCE for the 1030 nm pump wavelength is consistently higher than for 915 nm and 980 nm at all input power levels, achieving a maximum PCE of 60% at an input power of 10 dBm. Due to the unavailability of a 1030 nm MM-pump diode and the fact that the 915 nm pump wavelength operates away from the high absorption peak at 976 nm—which could help balance gain distribution over a longer length of gain fibre, the 915 nm MM pump diode was selected for the subsequent simulations and experiments.

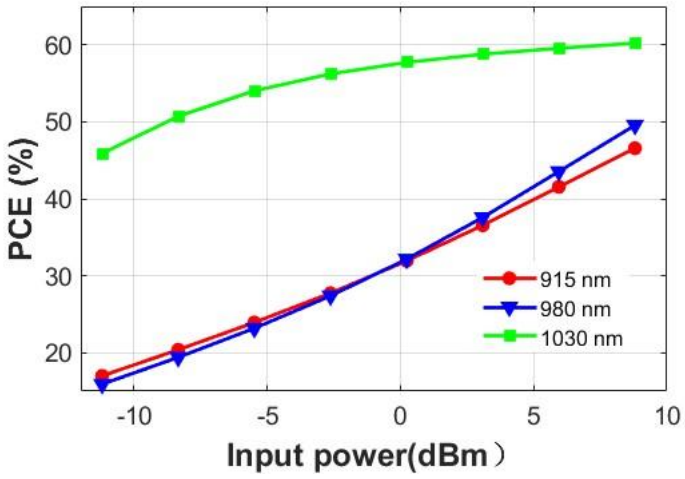

Figure 6.5 PCE vs. input power at different pump wavelengths.

Based on above analysis on the gain and PCE performance of amplifier, we conclude that 1030 nm cladding pumped YDFA is advantageous for amplifying YDFA in long wavelength region. However, due to the lack of the commercially available 1030 MM-LD and the multi-channel seed source in 1070-1110 nm, I also simulated the gain and NF performance of an SS-YDFA under a single-channel input power of -20 dBm/ch, using a 915 nm multimode laser diode (MM-LD) as the pump diode. I also accounted for the insertion losses of 1 dB for each isolator and 0.5 dB for the pump/signal combiner to ensure accurate comparison with the subsequent experimental results. Forward pump powers (0.8, 1, and 1.4 W) were used for fibre lengths of 20, 40, and 60 m, respectively (we determined these pump powers as optimal for these respective lengths). The calculated gain and NF spectra are depicted by the red, blue, and green lines in Figure 6.6. As the fibre length increases, the gain peak shifts towards longer wavelengths due to signal reabsorption at shorter wavelengths. The gain bandwidth is also dependent on fibre length. The 20-m-long YDF provides the broadest amplification bandwidth, with >25 dB gain for signal wavelengths up to 1105 nm. However, the gain

rapidly decreases for wavelength beyond 1105 nm, and longer fibre lengths are necessary to achieve >25 dB gain at these wavelengths. With a 60 m fibre length, a 43-nm-wide bandwidth extending from 1072 to 1115 nm can be achieved with >25 dB gain. The calculated NF is less than 6 dB for all fibre lengths, and the NF of a 60 m YDF is predicted to be less than 4.7 dB in the 1072-1115 nm wavelength range.

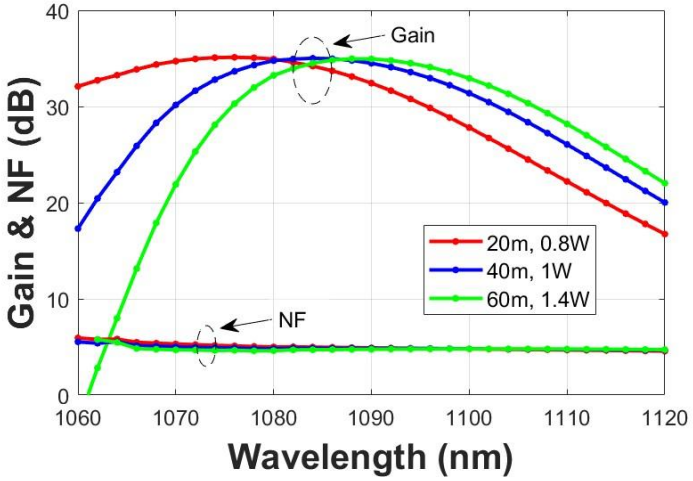

Figure 6.6: Simulated gain and NF spectra of long-wavelength YDFA at 1060-1120 nm with different fibre lengths.

6.2.2 Experiments

To begin to confirm my simulation predictions, I have undertaken some preliminary experiments. I first conducted measurement of the forward ASE spectra using various lengths of YDF to assist in optimisation of the cladding-pumped YDFA for long wavelength operation. The YDF employed in this configuration is a double-clad fibre manufactured by nLIGHT, with a core diameter of 6 µm and a core NA of 0.12. It features an octagonal-shaped inner-cladding with a diameter of approximately 125 µm and a cladding NA of 0.48 to increase the MM pump light absorption. The pump absorption at 920 nm is 0.55 dB/m in the inner cladding. The results, shown in Figure 6.7, indicate that as the YDF length increased from 20 m to 60 m, the ASE peak shifted from 1075 to 1085 nm and the ASE spectral intensity at longer wavelengths increased. The ASE spectrum had a 10 dB bandwidth of 37 nm, 35 nm, 33 nm for YDF lengths of 20 m, 40 m, and 60 m, respectively. These results suggest that increasing the fibre length further should enhance the gain at signals above 1100 nm, but this would also decrease the 10-dB bandwidth of the YDFA. In terms of the 10-dB bandwidth prediction, the results obtained from the ASE measurement showed a nearly 80% agreement with my simulations.

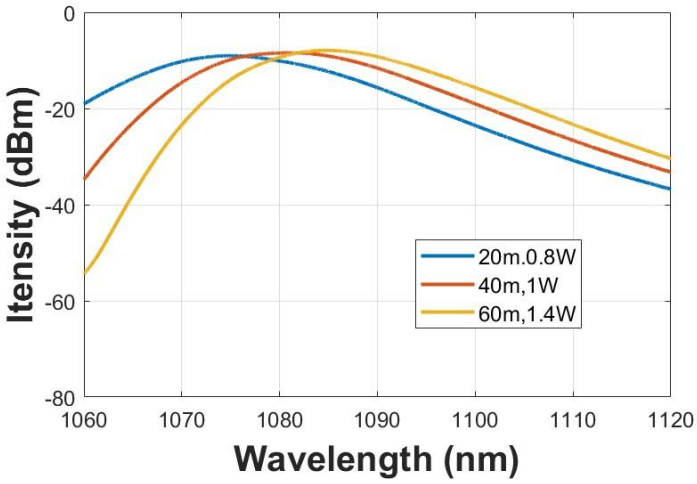

Figure 6.7: Measured ASE spectra at different YDF lengths.

Based on above simulation results and the ASE measurement, I have constructed a long-wavelength YDFA in a cladding-pumped configuration. The schematic of the amplifier is shown in Figure 6.9(a), which comprises a length of YDF, a (2+1)×1 pump and signal combiner, and two optical isolators. To forward-pump the YDF, I coupled the pump light from a commercially available 915 nm LD into the YDF via the pump and signal combiner. The power of the 915 nm LD was detected directly from the output of the LD via a thermal power sensor and the stainability of the 915 nm MM-LD was tested, as it does not have a volume Bragg grating to stabilize the central wavelength. The power of the 915 nm LD was detected directly from the output of the LD via a thermal power sensor. Wavelength stability was assessed by collecting light from the side of the output via a multimode fibre and was analysed using an OSA. Figure 6.8(a) shows the photo of this simple setup and Figure 6.8(b) presents the output spectrum measured from the multimode fibre. The central wavelength shifts from 913.6-919 nm with pump power increase from 1W to 6 W and the 3-dB bandwidth varies from 3.1 to 4.7 nm, indicating the that the central pump wavelength is situated within the flat absorption region. Isolators were inserted at the amplifier's input and output ends to minimize back reflections and prevent feedback oscillations. Additionally, the residual pump light from the YDF was removed by a high-index-coated cladding-light-stripper positioned before the output isolator.

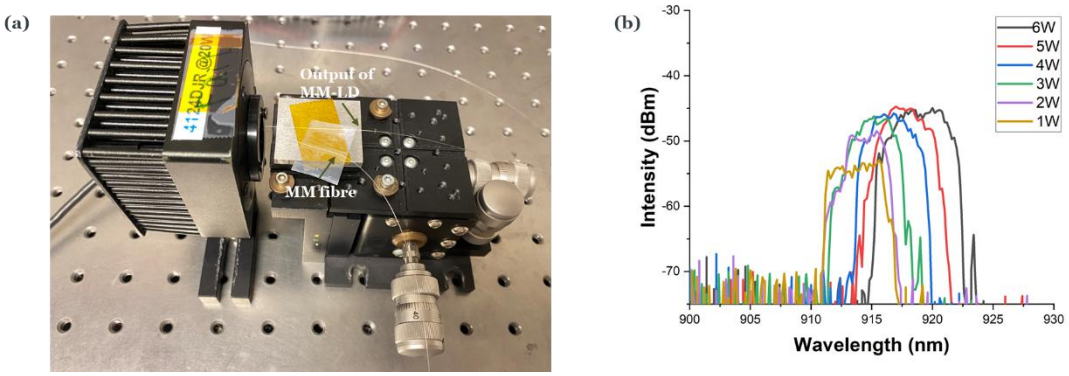

Figure 6.8 (a) Photo of the setup of measuring the wavelength stability of 915 nm MM-LD; (b) measured output spectrum of 915 nm MM-LD.

To characterize the long-wavelength YDFA, an in-house built Yb-doped fibre ring laser was used as the seed source, as no commercial TLS operating beyond 1070 nm was available. The seed laser consisted of a 1-m-long YDF (YB1200-4/125) that was core-pumped by a single-mode 980-nm pump LD. An isolator was included in the laser cavity to ensure unidirectional propagation of the oscillating laser. The output was tapped out from the cavity through the 10% port of a 90/10 coupler, and the lasing wavelength could be tuned by adjusting the tuneable band pass filter (BPF) inside the cavity. The homemade seed laser provided an operating wavelength range from 1020 to 1110 nm with a high output power. The optical signal to noise ratio (OSNR) is >40 dB for -20 dBm/ch output power and OSNR is >60 dB for -5 dBm/ch output power (measured at a resolution of 1 nm), as shown in Figure 6.9(b,c). An ATT was placed after the seed laser to control the power launched into the YDFA. The output of the cladding-pumped YDFA was characterised using an OSA and a power meter.

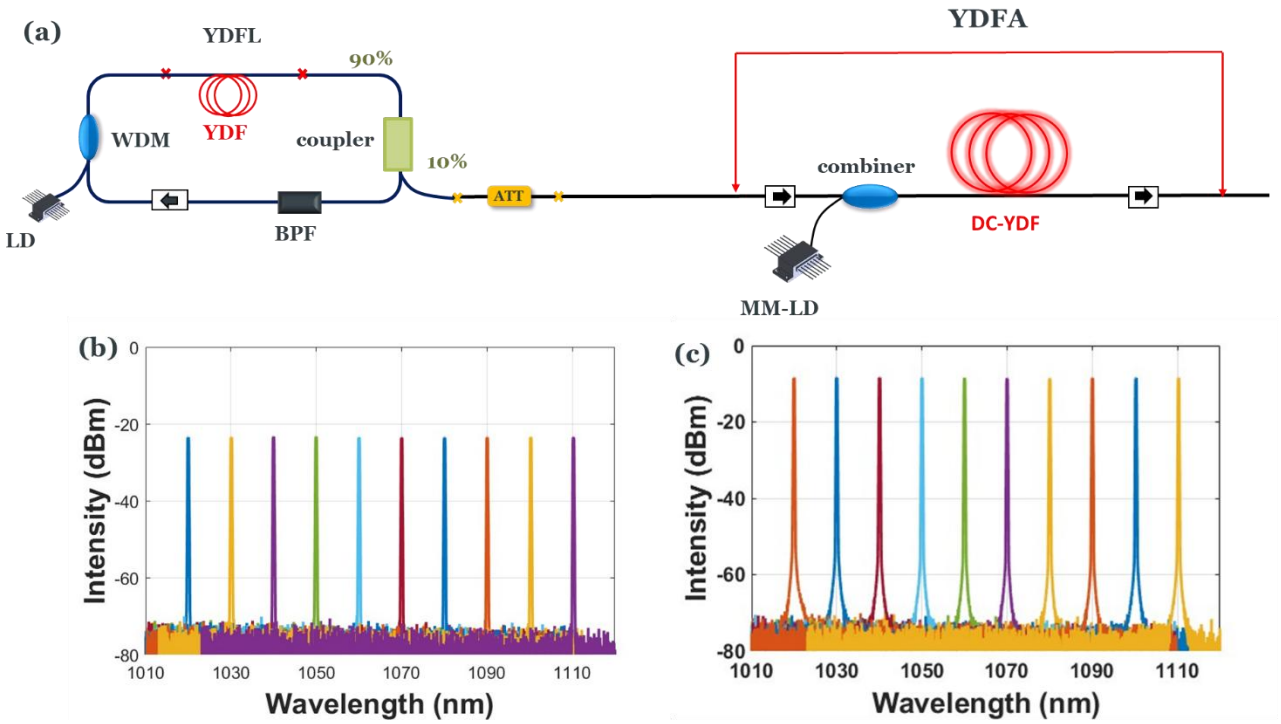

Figure 6.9: (a) Schematic of the long-wavelength YDFA in a cladding-pumped configuration; input spectrum of (b) -20 dBm/ch and (c) -5 dBm/ch from the homemade YDFL.

The gain and NF were measured for 20 m, 40 m and 60 m-long YDFA under different pump power, as shown in Figure 6.10, with an input signal power of -20 dBm/ch. In all cases, gain increased with pump power, while the NF remained steady at approximately 6 dB. As shown in Figure 6.10(a), the 20 m-long YDFA achieved a gain over than 25 dB under 0.76W pump (blue line) across a 40 nm's bandwidth in the 1060-1100 nm range. When the YDF length was increased to 40 m, the maximum gain decreased slightly from 33.2 dB to 32.3 dB, and the central wavelength shifted from 1075 nm to 1080 nm. As shown in Figure 6.10(b), over 25 dB gain was achieved under the same 0.76 W pump power across a 30 nm's bandwidth in the 1070-1100 nm range. Further extending the YDF length to 60 m, as illustrated in Figure 6.10(c), resulted in a gain peak of 27.2 dB at 1085 nm under 0.76 W pump power. A gain exceeding 25 dB was achieved in 1080-1100 nm wavelength range, with a 20 nm's bandwidth. These results indicate that the optimal pump power varies with fibre length, as higher pump power is required to compensate for increased absorption in longer fibres. Therefore, the gain and NF performance were further characterized for different fibre lengths under optimal pump power conditions.

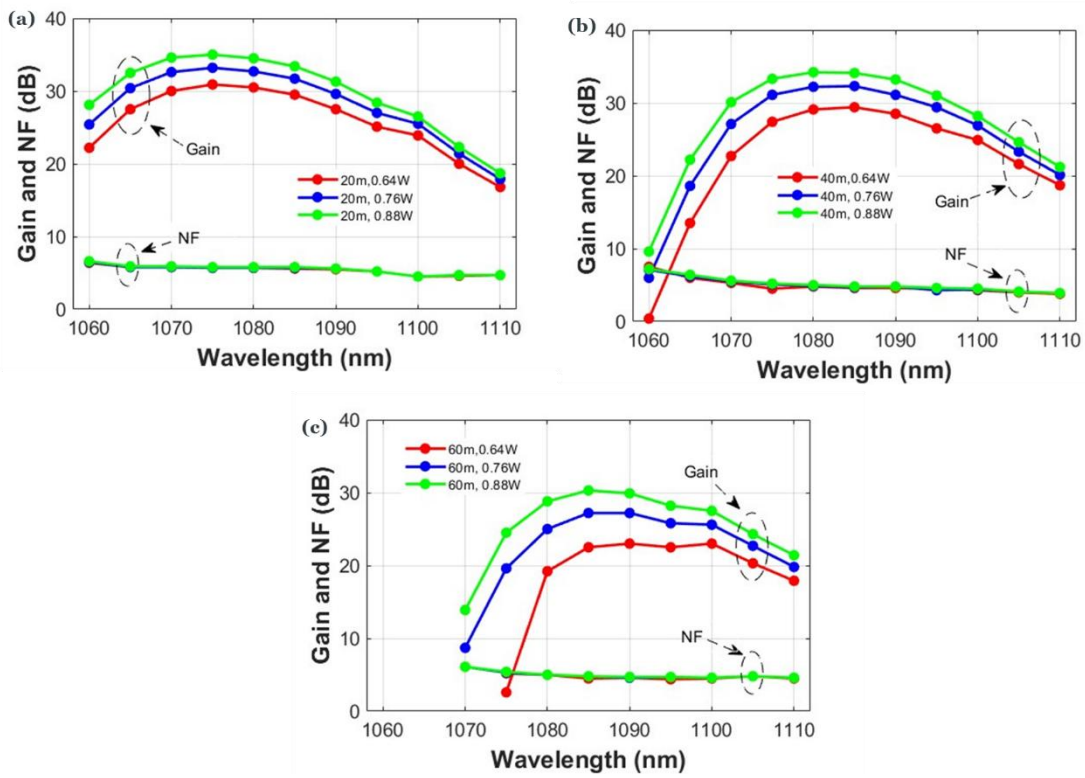

Figure 6.10: Gain and NF spectrum of the YDFA for YDF lengths of (a) 20 m, (b) 40 m and (c) 60 m respectively under -20 dBm/ch input signal power.

Figure 6.11(a) shows the measured gain and NF of the long-wavelength YDFAs using various fibre lengths with optimized pump power. The experimental data (scatter points) show good agreement with the simulation results (solid lines). The discrepancies between the experimental and simulated results can be attributed to several factors, such as mismatches between the emission cross-section values used in simulations and those of the actual fibre, coupling losses introduced by optical connectors in the experimental setup, wavelength-dependent IL of isolators and WDMs, and measurement uncertainties associated with the OSA. Additionally, a clear trend of higher gain at longer wavelengths is observed with increasing YDF length. For 20-m length YDF with optimum 0.8 W pump power, it shows a > 25 dB gain in 1060-1100 nm with 40 nm bandwidth. Further increasing the fibre length to 40 m with corresponding pump power of 1W, > 25 dB gain could be achieved in 1065 nm-1110 nm and the peak gain is shifted to 1085 nm. Notably, a 60-m-long YDFA exhibits >25 dB gain for signals from 1070 to 1110 nm, with a NF of <6.5 dB. This 40-nm-wide bandwidth corresponds to ~10.1 THz in the frequency domain, which is more than 2.3 times that of a C-band EDFA (~4.4 THz). The output spectrum of Figure 6.11(b) shows the >25 dB OSNR.

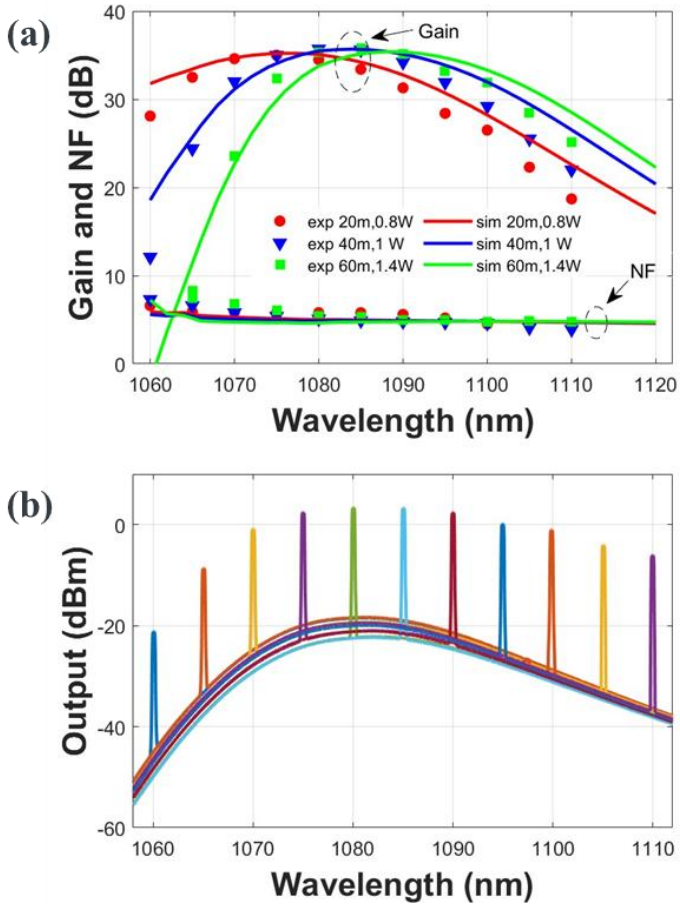

Figure 6.11: (a) Measured gain and NF spectra of the YDFA with various fibre lengths under -20 dBm/ch input signal power; (b) output spectrum of YDFA in 1060-1110 nm.

The gain and NF of the cladding-pumped YDFA were also measured with an input signal power of -5 dBm/ch for different fibre lengths and optimized pump power, as shown in Figure 6.12. The results show a similar trend to those obtained with a -20 dBm/ch input signal power, where the peak wavelength shifts from 1080 nm to 1090 nm as the fibre length increases from 20 m to 60 m. Compared to the results at -20 dBm/ch input signal power (Figure 6.11(a)), the gain spectrum is relatively flat. A 3-dB bandwidth of 40 nm was achieved in 1060–1100 nm wavelength for the 20 m-long YDFA at 0.9 W pump power, and in 1065–1105 nm for the 40 m-long YDFA at 1 W pump power. Extending the YDF length to 60 m under 1.2 W pump power resulted in a 3-dB bandwidth of 30 nm, spanning 1075–1105 nm. The NF remains below 5.1 dB across this wavelength range. Notably, the gain at wavelengths beyond 1090 nm remains similar when increasing the YDF length from 40 m to 60 m. This suggests that simply extending the fibre length in a single-stage cladding-pumped YDFA is insufficient to achieve high gain at wavelengths beyond 1110 nm. Alternative amplifier designs will be explored in Section 7.3.2 to further extend the operating wavelength range (up to 1140 nm) of YDFA around 1 µm.

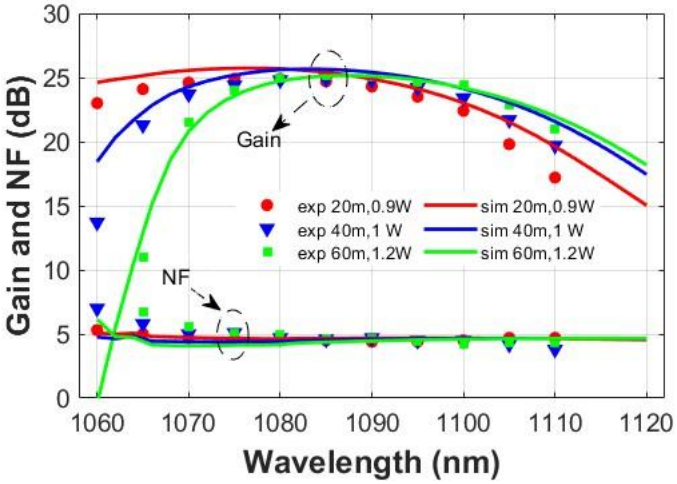

Figure 6.12: Measured gain and NF spectra of the YDFA with various fibre lengths under -5 dBm/ch input power.

6.3 Dual -stage Hybrid-YDFA with Enhanced Noise Figure

As discussed in section 6.2, the NF of cladding-pumped YDFA was degraded compared to core-pumped YDFA due to the lower pump intensity within the core, resulting in reduced population inversion and increased ASE. To enhance the NF performance of YDFA in the long-wavelength region, a hybrid pumped dual-stage configuration was proposed. The schematic is shown in Figure 6.13. A section of forward core-pumped YDFA is inserted before the cladding-pumped YDFA. The single-core YDF with a length of 5 m was forward pumped by a 980 nm LD with a power of 300 mW to maintain a good NF. The second stage employs a double-cladding YDF (DC-YDF) with a length of 60 meters, which is forward cladding-pumped by a 915 nm multi-mode laser diode (MM-LD) with a power of 0.6 W.

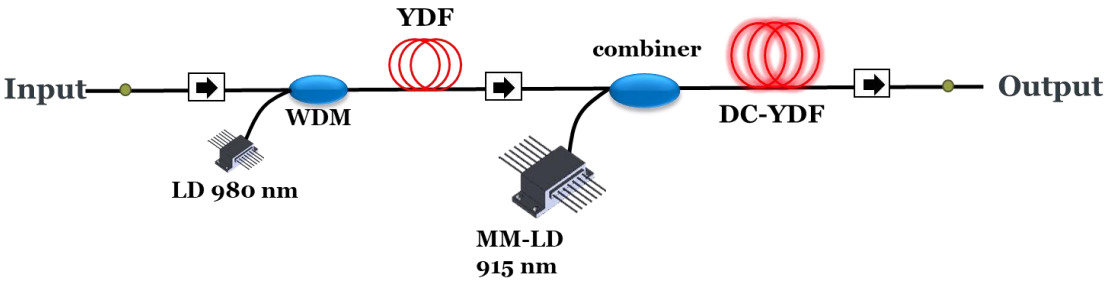

Figure 6.13 Schematic of hybrid pumped dual-stage YDFA for long wavelength operation.

6.3.1 Simulations

To compare the hybrid pump with the simple cladding-pump schemes, simulations were performed, as illustrated in Figure 6.14For the simple cladding-pumped YDFA, a fibre length of 60

m was set and a pump power of 900 mW were chosen to match the total pump power of the hybrid pumped YDFA (300 mW at 1st stage, 600 mW at 2nd stage). The figure provides a comparison of the gain and NF of the YDFA using two configurations: one with the first stage core-pumped and the second stage cladding-pumped, and the other with a single-stage cladding-pumped setup. Both configurations exhibit a peak gain of approximately 30 dB at 1094 nm. The hybrid (core+cladding) pump scheme demonstrates slightly higher gain in the shorter wavelength region of 1070-1098 nm compared to the simple cladding-pump scheme, attributed to the shorter fibre length used in the first stage, which is more efficient for amplifying relatively short wavelength region. The hybrid pumped YDFA also shows a broader bandwidth of 43 nm in the 1075-1118 nm range with a gain exceeding 20 dB, slightly wider than the 39 nm bandwidth observed in cladding-pumped YDFA (1079-1118 nm). The NF of the hybrid pump scheme remains below 4.3 dB over the 10-dB bandwidth range, presenting a 0.3 dB improvement compared to the simple cladding-pump scheme, which has an NF of 4.6 dB. This enhancement highlights the effectiveness of the hybrid core (first stage) and cladding pump (second stage) configuration in improving NF performance at longer wavelengths compared to the simple cladding-pump scheme.

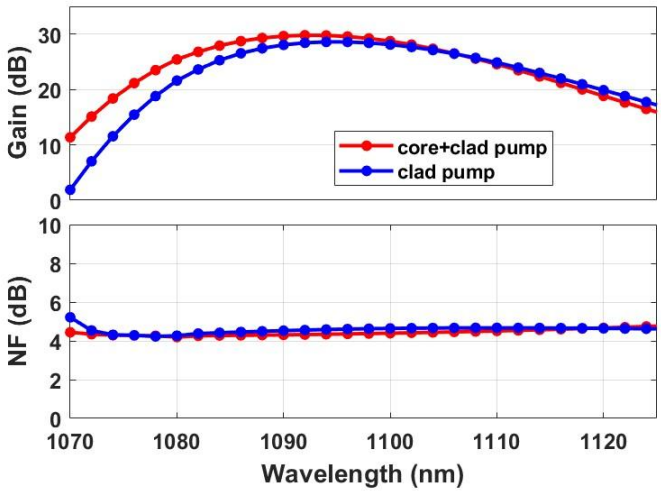

Figure 6.14: Gain and NF comparison between two different types of pumping configurations: hybrid core+cladding pumping and simple cladding pumping scheme.

6.3.2 Experiments

Followed by the simulation results discussed above, experiments were conducted to validate simulations. Figure 6.15 shows the measured gain and NF spectra of single-stage cladding pumped YDFA and dual-stage hybrid-pumped YDFA. The pump power for the single-stage cladding-pumped YDFA was set at 900 mW, ensuring that the total pump power matched that of the hybrid-pumped YDFA (300 mW + 600 mW). The experimental results, represented by scatter dots, show good

agreement with the simulations, depicted by lines. Both the cladding-pumped and hybrid-pumped YDFA demonstrate similar gain performance, achieving a 10-dB bandwidth of 35 nm within the 1075-1110 nm range with a gain exceeding 20 dB. The NF of the hybrid-pumped YDFA remains below 4.3 dB (blue dots) across the wavelength spectrum, marking a 1.1 dB improvement compared to the simple cladding-pumped YDFA, which has a maximum NF of 5.4 dB (red dots). At wavelengths beyond 1090 nm, the NF of the hybrid-pumped YDFA shows a slightly higher value, which can be attributed to the increased IL due to the additional passive components, such as isolators and WDM couplers, used in the dual-stage amplifier. Despite this, the dual-stage hybrid-pumped YDFA still exhibits superior NF performance compared to the simple cladding-pumped YDFA.

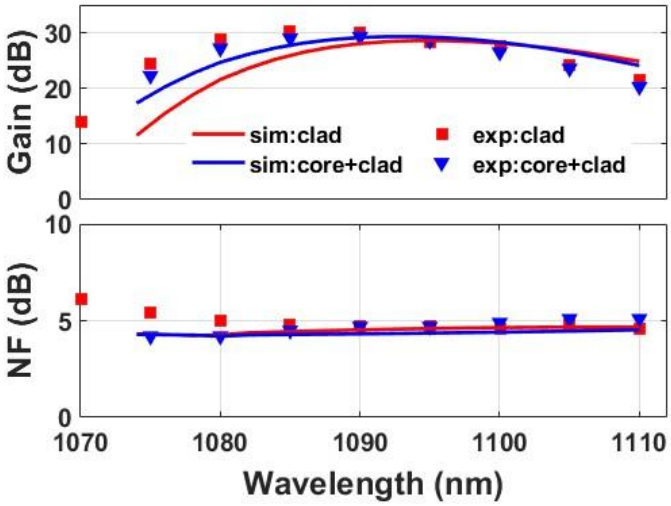

Figure 6.15: Gain and NF spectrum of single-stage cladding pumped YDFA and dual-stage hybrid pumped YDFA.

6.4 Conclusion

In this chapter, I have characterised and optimized a cladding-pumped YDFA for long-wavelength operation. The gain, NF, and PCE across various configurations, including core-pumped and cladding-pumped schemes, was studied. Cladding-pumped YDFAs exhibit a more stable and higher gain over a broader wavelength range compared to core-pumped YDFAs. Specifically, the gain is consistently higher and more stable for longer wavelengths, while core-pumped YDFAs exhibited a lower NF. Cladding-pumped YDFAs also showed higher PCE across all input power levels, reaching 50% at an input power of 8 dBm, with a saturated output power of 33 dBm. The study concludes that cladding-pumped YDFAs, especially when pumped at 1030 nm wavelength and with longer fibre lengths, are advantageous for long-wavelength amplification. However, due to the lack of commercially available multi-channel seed source and 1030 nm MM-LD, the gain and NF performance was further simulated for single-channel cladding-pumped YDFA using 915 nm pump

diode. It was observed that increasing the fibre length shifts the gain peak towards longer wavelengths, with a 60-m YDFA achieving a 43-nm-wide bandwidth (1072-1115 nm) with over 25 dB gain.

In preliminary experiments, the measured ASE spectrum showed a 10 dB bandwidth of 37 nm, 35 nm, 33 nm for YDF lengths of 20 m, 40 m, and 60 m, respectively, demonstrating an 80% agreement with simulation predictions. Using a commercially available 915 nm MM pump LD, I was able to achieve a wide gain bandwidth of 1070 to 1110 nm with a gain exceeding 25 dB and NF below 6.5 dB. The demonstrated YDFA bandwidth is ~10.1 THz in frequency domain, which is nearly 2.3 times as wide as that of EDFAs operating in the C-band. To further enhance the NF performance, a hybrid dual-stage pumping configuration was introduced. Both simulations and experimental results consistently demonstrated that the hybrid core-plus-cladding pump scheme offers significant advantages over the simple cladding-pumped configuration. Notably, the hybrid setup achieved a broader bandwidth and a lower NF across the wavelength spectrum, with a marked improvement of 1.1 dB, resulting in an NF of 4.3 dB, compared to the single-stage cladding-pumped YDFA. This advancement holds the potential to open new data transmission windows around 1 μm, thereby expanding the capacity of optical communication networks.

Chapter 7 Ultra-wideband YDFA (21.9 THz) Development and Beyond

7.1 Introduction

In this chapter, I delve into the enhancement of data capacity in single-mode fibre transmission systems, focusing specifically on bandwidth extension. While expanding the spectral window beyond the traditional C-band (~4.4 THz) to include the C+L band is a well-established solution for long-distance transmissions [134], innovative multi-band approaches are now emerging. These approaches are integrated within WDM systems, where diverse wavelength bands are combined and transmitted over a single optical fibre. In recent developments, there have been concerted efforts to combine the C-band with neighbouring E-, S- and L-bands, enabling the transmission of wideband signals spanning over 20 THz (~200 nm) [135, 136]. These multi-band systems necessitate the fusion of different amplification technologies to cover E-, S-, C- and L-bands. For instance, the integration of C+L band EDFAs with thulium doped-fibre amplifiers (TDFAs) and BDFAs has been instrumental, in showcasing transmission across the E, S, C, and L-bands over a 212 nm bandwidth (~27.8 THz) [136]. It is worth highlighting that, except for EDFAs, which have reached a significant level of maturity, other amplifier technologies exhibit various limitations. For example, despite significant advancements in recent years, BDFAs are associated with lower efficiency and typically requires 100 m lengths of gain fibre [137].

Based on the results discussed in Chapter 5 and Chapter 6, this chapter fully explores the communication window at 1 μm. Section 7.2 introduces an ultra-wideband YDFA operating in the 1025-1110 nm range. This amplifier is designed by combining two YDFAs operating in different windows (1025-1072 nm and 1075-1110 nm) in a parallel configuration, similar to the C+L band EDFAs. The proposed amplifier offers significant advantages, utilizing a simpler amplification scheme to achieve a bandwidth greater than 20 THz while delivering excellent gain and NF performance. This contrasts with recent approaches that rely on multiple bands and various amplification technologies for data transmission.

In addition to demonstrating the ultra-wideband YDFA, Section 7.3 explores the potential for extending the YDFA's bandwidth in both short and long wavelengths, similar to the S-band and extended L-band EDFAs. Due to time constraints of my PhD study, these explorations were limited to simulations. In the simulations, three different configurations for the S-type YDFA were simulated: single double-pass, partial double-pass, and three-stage YDFAs. The results suggest that

in the short-wavelength region, the bandwidth could be extended to 1002-1024 nm, achieving a 6.43 THz's bandwidth, which is 2.4 times wider than the S-band EDFA (typically 2-4 THz). For the long-wavelength extension, a high-power, low-noise extended L-type YDFA was modelled using a hybrid bi-directional pump scheme. The pump wavelength in the extended region was investigated using 915 nm, 975 nm, 1064 nm, and 1080 nm multi-mode laser diodes (MM-LD). The gain and NF performance were analysed for three different hybrid schemes: forward, backward, and bi-directional pumping.

Finally, section 7.4 provides a conclusion, summarizing the comprehensive exploration and discussion of the available bandwidth of the wideband YDFA designed for 1 μm telecommunications.

7.2 Ultra-Wideband YDFA in the 1025-1110 nm Range

7.2.1 Experimental Setup

Figure 7.1(a) presents the schematic of our ultra-wideband YDFA, designed similarly to C+L band EDFAs. This configuration combines two distinct YDFAs that are denoted as YDFA-1 operating from 1025-1072 nm and YDFA-2 from 1075-1110 nm. To generate a broadband seed source, we developed an in-house system that includes a multi-channel ASE comb source filtered by a programmable waveshaper in the 1025-1072 nm range, alongside a homemade TLS constructed from a Yb-doped fibre ring laser operating within the 1075-1110 nm range. Figure 7.1 (b) shows the spectrum of this integrated seed source which exhibits 1-dB spectral intensity variation from 1025 to 1072 nm. The total input power from the multi-channel signal was set to -5.5 dBm, corresponding to an input power per channel of -20 dBm. The single-channel TLS was set to the same spectral density and could be tuned from 1075-1110 nm. This seed source was then divided into two parallel fibre paths using a WDM splitter. In YDFA-1, two amplification stages were employed, utilizing YDF (iXblue, IXF-YDF-6-125) with different lengths (3m and 6 m, respectively), and both stages were forward-pumped by 980 nm single-mode laser diodes (SM-LDs) with an output power of 300 mW. To minimize the gain variation, a custom-made dielectric thin-film-based GFF was introduced as an interstage GFF. At the long wavelength region (1075-1110 nm), YDFA-2 employs a hybrid pump scheme with a dual-stage configuration. The first-stage amplifier was core-pumped with a 5 m-long fibre at a pump power of 300 mW to ensure good NF performance, while the second-stage amplifier is cladding-pumped to provide efficient power conversion. In our experiment, a 60 m-long double-clad YDF (nLIGHT, DCF-YB-6/125) was used. The double-clad YDF was forward pumped by a 915 nm multi-mode (MM) LD at a pump power of 600 mW to enhance PCE at longer wavelengths and to achieve better gain uniformity over the fibre length. The amplified signals, separately amplified in

the individual arms, were combined through another WDM combiner at the output port of the amplifier. The performance of this wideband YDFA was characterized by a power meter and an optical spectrum analyser. The IL from isolators and WDM couplers are below 1 dB and 0.5 dB, respectively.

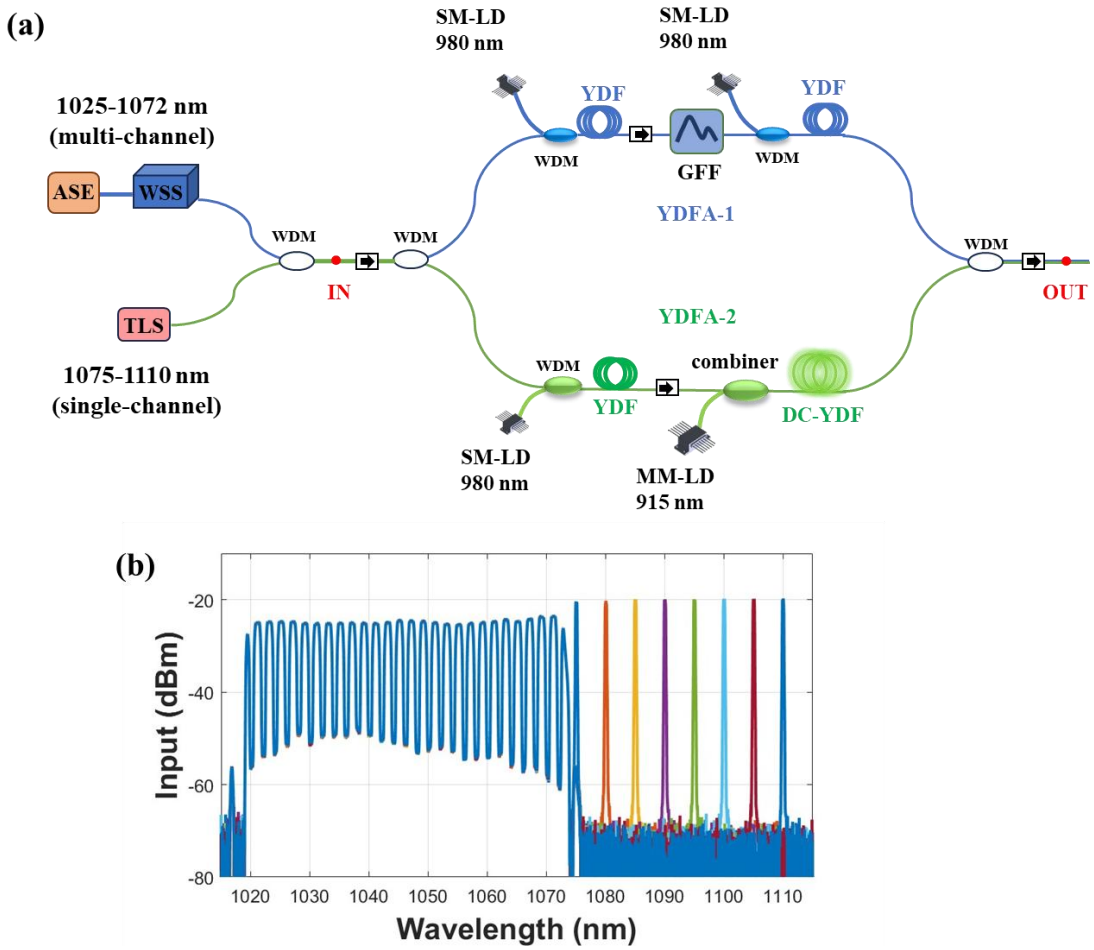

Figure 7.1: (a) Schematic of the ultra-wideband YDFA and (b) the input spectrum of the seed source.

7.2.2 Results and Discussion

I first analysed the performance of the dual-stage YDFA without a GFF. In Figure 7.2(a), the red scattered points represent the measured gain and NF spectrum of YDFA-1 without a GFF, compared to our simulation results (black curve). In the absence of the GFF, the YDFA-1 demonstrated a maximum gain of 28.2 dB at 1038 nm but exhibited significant gain variation of 13.2 dB. To mitigate this substantial gain variation, I designed and fabricated a customized thin-filed based GFF. Figure 7.2(b) illustrates the GFF profile, featuring the attenuation peak at 1035 nm with a peak attenuation of 9.7 dB, and matching the gain peak of the amplifier. The GFF exhibited an IL of ~0.5 dB and a polarization dependent loss of <0.1 dB. By incorporating this GFF between two amplifiers, YDFA-1 achieved a significantly reduced gain variation of 4 dB, with an average gain of 23 dB, as shown in

Figure 7.2(c). The measured NF remained consistently low, at < 4.2 dB. Notably, the maximum attenuation of the GFF was 2.5 dB lower than our initial design (orange curve), indicating the potential for further improvement in gain variation in the future. Nevertheless, this GFF offers compact, low-loss integration with minimal polarization dependency.

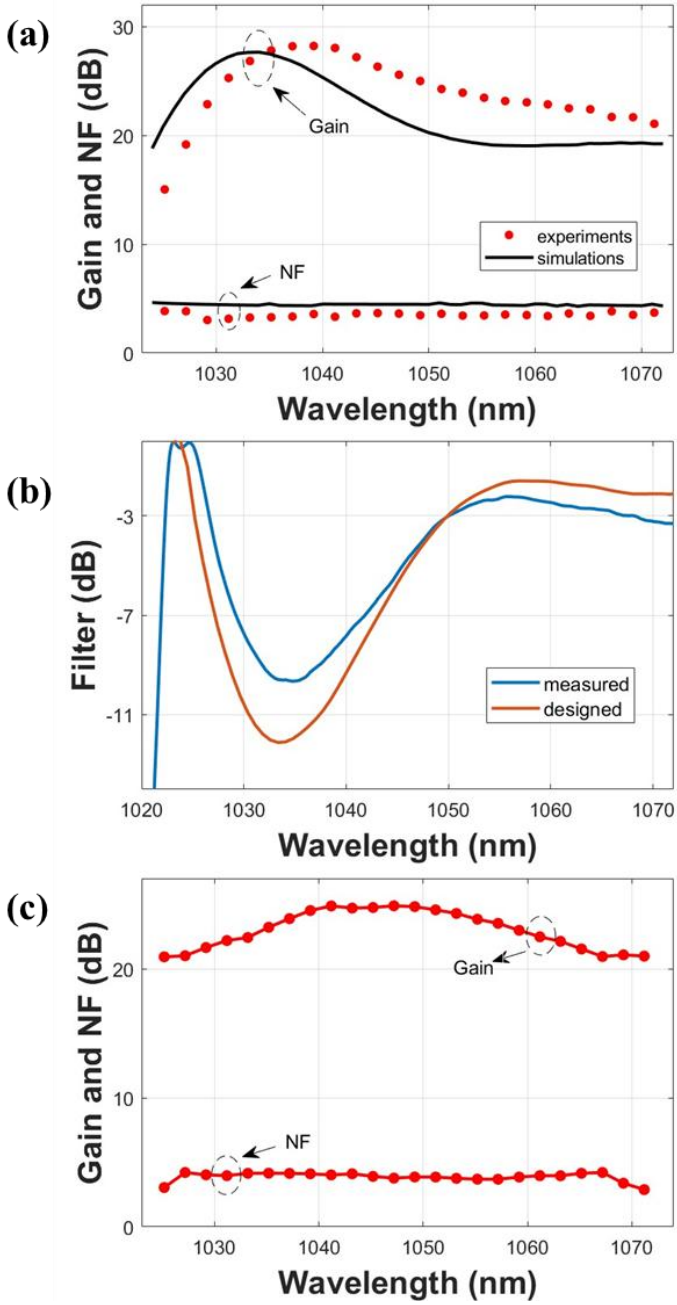

Figure 7.2: Gain and NF spectrum of YDFA-1 in the 1025-1072 nm range (a) without GFF and (c) with GFF, (b) along with the filter spectrum of the GFF (bule curve: measured, orange curve: designed).

In Figure 7.3 I present the measured gain and NF spectrum of YDFA-2 (blue scatter points), which closely align with our simulations (black solid line). YDFA-2 achieved a maximum gain of 29.3 dB at 1090 nm and maintained a gain of >20 dB for signals in the 1075 to 1110 nm range. The NF remained

below 5.1 dB, representing a 1.4 dB improvement compared to the single-stage cladding-pumped YDFA discussed in [7]. It is worth noting that the NF in this wavelength range is 0.9 dB higher than that in the 1025-1072 nm region, primarily due to the slightly increased IL of passive components, such as isolators and WDM couplers, at longer wavelengths.

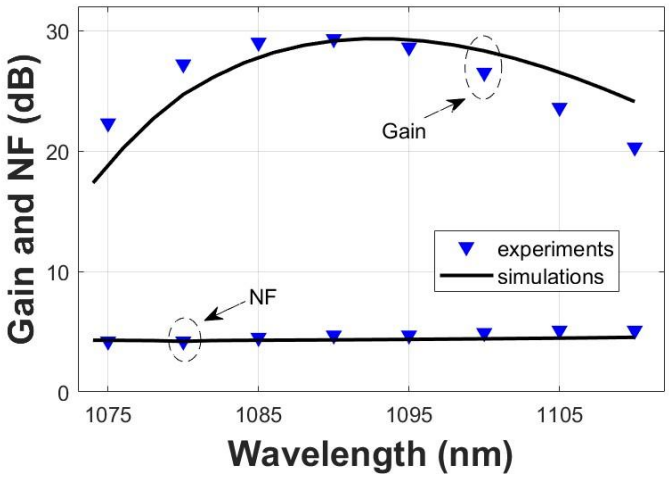

Figure 7.3: Gain and NF spectrum of YDFA-2 in the 1075-1110 nm range.

These two YDFAs are combined in a parallel configuration, and Figure 7.4(a) presents the measured overall gain and NF spectrum in the 1025-1110 nm range. The combination of 47 nm gain region from 1025 to 1072 nm and another 35 nm from 1075 to 1110 nm results in an exceptionally broad overall gain spectrum spanning 82 nm. This translates to a frequency bandwidth of ~21.9 THz, nearly double that of C+L band EDFAs. Figure 7.4(b) displays the output spectrum across the entire wavelength range, showcasing an output OSNR of >20 dB for most signal channels.

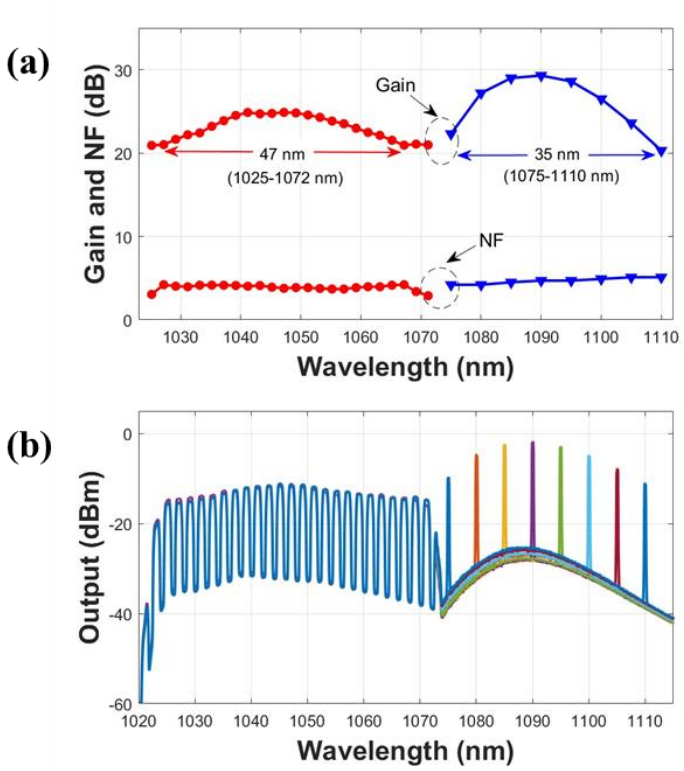

Figure 7.4: (a) Overall gain and NF spectrum in the 1025-1110 nm range and (b) output spectrum of YDFA.

7.3 Further Extension of Gain Bandwidth

In section 7.2, I have successfully built an ultra-wideband YDFA that covers the 1025-1110 nm wavelength range, achieving an impressive bandwidth of 21.9 THz. While this represents a significant breakthrough, there remains considerable potential for further enhancement by extending the gain bandwidth to encompass shorter or longer wavelengths. This potential for expansion can be realized by employing techniques similar to those used in the development of S-band and extended L-band EDFAs, which have demonstrated substantial advancements in expanding operational bandwidths [138-142]. In this section, I present a series of simulations that evaluate the performance of YDFAs designed to operate in the S-band and extended L-band regions. Given the current lack of commercially available components for these specific wavelengths and the time constraints of my PhD research, experimental validation was not possible within this timeframe. However, the simulation results are promising and demonstrate the feasibility of future experimental work to realize these extended bandwidths.

7.3.1 Short Wavelength Extension (S-band Type YDFA)

To achieve YDFA gain in the short-wavelength region (below 1025 nm), suppressing ASE is essential for improving gain efficiency and enabling effective optical amplification in the short-wavelength

region. Efficient S-band EDFAs, for instance, require high inversion levels along the fibre while suppressing C-band ASE, which can otherwise deplete the population inversion and reduce efficiency. In S-band EDFAs, C-band ASE suppression is often achieved by leveraging the fundamental-mode cutoff of depressed-cladding doped fibres [143, 144] or by incorporating multiple filters within the amplifier module [139]. Given the current lack of YDFs specifically designed for short-wavelength amplification, I employed commercially available YDF parameters in my simulations. The fibre used had a core diameter of 6 μm, a cladding diameter of 125 μm, and a cutoff wavelength of 1000 nm. The design of the amplifier plays a pivotal role in ensuring high gain and a low noise figure across the entire amplification wavelength range. As an alternative approach, I also referenced the use of conventional EDF in the S-band, particularly in a double-pass configuration, to optimize gain in S-band YDFAs. Additionally, I considered the multi-stage EDFA configuration, which cascades multiple standard erbium-doped fibre sections with optical filters interstage to reduce ASE power from the C and L bands, as a model for amplifying short wavelengths with YDFA. These configurations are designed to replicate the success observed in S-band EDFAs, ensuring that the YDFA can deliver high gain and maintain a low noise figure across the desired wavelength range.

7.3.1.1 Single-stage double pass configuration

The configuration of the core-pumped double-pass S-band YDFA, modelled after the design of S-band EDFAs, is illustrated in Figure 7.5. This setup employs a relatively short length of YDF to minimize the signal reabsorption at short wavelengths, thereby enabling amplification in the short-wavelength region. The system is pumped with a 915 nm laser diode, which operates at a wavelength further from the amplification range (1000-1024 nm) than 980 nm, and the pump power is set to 800 mW. A forward pumping scheme is utilized, with a pump absorption of 70±5 dB/m. At the input end, an optical circulator (OC1) directs the amplified signal into an OSA for performance evaluation. At the output end, a second optical circulator (OC2) is used, where port 1 is connected to port 3, enabling the double propagation of the test signal through the YDF. This configuration allows the signal to pass through the fibre twice, enhancing the amplification process. 13 WDM channels at wavelengths between 1000-1024 nm with a 2 nm channel spacing were considered as the seed source (-20 dBm/ch). For comparison, the amplifier's performance in the double-pass configuration is evaluated against a single-pass configuration, which is achieved by disconnecting ports 3 and 1 of OC2.

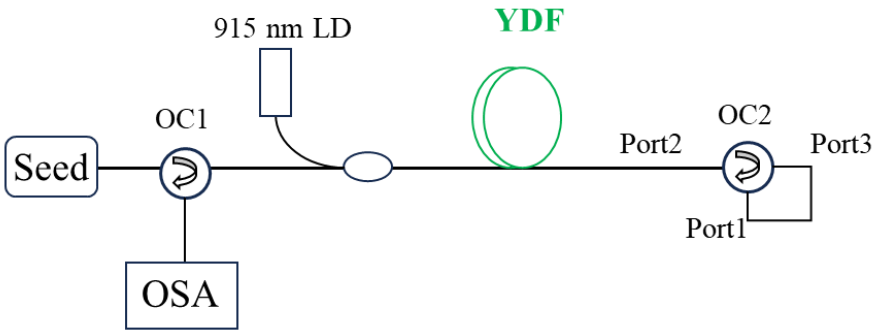

Figure 7.5: Configuration of the single-stage double-pass S-band YDFA.

Figure 7.6 presents the gain and NF spectra of a double-pass YDFA across different fibre lengths (0.5 m, 1 m, 1.5 m, and 2 m) for the wavelength range of 1000 to 1024 nm. It indicates that shorter fibre lengths are advantageous in increasing gain at shorter wavelengths. This phenomenon occurs because longer YDFs tend to saturate at longer wavelengths, leading to a reduction in gain at shorter wavelengths due to a decrease in the average inversion level. Furthermore, the spectra shows that the NF increases as the fibre length increases. The maximum NF observed for the double-pass amplifier is approximately 7 dB when the fibre length is 0.5 m. Note that in the following simulations, the NF is occasionally slightly lower than the quantum limit of 3 dB. This is due to the settings used in the calculation: a noise bin spacing of 1 nm and a noise dynamic of 3 dB. While finer settings would improve the accuracy, they would also significantly increase computation time, particularly given the long fibre length. Nonetheless, the results remain valid and are sufficient for analysing the general trend.

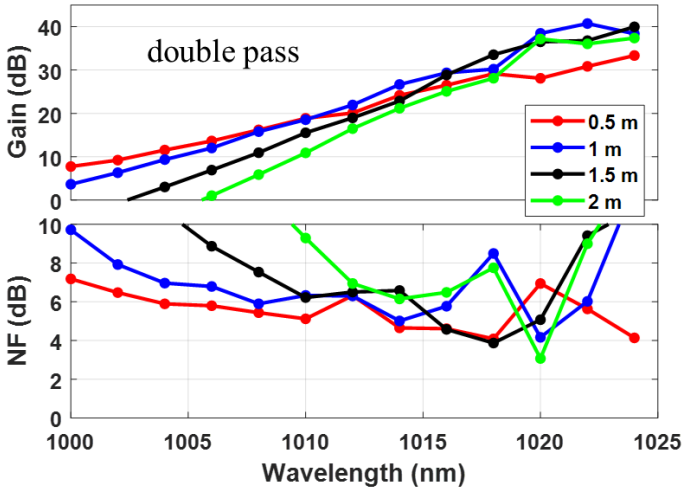

Figure 7.6: Gain and NF spectra versus different fibre length for double-pass amplifier in 1000-1024 nm.

Figure 7.7 compares the gain and NF spectra between single-pass and double-pass YDFA configurations. The gain spectrum (top) clearly show that the double-pass amplifier achieves a gain

approximately 10 dB higher than that of the single-pass amplifier. This gain enhancement is attributed to the double propagation of the signal through the amplifier, which effectively increases the ASE level, particularly in the short-wavelength region. However, this gain improvement comes at the cost of increased NF. The double-pass configuration introduces more counter-propagating ASE, which reduces the population inversion at the input section of the amplifier, leading to a higher NF. As depicted in the bottom of Figure 7.7, the NF for the double-pass amplifier (~7.5 dB) is approximately 4 dB higher than that of the single-pass configuration (~3.5 dB). This suggests that while the double-pass amplifier significantly boosts gain, it also introduces a trade-off in the form of increased noise, highlighting the importance of balancing these factors in amplifier design.

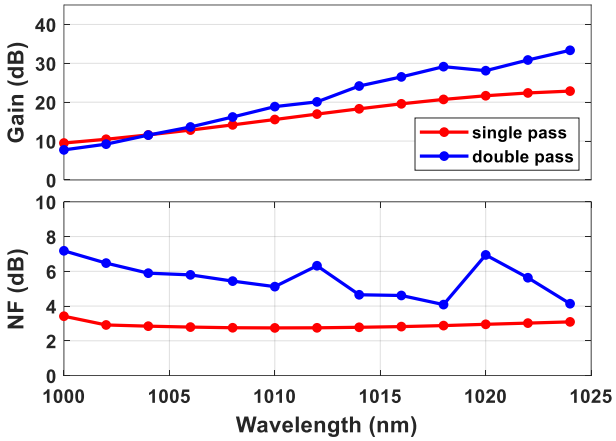

Figure 7.7: Comparison of the gain and NF spectra between single-pass and double-pass amplifiers.

7.3.1.2 Partial double pass configuration

To solve the problem of the high NF in the double-pass amplifier, a partial double-pass S-type YDFA design is introduced. This design aims to combine the advantages of low noise and high gain by employing a structure similar to that of a multistage amplifier. Figure 7.8 illustrates the schematic of the partial double-pass S-band YDFA design. In this configuration, the first stage uses a short length of forward-pumped YDF to maintain low noise characteristics, while the second stage utilizes a double-pass configuration to achieve higher gain, as detailed in 7.3.1.2. Both stages utilize 0.5 meters of YDF, each forward-pumped by a 915 nm laser diode with a power output of 800 mW. To achieve a flattened gain across the S-band, an ideal GFF is placed after the second YDF (YDF2).

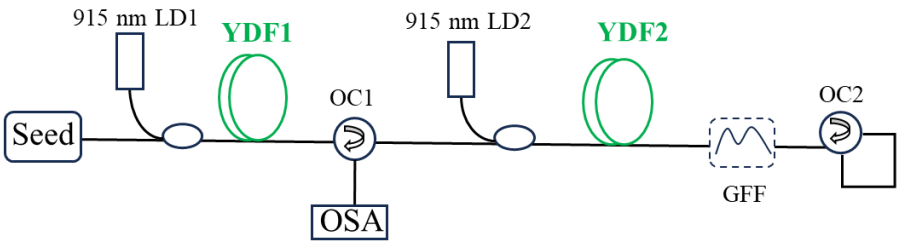

Figure 7.8: Schematic of the partial double-pass S-band type YDFA design.

The amplifier's performance is compared with a single-pass and double-pass configuration discussed in section 7.3.1.1, as illustrated in Figure 7.9. The gain spectrum shows that the partial double-pass amplifier consistently delivers the highest gain, outperforming both the single-pass and double-pass configurations, particularly as the wavelength approaches 1024 nm. At the longest wavelengths, the partial double-pass configuration achieves a maximum gain of nearly 40 dB. In terms of NF, the partial double-pass amplifier maintains a low NF, staying below 4 dB across most of the spectrum. This represents a significant improvement over the double-pass configuration, which exhibits higher NF values, exceeding 6 dB at certain wavelengths. The partial double-pass design achieves more than a 2 dB improvement in NF within the 1006-1024 nm range compared to the double-pass configuration. This improvement is attributed to the strategic placement of the forward-pumped YDF1 section before OC1. By preventing the amplified signal and backward ASE from propagating back into the input section (YDF1), OC1 ensures that the population inversion in the YDF is minimally affected by intense light, thereby maintaining a low NF. Overall, the partial double-pass amplifier offers a noise figure comparable to that of the single-pass configuration, while providing a significantly higher gain—exceeding 20 dB in the 1006-1024 nm range. This makes the partial double-pass design a highly effective solution for achieving both high gain and low noise in S-type YDFAs.

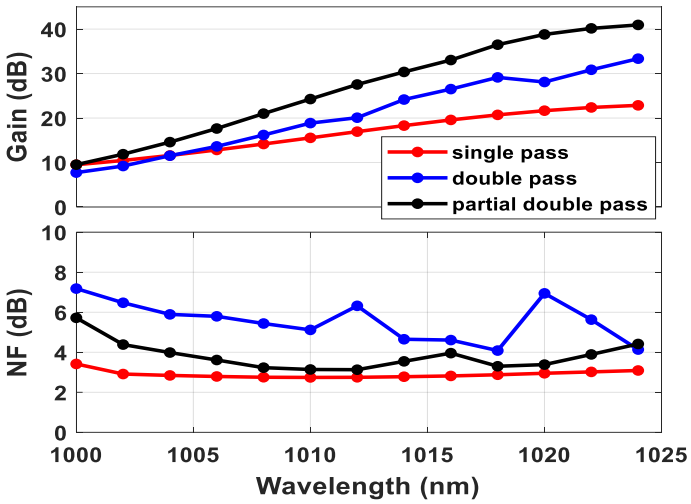

Figure 7.9: Comparison of Gain and NF between single-pass, double-pass and partial double-pass S-type YDFAs.

Finally, I developed an S-band type YDFA with high flattened gain and low NF by inserting a GFF before OC2 of the partial double-pass YDFA discussed above. Figure 7.10(a) compares the gain and NF spectra of the amplifier with and without the GFF. Without the GFF, the S-band YDFA achieves a maximum gain of up to 40 dB at 1024 nm but exhibits a significant gain variation of 20 dB across the wavelength range from 1008 nm to 1024 nm. To address this variation, I introduced an idealized GFF before OC2. The GFF is designed to introduce maximum attenuation at 1030 nm, with a peak attenuation of 25 dB, as shown in Figure 7.10(b). With the idealized GFF, the S-band type YDFA achieves an average gain of 20 dB with less than 1 dB of variation across the wavelength range from 1006 nm to 1024 nm. The NF remains below 5 dB, with only a 1 dB increase compared to the amplifier without the GFF.

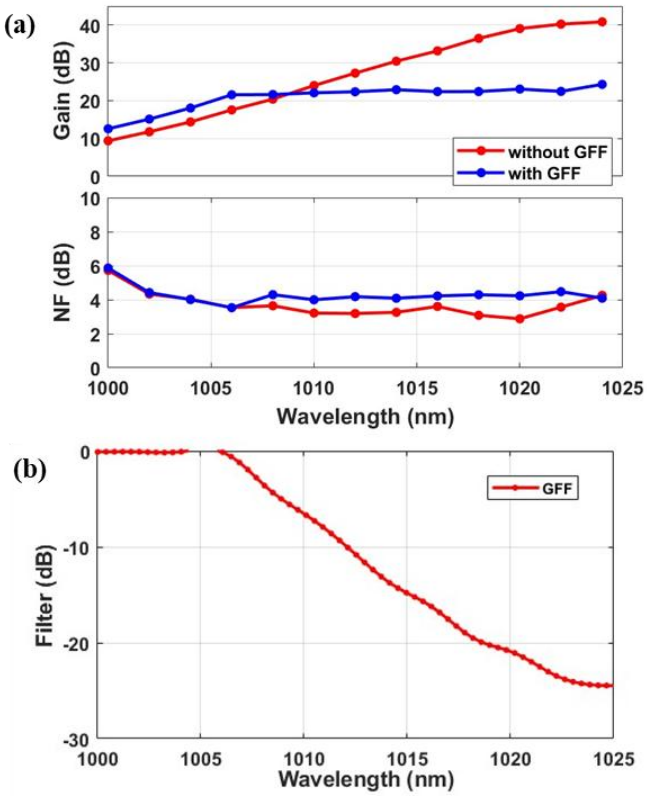

Figure 7.10: (a) Gain and NF spectra of partial double-pass YDFA with and without GFF; (b) filter spectrum of the GFF.

7.3.1.3 Three-stage YDFA

To enhance PCE in the S-band EDFA, another conventional approach involves using a multistage configuration with GFF inserted between each amplifier stage. In my research, I conducted a preliminary investigation into the amplification characteristics of an S-band type YDFA using this approach.

Figure 7.11 illustrates the configuration of the gain-flattened S-band type YDFA, which consists of three amplifier stages. In this setup, 13 WDM channels with a total input power of -18.9 dBm (-20 dBm per channel) are launched into the YDF. Each amplifier stage employs a 915 nm forward pumping scheme. The YDF lengths for the three stages are 0.8 m, 0.2 m, and 0.2 m, respectively, with corresponding pump powers of 1000 mW, 200 mW, and 200 mW. To suppress ASE and flatten the gain spectrum, GFF1 and GFF2 are placed between each amplifier stage. The IL from the WDM coupler, isolator, and GFFs were considered ideal at 0 dB, ensuring that the amplifier's performance is not compromised by these components. This configuration is designed to optimize the PCE while maintaining a flattened gain profile between 1000 and 1025nm.

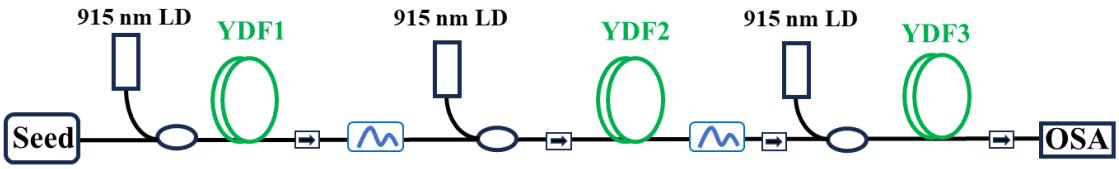

Figure 7.11: Configuration of the gain-flattened S-band type YDFA with three amplifier stages

Figure 7.12(a) shows the gain and NF spectra of 3-stage S-band type YDFA with and without GFF. In the absence of GFFs (red line of top figure), the amplifier achieves a gain exceeding 20 dB across the 1002 nm to 1024 nm range, but with a significant 10 dB variation. To address this issue, two optimized GFFs were inserted between the amplifier stages. As shown in blue line of top figure, this modification successfully flattens the gain to an average of 20 dB, with less than 1 dB of variation across the entire wavelength range. The NF also remains low, staying below 3.5 dB, with only a slight degradation of 0.3 dB due to the insertion of the GFFs. Figure 7.12(b) illustrates the filter spectra of the GFFs used in each stage. To effectively suppress ASE generated at wavelengths longer than 1025 nm, the GFFs were designed to operate within the 1000-1030 nm range. GFF1 exhibits a peak attenuation of -12 dB at 1013 nm, while GFF2 peaks at 1020 nm. Compared to the gain-flattened partial double-pass YDFA, the three-stage YDFA demonstrates smaller NF degradation after the insertion of GFFs. This improvement is due to the distribution of strong attenuation across two GFFs in the three-stage configuration, as opposed to the partial double-pass YDFA, which relies on a single GFF. By spreading the attenuation across multiple stages, the three-stage YDFA maintains lower NF levels, enhancing overall performance. However, it is important to consider that in real-world applications, the three-stage amplifier introduces additional passive fibre components, which can result in increased IL.

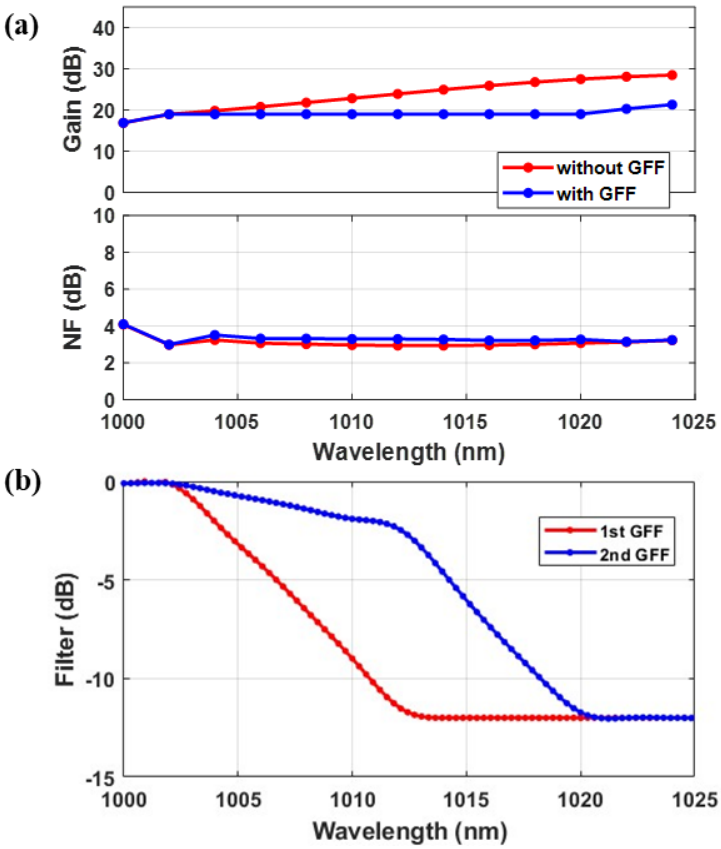

Figure 7.12: (a) Gain and NF spectra of 3-stage S-band YDFA with and without GFF; (b) Filter spectrum of the GFFs at each stage.

7.3.2 Long Wavelength Extension (Extended L-band type YDFA)

To fully explore the potential of the 1 µm optical communication window, it is crucial to extend the YDFA gain towards 1110 nm and beyond. However, expanding the gain region to longer wavelengths presents significant challenges. The PCE of an extended L-band YDFA is inherently lower than that of a conventional C-band YDFA because the L-band operates at the tail end of the ytterbium gain band, where the emission cross-sections are much smaller than near the 1030 nm peak. As a result, achieving sufficient gain requires a longer fibre length, which leads to higher background loss.

Moreover, due to the reduced PCE beyond 1110 nm, higher pump power is generally needed to enhance amplifier performance. This requirement is often constrained by the limitations of conventional single-mode laser diodes. In the case of extended L-band EDFAs, various amplification configurations have been explored to improve PCE, including in-band pumping with longer pump wavelengths (e.g., 1480 nm or 1540 nm), the use of multimode cladding pumping schemes, and the implementation of bi-directional pump configurations [141, 145].

In this subsection, I have designed a hybrid bi-directional pumped YDFA capable of operating beyond 1104 nm, extending its gain up to 1140 nm. The emission and absorption cross-sections data used in my simulations were sourced from Thorlabs [30], which provides a preliminary prediction of the operating wavelength range for extended L-band YDFAs. According to these data, 1140 nm represents the current upper limit for wavelength extension. However, further exploration of even longer wavelengths could be achieved through the development of novel YDFs specifically designed for communication applications.

7.3.2.1 Extended L-band type YDFA design

Figure 7.13 illustrates the high-power, low-noise extended L-band type YDFA designed with a hybrid bi-directional pumping scheme. As discussed in Section 6.2, the multimode cladding pumping scheme is particularly effective for L-band amplification, offering higher brightness in the cladding and thus improving PCE at longer wavelengths. While cladding-pumped double-clad YDF enhances gain, it also tends to degrade the NF. To mitigate this NF degradation, my design incorporates a section of single-clad YDF (SC-YDF) in the first stage, which is forward-pumped by a 980 nm single-mode laser diode. In the second stage, which uses DC-YDF, three different pumping schemes were explored: forward, backward, and bi-directional. The pump powers and fibre lengths used for each stage are detailed in Table 4, with the first stage using a 4 m length of fibre and the second stage using a 400 m length. 13 WDM channels were used as the seed source with -8.9 dBm total power (-20 dBm/ch). The amplifier was seeded with 19 WDM channels operating in 1102-1140 nm, with a total input power of -7.2 dBm (-20 dBm per channel). To ensure a fair comparison of the three pumping schemes, the total input power was kept consistent across all configurations. The input power for the first stage was set at 0.4 W, while the total pump power for the second stage was maintained at 4 W.

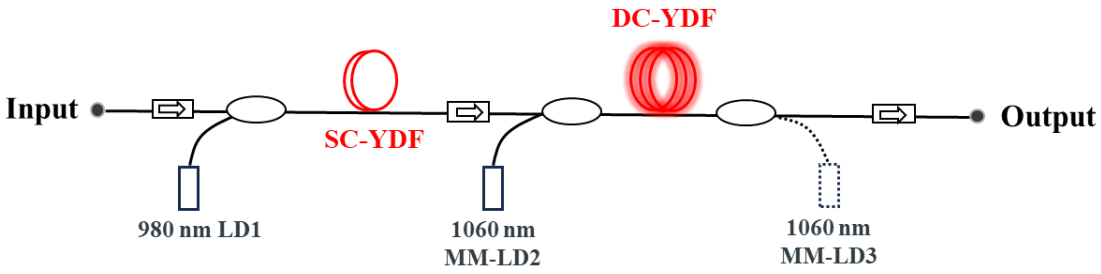

Figure 7.13: Extended L-band type YDFA configuration.

Table 4 Parameters of pump power and fibre lengths used in extended L-band type YDFA.

	Pump scheme	Forward power	Backward power	Fibre length
1st stage	Forward pump	0.4 W	-	4 m SC-YDF
2nd stage	Forward pump	4 W	-	400 m DC-YDF
	Backward pump	-	4 W	
	Bi-directional pump	2 W	2 W	

7.3.2.2 Simulation results and discussion

Before evaluating the performance of the dual-stage YDFA, I conducted simulations to analyse the gain and NF spectra of a single-stage cladding-pumped YDFA operating in the 1104-1140 nm range, using various pump wavelengths. Considering commercially available multimode laser diodes at 1 μm, the pump wavelengths selected for simulation were 915 nm, 975 nm, 1064 nm, and 1080 nm, each with a pump power of 4 W. Figure 7.14 presents the calculated gain and NF spectra for these pump wavelengths. The gain spectrum (top) shows a clear dependence on the pump wavelength, with the highest gain achieved using a 1080 nm pump (black line), reaching a peak of approximately 30 dB. The 1064 nm pump also provides substantial gain (green line), though slightly lower than that of the 1080 nm pump. In contrast, the 975 nm and 915 nm pumps yield considerably lower gain across the wavelength range (red and blue line). Regarding the NF (bottom figure), the results indicate that both the 915 nm, 975 nm pumps (red and blue line) exhibit a high NF at shorter wavelengths but maintain a relatively low NF at longer wavelengths, stabilizing below 4 dB across most of the spectrum. The 1064 nm (green line) pump follows closely, with an NF of around 5 dB. However, the 1080 nm pump (black line), while delivering the highest gain, results in a higher NF, consistently around 6 dB. This increase in NF is due to the reduced difference between the signal and pump wavelengths, which can lead to performance degradation [146]. Considering both gain and NF, the 1064 nm pump emerges as a potentially more suitable choice for amplifying YDFA in the 1104-1140 nm range, offering a balanced performance with moderate gain and lower NF. Notably, when using the 1064 nm pump, a 10-dB bandwidth of 36 nm was achieved within the 1104-1140 nm range, making it an effective option for extended long-wavelength applications.

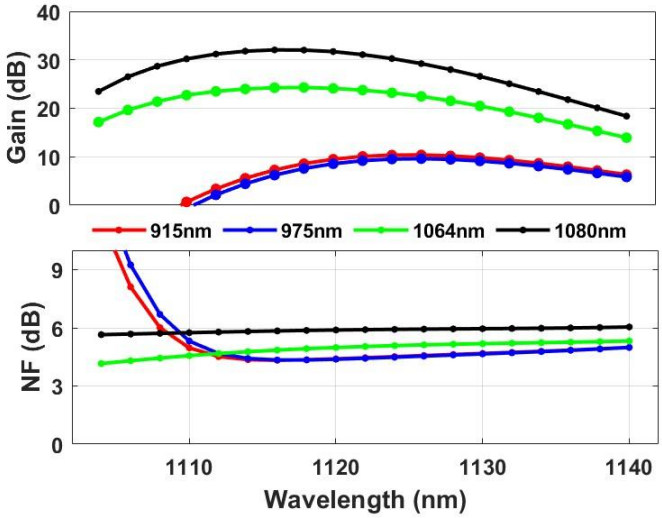

Figure 7.14: Calculated gain and NF spectra of single-stage YDFA versus different pump wavelength.

Building on these findings, I employed a 1064 nm MM-LD with a pump power of 4 W to drive the second stage DC-YDF in a dual-stage YDFA configuration. For the first stage SC-YDF, which utilizes SC-YDF, a 980 nm single-mode laser diode at 400 mW was used to optimize the NF. Figure 7.15 presents the calculated gain and NF spectra for a dual-stage YDFA operating in the 1104-1140 nm range, comparing three different pump schemes for the second stage: forward, backward, and bi-directional. Among these schemes, the bi-directional pumping scheme (green line) demonstrates the highest overall gain, reaching up to approximately 48 dB at 1104 nm and maintaining superior gain performance across the entire wavelength range. The backward pumping scheme (blue line) follows, providing slightly lower gain but still outperforming the forward pumping scheme. In terms of NF, the bi-directional scheme also achieves the best results, consistently remaining below 6 dB across the wavelength range. The forward pumping scheme maintains a slightly higher NF, just above 6 dB, but remains relatively stable. In contrast, the backward pumping scheme, while delivering reasonable gain, results in a significantly higher NF, increasing to around 10 dB as the wavelength approaches 1140 nm.

Overall, the bi-directional pumping scheme offers the best performance in both gain and NF, making it the most effective configuration for extending gain while maintaining low noise in the extended L-band type YDFA. It is worth noting that throughout this thesis, I utilized parameters from IXblue (IXF-6-126 µm) YDF, which has an absorption coefficient of 273.3 dB/m at 977 nm. However, higher doping concentrations are available in other YDFs, such as the YB1200-4/125, which has an absorption coefficient of approximately 826 dB/m at 977 nm. These higher doping concentrations could potentially reduce the required active fibre length for extended L-band YDFAs

by at least threefold, down to approximately 130 m, offering further opportunities for optimization in amplifier design.

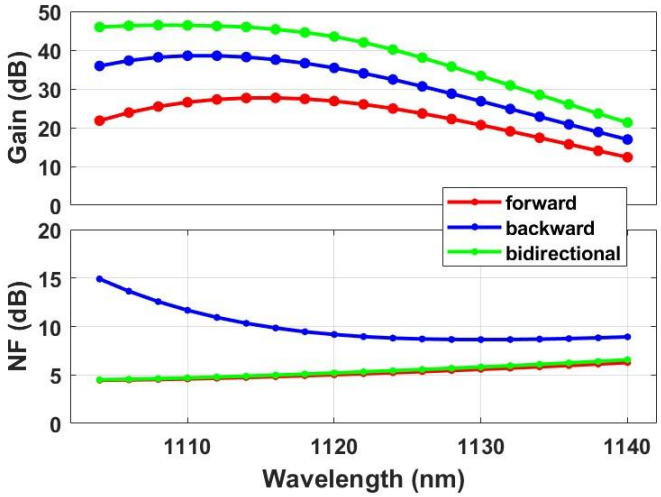

Figure 7.15: Gain and NF spectra of dual-stage YDFA versus different pump schemes at 2nd stage: forward, backward, and bi-directional.

7.4 Conclusions

In this chapter, I systematically explored the wideband YDFA operating at the 1 µm wavelength, with a focus on its application as a high-performance amplifier in future telecommunication networks using hollow-core fibre. I first introduced an ultra-wideband YDFA that combines two YDFAs operating in different windows (1025-1072 nm and 1075-1110 nm) in a parallel configuration, similar to the C+L band EDFAs. For the 1025-1072nm YDFA, a dual stage configuration was utilized, incorporating a dielectric thin-film-based gain flattening filter (GFF) as an interstage component. For the 1075-1110 nm YDFA, a relatively lengthy gain fibre (60 m) was employed, coupled with a hybrid pumped dual-stage configuration to ensure high gain and a low NF. By combining these two amplifiers, I achieved a wideband YDFA spanning the wavelength range 1025-1110 nm (~21.9 THz), nearly 5 times the bandwidth of a C-band EDFA. This amplifier shows great advantages in utilizing a much simpler amplification scheme for >20-THz bandwidth whilst providing excellent gain and NF performance compared to recent works which exploited multiple bands in conjunction with the use of various amplification technologies for data transmission.

Further exploration into extending the YDFA's gain bandwidth to both shorter and longer wavelengths was conducted through simulations. The short-wavelength extension was investigated with different YDFA configurations, including single double-pass, partial double-pass, and three-stage designs. The three-stage configurations showed promising results in achieving a wider

bandwidth of ~6.4 THz with improved gain and NF performance in the 1002-1024 nm range, indicating potential for significant enhancements in short wavelength applications. For long-wavelength extensions, the chapter detailed the design of a hybrid bi-directional pumped YDFA, aiming to extend the gain beyond 1110 nm. Simulation results demonstrated the feasibility of achieving high gain and low NF in the extended L-band type YDFA (1104-1140 nm). The current design of this extended L-band type YDFA requires a fibre length of approximately 400 m. However, higher doping concentrations in YDFs could optimize the amplifier design by significantly reducing the required active fibre length.

To the best of our knowledge, this is the first time the YDFA has been systematically evaluated for 1 μm optical fibre communications. With the transmission loss of HCF getting lower and the increasing availability of 1 μm components, this advancement should support significantly enhanced data transmission in the 1 μm waveband and represents a promising approach to meet the growing demands for high-capacity data transmission. Future work should focus on experimental validation of the simulated results and exploration of novel fibre designs to further enhance the performance of YDFAs for telecommunication applications.

Chapter 8 Conclusion and Future Work

8.1 Summary of the thesis

In Chapter 3, I explored various technologies for GFFs, focusing on LPFGs, dielectric thin-film filters, and programmable waveshapers. LPFGs were investigated as low-loss, all-fibre spectral filters for multi-stage amplifiers and functional devices. Both conventional and phase-shifted LPFGs could effectively flatten and broaden gain bandwidth in amplifiers. A key achievement was the successful fabrication of LPFGs using a 3D printing technique, which produced clear resonance peaks with over 10 dB filter strength at 1.5 µm. Additionally, the arc-induced periodic taper technique was explored, achieving more than 20 dB attenuation at resonant dip for around 1 µm.

The chapter also highlighted the potential of FMF based LPFGs as low-loss broadband mode scramblers. Simulations predicted a >260 nm bandwidth with a short 0.613-cm LPFG, while experiments confirmed a 100 nm bandwidth over the C band with minimal insertion and mode-dependent losses. Finally, the investigation of dielectric thin-film filters and programmable waveshapers based LCoS technologies demonstrated their effectiveness as GFFs and multi-channel comb filters in wideband YDFAs.

In Chapter 4, I focused on the design and analysis of multi-stage EDFAs aimed at extending the gain bandwidth beyond the traditional C-band. The research demonstrated that optimized GFFs could significantly enhance the gain bandwidth while achieving a flatten gain profile. Simulations and experiments confirmed a reduction in gain variation to as low as 0.5 dB. The trade-off between gain flattening and NF was carefully examined, revealing that even though stronger GFFs can improve bandwidth, they introduce higher attenuation, thus increasing NF. The findings from this chapter provided crucial insights that informed the subsequent work on broadband YDFAs

Chapter 5 presented a comprehensive study of wideband YDFAs in both single-stage (SS-YDFA) and dual-stage (DS-YDFA) configurations, aimed at developing high-performance amplifiers for future telecommunication networks utilizing hollow-core fibres operating around 1 µm.

Simulations of a SS-YDFA with a 9 m YDF length demonstrated a flat gain spectrum over an 87 nm bandwidth (1023-1110 nm) with a gain of >10 dB. For the DS-YDFA simulations without a GFF showed optimal performance with fibre lengths of 3 m and 9 m for the first and second stages, respectively, providing a bandwidth of 72 nm (1025-1097 nm) with a gain >17 dB. Experimental validation, although limited by the available seed source range of 1020-1080 nm, confirmed these simulated trends. The SS-YDFA with a 12 m YDF exhibited a flat emission spectrum with a 3 dB

bandwidth of 40 nm (1040-1080 nm), while the DS-YDFA exhibited superior performance with a flatter gain profile and consistent NF across the measured wavelength range.

A significant achievement was the successful demonstration of a penalty-free transmission system in the 1 µm band using the fabricated broadband DS-YDFA. Both 90-Gb/s Nyquist PAM4 and >100-Gb/s adaptively-loaded DMT transmission were achieved over a bandwidth of 16.3 THz (1020-1080 nm) after transmission in a NANF. The incorporation of a GFF between amplifier stages in the DS-YDFA further improved performance, theoretically achieving a gain bandwidth of 65 nm (~17.4 THz) from 1025 nm to 1090 nm with a 21.7 dB average flat gain (<1 dB variation). Experimental results using a 1 µm waveshaper as a programmable GFF demonstrated a 50 nm gain bandwidth (1025-1075 nm) with an average gain of 20 dB and <1 dB gain flatness.

This chapter showcased the potential of YDFAs for 1 µm spectral region data transmission. The achieved 50 nm optical bandwidth (~13.7 THz) is almost 3.1 times greater than that of C-band EDFAs, highlighting the promising future of data transmission in the 1 µm spectral region.

Chapter 6 focused on the characterization and optimization of cladding-pumped YDFAs for long-wavelength operation. The research compared various configurations, including core-pumped and cladding-pumped schemes, evaluating their gain, NF, and PCE.

Key findings revealed that cladding-pumped YDFAs exhibit more stable and higher gain over a broader wavelength range compared to core-pumped YDFAs, particularly at longer wavelengths. While core-pumped YDFAs showed lower NF, cladding-pumped YDFAs demonstrated superior PCE across all input power levels, reaching 50% at an input power of 8.08 dBm, with a saturated output power of 33 dBm. Simulations for single-channel cladding-pumped YDFAs using 915 nm pump diodes showed that increasing fibre length shifts the gain peak towards longer wavelengths. A 60-m YDFA achieved a 43-nm-wide bandwidth (1072-1115 nm) with over 25 dB gain. Experimental results largely corroborated these simulations, with ASE spectra showing 10 dB bandwidths of 37 nm, 35 nm, and 33 nm for YDF lengths of 20 m, 40 m, and 60 m, respectively.

A significant achievement was the demonstration of a wide gain bandwidth from 1070 to 1110 nm with gain exceeding 25 dB and NF below 6.5 dB, using a commercially available 915 nm MM pump LD. This bandwidth (~10.1 THz) is nearly 2.3 times as wide as that of EDFAs operating in the C-band.

To further enhance performance, a hybrid dual-stage pumping configuration was introduced. Both simulations and experimental results consistently showed that this hybrid core-plus-cladding pump scheme offers significant advantages over the simple cladding-pumped configuration, achieving a broader bandwidth and lower NF across the spectrum. Notably, the hybrid setup improved the NF by 1.1 dB, resulting in an NF of 4.3 dB.

This final research chapter (Chapter 7) presented a comprehensive exploration of ultra-wideband YDFAs operating at the 1 μm wavelength, with a focus on their application in future telecommunication networks using hollow-core fibre. The research culminated in the development of an innovative ultra-wideband YDFA that combines two YDFAs operating in different windows (1025-1072 nm and 1075-1110 nm) in a parallel configuration.

A key achievement was the realization of a wideband YDFA spanning the wavelength range 1025-1110 nm (~21.9 THz), nearly 5 times the bandwidth of a C-band EDFA. This amplifier demonstrated significant advantages in utilizing a simpler amplification scheme for >20-THz bandwidth while providing excellent gain and NF performance compared to recent works exploiting multiple bands and various amplification technologies.

The chapter also explored potential extensions of the YDFA's gain bandwidth to both shorter and longer wavelengths through simulations. For short-wavelength extension, various configurations were investigated, with three-stage designs showing promising results in achieving a wider bandwidth of ~6.4 THz with improved gain and NF performance in the 1002-1024 nm range.

Long-wavelength extensions were addressed through the design of a hybrid bi-directional pumped YDFA. Simulation results demonstrated the feasibility of achieving high gain and low NF in the extended L-band type YDFA (1104-1140 nm), although current designs require a relatively long fibre length of approximately 400 m.

This research represents the first systematic evaluation of wideband YDFAs for 1 μm optical fibre communications. As transmission losses in hollow-core fibres continue to decrease and more 1 μm components become available, the advancements presented here have the potential to support significantly enhanced data transmission in the 1 μm waveband, offering a promising approach to meet the growing demands for high-capacity data transmission.

8.2 Future work

While this thesis has made significant contributions to the field of optical amplification, particularly in gain flattening techniques, bandwidth extension, and performance optimization, there remain numerous avenues for further research. The continued evolution of telecommunication networks demands amplifiers that can handle higher data rates, broader bandwidths, and operate efficiently over longer distances. Here I outline several promising directions for future work, drawing upon the findings of each chapter.

8.2.1 Advanced LPFG technologies

The work on LPFGs demonstrated their potential for gain flattening in both single-mode and few-mode fibre systems. Future work could focus on further optimizing LPFG fabrication techniques to enhance spectral filtering capabilities. Since 3D printing and arc-induced techniques have proved effective and precise abilities to fabricate conventional SMF-LPFG, further investigation should fabricate precise GFFs for EDFA and YDFA. Especially, there is no reports about the 1 μm LPFGs designed for the GFF of wideband YDFA or BDFA operating in 1.3 μm.

Furthermore, with the SDM becoming the hottest topic in telecommunication area, multi-core LPFGs should arise attention. Although there have been a few research on the multicore LPFGs [147-149], however, due to the different locations of the cores inside the multicore fibre, it difficult to fabricate identical gratings on each core and achieve the same filtering performance. Figure 7.15 shows an example to induce LPFGs in a MCF by plating an uncoated MCF on a 3D printed grooved plate and rotate the fibre. Figure 8.1(B) shows the pressure-induced LPG transmission spectra in each MCF core, for different angular position. It indicates that different core has different grating performance under different angular position. More precise fabrication techniques should be explored to systematically inscribe multicore LPFGs for future SDM based optical communication systems.

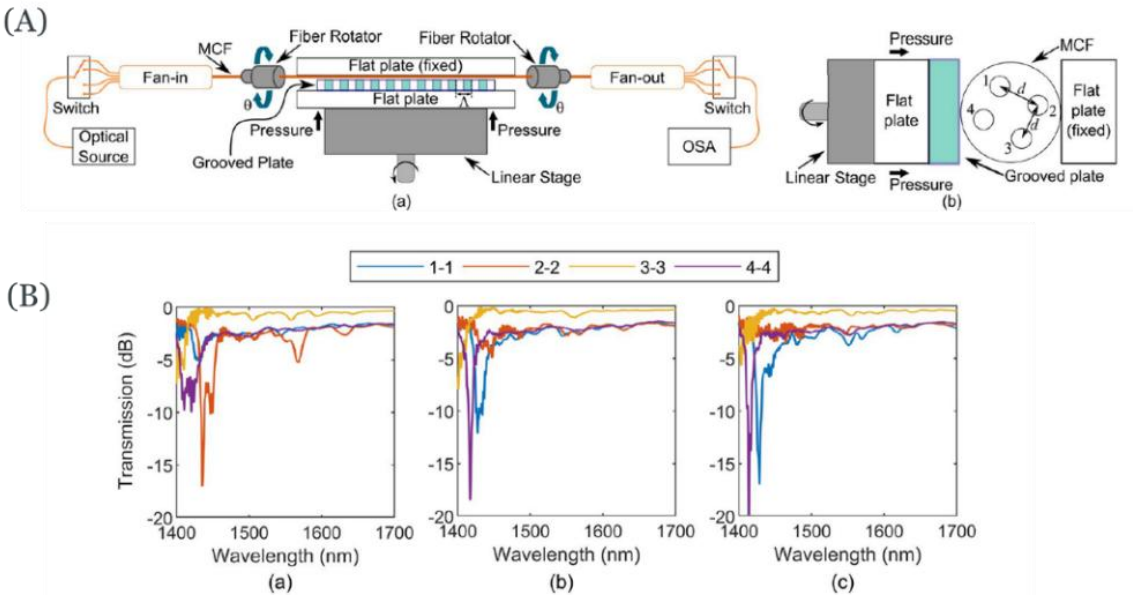

Figure 8.1: (A) Diagram of the experimental setup to pressure-induce LPFGs in a MCF; (B) Pressure-induced LPG transmission spectra in each MCF core, for the angular position of (a) 40°, (b) 60° and (c) 80° [147].

8.2.2 Further development of wideband YDFA for telecommunication

The development of wideband YDFAs in the 1 µm region has unlocked a promising new spectral window for optical communication. However, there remains considerable scope for further improvements to maximize the potential of these amplifiers.

One key limitation encountered in this work is the lack of an appropriate wideband seed source that can fully cover the operational wavelength range of the YDFA. Future research should prioritize the development of multi-channel seed sources, capable of spanning this entire wavelength range, to enhance performance and enable more efficient amplification across broader spectral bands. In addition, the advancement of multi-mode pump diodes, particularly those operating at longer wavelengths (e.g., 1030 nm), will play a critical role in improving the performance of cladding-pumped YDFAs. These longer-wavelength pump sources would allow for more efficient pumping and broaden the gain spectrum, which is crucial for amplifiers aiming to cover wider wavelength regions.

Regarding the ultra-wideband YDFA developed in this thesis, which achieved an impressive bandwidth of 21.9 THz, future work should collaborate with the telecommunication group to integrate this device into HCF transmission systems.

- Expanding the operational wavelength range of YDFAs remains a critical area for future research. While our simulations have indicated the feasibility of extending gain bandwidth

both below 1025 nm and beyond 1110 nm, experimental validation is essential. Building prototypes that push the operational boundaries and testing them in transmission systems will be essential to realize the full potential of YDFAs for broader wavelength applications.

Furthermore, there is a gap between the longest wavelength explored in this thesis (1140 nm) and the emission capabilities of currently studied BDFA, which operates around 1255 nm [150]. Bridging this gap is crucial for achieving a continuous, broad-spectrum amplification. Future research should focus on investigating novel active fibres capable of extending the gain spectrum to cover this intermediate range. One promising avenue is the development of Bi-doped aluminosilicate fibres, which exhibit emission peaks around 1160 nm when pumped at 1120 nm [151]. These fibres could play a vital role in filling the spectral gap and expanding the available amplification window for future optical systems. Additionally, the YDF used in this research, while effective, were not specifically optimized for telecommunication applications due to their relatively large core diameter and small numerical aperture. Future research should focus on designing and fabricating novel YDFs tailored explicitly for telecommunication needs, e.g., small-core and high-NA fibre design (NA≥ 0.3) is beneficial for maintaining a high power conversion efficiency and deep gain saturation in low-power amplifier operation systems [133]. The design and glass host of these fibres should aim to balance low nonlinearity, high efficiency, and excellent beam quality to meet the stringent requirements of next-generation optical networks.

Appendix A List of Publications

Journal Publications

1. Xin Huang, Sijing Liang, Lin Xu, David J. Richardson, and Yongmin Jung. "Wideband (13.7 THz) Gain-Flattened Yb-Doped Fiber Amplifier for Telecommunication Applications." IEEE Photonics Technology Letters (2024).

2. Xin Huang, Yongmin Jung, Yaping Liu, Kerrianne Harrington, and David J. Richardson. "Broadband mode scramblers for few-mode fibers based on 3D printed mechanically induced long-period fiber gratings." IEEE Photonics Technology Letters 34, no. 3 (2022): 169-172.

3. Xin Huang, Sijing Liang, Lin Xu, David J. Richardson, and Yongmin Jung. “Ultrawide YDFA with 21.9 THz’s bandwidth for 1 μm telecommunication” (to be submitted).

Conference Publications

1. Xin Huang, Yongmin Jung, Sijing Liang, and David J. Richardson. "Gain flattened wideband YDFA for 1 μm data transmission." In CLEO: Science and Innovations, pp. SM2I-1. Optica Publishing Group, 2023.

2. Hong, Yang, Xin Huang, Yongmin Jung, Hans Christian H. Mulvad, Hesham Sakr, Natsupa Taengnoi, Kyle RH Bottrill, Francesco Poletti, Periklis Petropoulos, and David J. Richardson. "Wideband Transmission in the 1-μm Band based on a Hollow-core Fiber and Wideband YDFA." In Optical Fiber Communication Conference, pp. W4D-5. Optica Publishing Group, 2023.

3. Xin Huang, Sijing Liang, Lin Xu, David J. Richardson, and Yongmin Jung. "Cladding-pumped YDFA for data transmission in the 1071-1097 nm range." In 49th European Conference on Optical Communications (ECOC 2023), vol. 2023, pp. 839-842. IET, 2023.

4. Xin Huang, Sijing Liang, Lin Xu, David J. Richardson, and Yongmin Jung. "21.9 THz-wide Ytterbium Doped Fiber Amplifier for 1 μm Data Transmission." In Optical Fiber Communication Conference, pp. W1D-7. Optica Publishing Group, 2024.

List of References

[1] M. J. Digonnet, "Optical and electronic properties of rare earth ions in glasses," in *Rare-Earth-Doped Fiber Lasers and Amplifiers*(Marcel Dekker, 2001), pp. 17-112.

[2] P. C. Becker, N. A. Olsson, and J. R. Simpson, *Erbium-doped fiber amplifiers : fundamentals and technology* (Academic Press, 1999), ISBN: 978-0-12-084590-3.

[3] R. J. Mears, L. Reekie, I. Jauncey, and D. N. Payne, "Low-noise erbium-doped fibre amplifier operating at 1.54 μm," Electronics Letters **19**, 1026-1028 (1987).

[4] N. Edagawa, K. Mochizuki, and H. Wakabayashi, "1.2 Gbit/s, 218 km transmission experiment using inline Er-doped optical fibre amplifier," Electronics Letters **5**, 363-365 (1989).

[5] S. V. Firstov, K. E. Riumkin, A. M. Khegai, S. V. Alyshev, M. A. Melkumov, V. F. Khopin, F. V. Afanasiev, A. N. Guryanov, and E. M. Dianov, "Wideband bismuth- and erbium-codoped optical fiber amplifier for C + L + U-telecommunication band," Laser Physics Letters **14**, 110001 (2017).

[6] D. J. Richardson, "Filling the light pipe," Science **330**, 327-328 (2010).

[7] C. E. Shannon, "A mathematical theory of communication," The Bell system technical journal **27**, 379-423 (1948).

[8] P. J. Winzer, D. T. Neilson, and A. R. Chraplyvy, "Fiber-optic transmission and networking: the previous 20 and the next 20 years," Optics Express **26**, 24190-24239 (2018).

[9] D. J. Richardson, J. M. Fini, and L. E. Nelson, "Space-division multiplexing in optical fibres," Nature photonics **7**, 354-362 (2013).

[10] T. Mizuno, H. Takara, K. Shibahara, A. Sano, and Y. Miyamoto, "Dense space division multiplexed transmission over multicore and multimode fiber for long-haul transport systems," Journal of Lightwave Technology **34**, 1484-1493 (2016).

[11] Y. Jung, S.-u. Alam, D. J. Richardson, S. Ramachandran, and K. S. Abedin, "Multicore and multimode optical amplifiers for space division multiplexing," in *Optical Fiber Telecommunications VII*(Elsevier, 2020), pp. 301-333.

[12] L. Rapp, and M. Eiselt, "Optical Amplifiers for Wideband Optical Transmission Systems," in *2021 Optical Fiber Communications Conference and Exhibition (OFC)*(2021), pp. 1-3.

[13] S. Liang, S. Jain, L. Xu, K. R. Bottrill, N. Taengnoi, M. Guasoni, P. Zhang, M. Xiao, Q. Kang, and Y. Jung, "High gain, low noise, spectral-gain-controlled, broadband lumped fiber Raman amplifier," Journal of Lightwave Technology **39**, 1458-1463 (2021).

[14] S. Singh, and R. Kaler, "Flat-gain L-band Raman-EDFA hybrid optical amplifier for dense wavelength division multiplexed system," IEEE Photonics Technology Letters **25**, 250-252 (2012).

[15] H. Kanamori, H. Yokota, G. Tanaka, M. Watanabe, Y. Ishiguro, I. Yoshida, T. Kakii, S. Itoh, Y. Asano, and S. Tanaka, "Transmission characteristics and reliability of pure-silica-core single-mode fibers," Journal of Lightwave Technology **4**, 1144-1150 (1986).

[16] F. Poletti, "Nested antiresonant nodeless hollow core fiber," Optics Express **22**, 23807-23828 (2014).

[17] H. Sakr, T. D. Bradley, G. T. Jasion, E. N. Fokoua, S. R. Sandoghchi, I. A. Davidson, A. Taranta, G. Guerra, W. Shere, Y. Chen, J. R. Hayes, D. J. Richardson, and F. Poletti, "Hollow Core NANFs with

Five Nested Tubes and Record Low Loss at 850, 1060, 1300 and 1625nm," in *Optical Fiber Communication Conference (OFC) 2021*, P. K. J. X. C. C. R. C. C. Dong, and M. Li, eds. (Optica Publishing Group, Washington, DC, 2021), p. F3A.4.

[18] H. C. H. Mulvad, S. Abokhamis Mousavi, V. Zuba, L. Xu, H. Sakr, T. D. Bradley, J. R. Hayes, G. T. Jasion, E. Numkam Fokoua, A. Taranta, S. U. Alam, D. J. Richardson, and F. Poletti, "Kilowatt-average-power single-mode laser light transmission over kilometre-scale hollow-core fibre," Nature photonics **16**, 448-453 (2022).

[19] H. Sakr, Y. Chen, G. T. Jasion, T. D. Bradley, J. R. Hayes, H. C. H. Mulvad, I. A. Davidson, E. Numkam Fokoua, and F. Poletti, "Hollow core optical fibres with comparable attenuation to silica fibres between 600 and 1100 nm," Nature Communications **11**, 6030 (2020).

[20] F. Poletti, N. V. Wheeler, M. N. Petrovich, N. Baddela, E. Numkam Fokoua, J. R. Hayes, D. R. Gray, Z. Li, R. Slavík, and D. J. Richardson, "Towards high-capacity fibre-optic communications at the speed of light in vacuum," Nature photonics **7**, 279-284 (2013).

[21] H. Sakr, T. D. Bradley, Y. Hong, G. T. Jasion, J. R. Hayes, H. Kim, I. A. Davidson, E. N. Fokoua, Y. Chen, and K. R. Bottrill, "Ultrawide bandwidth hollow core fiber for interband short reach data transmission," in *Optical Fiber Communication Conference*(Optica Publishing Group2019), p. Th4A. 1.

[22] A. Nespola, S. Straullu, T. D. Bradley, K. Harrington, H. Sakr, G. T. Jasion, E. N. Fokoua, Y. Jung, Y. Chen, J. R. Hayes, F. Forghieri, D. J. Richardson, F. Poletti, G. Bosco, and P. Poggiolini, "Transmission of 61 C-Band Channels Over Record Distance of Hollow-Core-Fiber With L-Band Interferers," Journal of Lightwave Technology **39**, 813-820 (2021).

[23] A. Nespola, S. Straullu, T. D. Bradley, H. C. Mulvad, J. R. Hayes, G. T. Jasion, M. A. Gouveia, S. R. Sandoghchi, S. Bawn, F. Forghieri, D. J. Richardson, F. Poletti, and P. Poggiolini, "Record PM-16QAM and PM-QPSK transmission distance (125 and 340 km) over hollow-core-fiber," in *45th European Conference on Optical Communication (ECOC 2019)*(2019), pp. 1-4.

[24] R. Paschotta, J. Nilsson, A. C. Tropper, and D. C. Hanna, "Ytterbium-doped fiber amplifiers," Journal of quantum electronics **33**, 1049-1056 (1997).

[25] Y. e. Jeong, J. Sahu, D. a. Payne, and J. Nilsson, "Ytterbium-doped large-core fiber laser with 1.36 kW continuous-wave output power," Optics Express **12**, 6088-6092 (2004).

[26] J. Limpert, F. Roser, T. Schreiber, and A. Tunnermann, "High-power ultrafast fiber laser systems," Journal of selected topics in Quantum Electronics **12**, 233-244 (2006).

[27] A. Einstein, "Strahlungs-emission und -absorption nach der Quantentheorie," Verhandlungen der Deutschen Physikalischen Gesellschaft (in German) **18**, 318–323 (1916).

[28] E. Desurvire, and M. N. Zervas, "Erbium‐doped fiber amplifiers: principles and applications," (American Institute of Physics, 1995).

[29] W. Koechner, *Solid-state laser engineering* (Springer, 2013), ISBN: 366215143X.

[30] "https://www.thorlabs.com/."

[31] J. L. Zyskind, J. A. Nagel, and H. D. Kidorf, "Chapter 2 - Erbium-Doped Fiber Amplifiers for Optical Communications," in *Optical Fiber Telecommunications IIIB (Third Edition)*, I. P. Kaminow, and T. L. Koch, eds. (Academic Press, 1997), pp. 13-68.

[32] E. Desurvire, J. R. Simpson, and P. C. Becker, "High-gain erbium-doped traveling-wave fiber amplifier," Optics Letters **12**, 888-890 (1987).

[33] M. J. Digonnet, *Rare-earth-doped fiber lasers and amplifiers, revised and expanded* (CRC press, 2001), ISBN: 0429207662.

[34] A. Brenier, and G. Boulon, "Overview of the best Yb3+-doped laser crystals," Journal of alloys and compounds **323**, 210-213 (2001).

[35] G. Boulon, "Why so deep research on Yb3+-doped optical inorganic materials?," Journal of alloys and compounds **451**, 1-11 (2008).

[36] A. Kurkov, V. Paramonov, and O. Medvedkov, "Ytterbium fiber laser emitting at 1160 nm," Laser Physics Letters **3**, 503 (2006).

[37] H. Fritsche, O. Lux, C. Schuett, S. W. Heinemann, M. Dziedzina, W. Gries, and H. J. Eichler, "Increased efficiency of Er: YAG lasers at 1645 nm using narrow bandwidth diode lasers and dual-wavelength resonant pumping," in *Solid State Lasers XXIII: Technology and Devices*(SPIE2014), pp. 35-43.

[38] B. J. Ainslie, "A Review of the Fabrication and Properties of Erbium-Doped Fibers for Optical Amplifiers," Journal of Lightwave Technology **9**, 220-227 (1991).

[39] S. Tanabe, "Rare-earth-doped glasses for fiber amplifiers in broadband telecommunication," Comptes Rendus Chimie **5**, 815-824 (2002).

[40] A. Jha, P. Joshi, S. Shen, and L. Huang, "Spectroscopic characterization of signal gain and pump ESA in short-lengths of RE-doped tellurite fibers," Journal of Non-Crystalline Solids **353**, 1407-1413 (2007).

[41] F. Vetrone, J. C. Boyer, J. A. Capobianco, A. Speghini, and M. Bettinelli, "980 nm excited upconversion in an Er-doped ZnO-TeO2 glass," Applied Physics Letters **80**, 1752-1754 (2002).

[42] F. Wang, C. Shao, C. Yu, S. Wang, L. Zhang, G. Gao, and L. Hu, "Effect of AlPO4 join concentration on optical properties and radiation hardening performance of Yb-doped Al2O3-P2O5-SiO2 glass," Journal of Applied Physics **125**, 173104 (2019).

[43] M. E. Likhachev, M. M. Bubnov, K. V. Zotov, D. S. Lipatov, M. V. Yashkov, and A. N. Guryanov, "Effect of the AlPO4 join on the pump-to-signal conversion efficiency in heavily Er-doped fibers," Optics Letters **34**, 3355-3357 (2009).

[44] J. Campbell, M. A. Cahoon, M. Gachich, M. Norlander, T. Hawkins, J. Ballato, and P. Dragic, "Gain optimization of Er-doped fibers doped with Er:BaF2 nanoparticles," in *2024 Optical Fiber Communications Conference and Exhibition (OFC)*(2024), pp. 1-3.

[45] R. Paschotta, J. Nilsson, P. Barber, J. Caplen, A. C. Tropper, and D. C. Hanna, "Lifetime quenching in Yb-doped fibres," Optics Communications **136**, 375-378 (1997).

[46] M. A. Mel'kumov, I. A. Bufetov, K. S. Kravtsov, A. V. Shubin, and E. M. Dianov, "Lasing parameters of ytterbium-doped fibres doped with P2O5 and Al2O3," Quantum Electronics **34**, 843 (2004).

[47] E. Desurvire, J. L. Zyskind, and C. R. Giles, "Design optimization for efficient erbium-doped fiber amplifiers," Journal of Lightwave Technology **8**, 1730-1741 (1990).

[48] G. Keiser, *Optical fiber communications* (McGraw-Hill New York, 2000), ISBN: 0-07-141204-2.

[49] H. Taga, Y. Yoshida, N. Edagawa, S. Yamamoto, and H. Wakabayashi, "459km, 2.4 Gbit/s 4 wavelength multiplexing optical fiber transmission experiment using 6 Er-doped fiber amplifiers," in *Optical Fiber Communication Conference*(Optica Publishing Group1990), p. PD9.

[50] L. Qian, D. Fortusini, S. Benjamin, G. Qi, P. Kelkar, and V. da Silva, "Gain-flattened, extended L-band (1570–1620 nm), high power, low noise erbium-doped fiber amplifiers," in *Optical Fiber Communication Conference*(Optica Publishing Group2002), p. ThJ4.

[51] Z. Zhai, A. Halder, and J. K. Sahu, "Extending L-band gain to 1628 nm using phospho-alumino-silicate erbium-doped fibre pumped by 1480 nm laser diodes," in *49th European Conference on Optical Communications (ECOC 2023)*(IET2023), pp. 598-600.

[52] R. S. Luís, B. J. Puttnam, G. Rademacher, M. v. d. Hout, G. D. Sciullo, D. Orsuti, C. Okonkwo, C. Antonelli, J. Sakaguchi, and H. Furukawa, "Wideband Unrepeatered Transmission Using Doped Tellurite-Fiber Amplifiers," Journal of Lightwave Technology **42**, 4410-4416 (2024).

[53] A. A. Al-Azzawi, A. A. Almukhtar, P. Reddy, S. Das, A. Dhar, M. C. Paul, H. Arof, H. Ahmad, and S. W. Harun, "An efficient wideband hafnia-bismuth erbium co-doped fiber amplifier with flat-gain over 80 nm wavelength span," Optical fiber technology **48**, 186-193 (2019).

[54] N. K. Thipparapu, A. Umnikov, P. Barua, and J. Sahu, "Bi-doped fiber amplifier with a flat gain of 25 dB operating in the wavelength band 1320–1360 nm," Optics Letters **41**, 1518-1521 (2016).

[55] Z. Zhai, and J. K. Sahu, "High-gain ultra-wideband bismuth-doped fiber amplifier operating in the O+ E+ S band," Optics Letters **49**, 3308-3311 (2024).

[56] Y. Ohishi, T. Kanamori, T. Kitagawa, S. Takahashi, E. Snitzer, and G. H. Sigel Jr, "Pr3+-doped fluoride fiber amplifier operating at 1.31 μ m," Optics Letters **16**, 1747-1749 (1991).

[57] Z. Li, Y. Jung, J. M. Daniel, N. Simakov, P. C. Shardlow, A. M. Heidt, W. A. Clarkson, S.-U. Alam, and D. J. Richardson, "Extreme short wavelength operation (1.65–1.7 μm) of silica-based thulium-doped fiber amplifier," in *Optical Fiber Communication Conference*(Optica Publishing Group2015), p. Tu2C. 1.

[58] S. Aozasa, H. Masuda, H. Ono, T. Sakamoto, T. Kanamori, Y. Ohishi, and M. Shimizu, "1480-1510 nm-band Tm doped fiber amplifier (TDFA) with a high power conversion efficiency of 42%," presented at the OFC 2001. Optical Fiber Communication Conference and Exhibit. Technical Digest Postconference Edition (IEEE Cat. 01CH37171)2001.

[59] Z. Li, A. M. Heidt, J. M. Daniel, Y. Jung, S.-U. Alam, and D. J. Richardson, "Thulium-doped fiber amplifier for optical communications at 2 μm," Optics Express **21**, 9289-9297 (2013).

[60] N. Simakov, Z. Li, S.-U. Alam, P. C. Shardlow, J. M. Daniel, D. Jain, J. Sahu, A. Hemming, W. A. Clarkson, and D. J. Richardson, "Holmium-doped fiber amplifier for optical communications at 2.05–2.13 μm," in *Optical Fiber Communication Conference*(Optica Publishing Group2015), p. Tu2C. 6.

[61] R. E. Tench, W. Walasik, and J.-M. Delavaux, "Novel highly efficient in-band pump wavelengths for medium slope efficiency holmium-doped fiber amplifiers," Journal of Lightwave Technology **39**, 3546-3552 (2021).

[62] Y. Hong, X. Huang, Y. Jung, H. C. H. Mulvad, H. Sakr, N. Taengnoi, K. R. Bottrill, F. Poletti, P. Petropoulos, and D. J. Richardson, "Wideband Transmission in the 1-μm Band based on a Hollow-core Fiber and Wideband YDFA," in *Optical Fiber Communication Conference*(Optica Publishing Group2023), p. W4D. 5.

[63] X. Huang, S. Liang, L. Xu, D. J. Richardson, and Y. Jung, "Wideband (13.7 THz) Gain-Flattened Yb-Doped Fiber Amplifier for Telecommunication Applications," IEEE Photonics Technology Letters (2024).

[64] I. Bufetov, and E. Dianov, "Bi-doped fiber lasers," Laser Physics Letters **6**, 487 (2009).

[65] N. Thipparapu, Y. Wang, S. Wang, A. Umnikov, P. Barua, and J. Sahu, "Bi-doped fiber amplifiers and lasers," Optical Materials Express **9**, 2446-2465 (2019).

[66] H. Xiao, J. Leng, H. Zhang, L. Huang, J. Xu, and P. Zhou, "High-power 1018 nm ytterbium-doped fiber laser and its application in tandem pump," Applied Optics **54**, 8166-8169 (2015).

[67] M. E. Marhic, P. A. Andrekson, P. Petropoulos, S. Radic, C. Peucheret, and M. Jazayerifar, "Fiber optical parametric amplifiers in optical communication systems," Laser & Photonics Reviews **9**, 50-74 (2015).

[68] M. Yamada, and M. Shimizu, "Ultra Wideband Amplification Technologies for Optical Fiber Amplifiers," JOURNAL-INSTITUTE OF ELECTRONICS INFORMATION AND COMMUNICATION ENGINEERS **86**, 234-241 (2003).

[69] F. Abdullah, M. Jamaludin, M. Ali, M. Al-Mansoori, A. Abass, and T. Al-Mashhadani, "Influence of Raman pump direction on the performance of serial hybrid fiber amplifier in C+ L-band," in *2018 IEEE 7th International Conference on Photonics (ICP)*(IEEE2018), pp. 1-3.

[70] M. J. Connelly, *Semiconductor optical amplifiers* (Springer Science & Business Media, 2007), ISBN: 0306481561.

[71] N. K. Dutta, and Q. Wang, *Semiconductor optical amplifiers* (World scientific, 2013), ISBN: 9814489050.

[72] C. H. Yeh, and S. Chi, "Utilizations of EDFA and SOA in series for broadband gain amplification," Laser Physics Letters **4**, 433 (2007).

[73] K. H. Lin, and J. H. Lin, "Amplification of supercontinuum by semiconductor and Er-doped fiber optical amplifiers," Laser Physics Letters **5**, 449 (2008).

[74] Y. Jung, Q. Kang, S. Jain, S.-u. Alam, and D. J. Richardson, "Recent progress in SDM amplifiers," in *Next-Generation Optical Communication: Components, Sub-Systems, and Systems VI*(International Society for Optics and Photonics2017), pp. 9-15.

[75] Y. Jung, S. U. Alam, Z. Li, A. Dhar, D. Giles, I. P. Giles, J. K. Sahu, F. Poletti, L. Grüner-Nielsen, and D. J. Richardson, "First demonstration and detailed characterization of a multimode amplifier for space division multiplexed transmission systems," Optics express **19**, 1094-4087 (2011).

[76] C. Kim, C. Giles, and Y. C. Chung, "Two-stage optical limiting fiber amplifier using a synchronized etalon filter," IEEE Photonics Technology Letters **10**, 285-287 (1998).

[77] J. Minowa, and Y. Fujii, "Dielectric multilayer thin-film filters for WDM transmission systems," Journal of Lightwave Technology **1**, 116-121 (1983).

[78] P. G. Verly, "Design of a robust thin-film interference filter for erbium-doped fiber amplifier gain equalization," Applied Optics **41**, 3092-3096 (2002).

[79] M. Harumoto, M. Shigehara, and H. Suganuma, "Gain-flattening filter using long-periodfiber gratings," Journal of Lightwave Technology **20**, 1027 (2002).

[80] A. M. Vengsarkar, J. R. Pedrazzani, J. B. Judkins, P. J. Lemaire, N. S. Bergano, and C. R. Davidson, "Long-period fiber-grating-based gain equalizers," Optics Letters **21**, 336-338 (1996).

[81] B. Poumellec, and F. Kherbouche, "The photorefractive Bragg gratings in the fibers for telecommunications," Journal de Physique III **6**, 1595-1624 (1996).

[82] N. Takato, T. Kominato, A. Sugita, K. Jinguji, H. Toba, and M. Kawachi, "Silica-based integrated optic Mach-Zehnder multi/demultiplexer family with channel spacing of 0.01-250 nm," IEEE Journal on Selected Areas in Communications **8**, 1120-1127 (1990).

[83] F. Horst, W. M. Green, S. Assefa, S. M. Shank, Y. A. Vlasov, and B. J. Offrein, "Cascaded Mach-Zehnder wavelength filters in silicon photonics for low loss and flat pass-band WDM (de-) multiplexing," Optics Express **21**, 11652-11658 (2013).

[84] R. Betts, S. Frisken, and D. Wong, "Split-beam Fourier filter and its application in a gain-flattened EDFA," in *Optical Fiber Communication Conference*(Optica Publishing Group1995), p. TuP4.

[85] A. M. Vengsarkar, P. J. Lemaire, J. B. Judkins, V. Bhatia, T. Erdogan, and J. E. Sipe, "Long-period fiber gratings as band-rejection filters," Journal of Lightwave Technology **14**, 58-65 (1996).

[86] B. Ortega, L. Dong, W. Liu, J. De Sandro, L. Reekie, S. Tsypina, V. Bagratashvili, and R. Laming, "High-performance optical fiber polarizers based on long-period gratings in birefringent optical fibers," IEEE Photonics Technology Letters **9**, 1370-1372 (1997).

[87] Y. Liu, Y. Jung, Z. Yang, L. Zhang, and D. J. Richardson, "Wideband and low-loss mode scrambler for few-mode fibers based on distributed multiple point-loads," Photonics Journal **13**, 1-7 (2021).

[88] I. Del Villar, O. Fuentes, F. Chiavaioli, J. M. Corres, and I. R. Matias, "Optimized strain long-period fiber grating (LPFG) sensors operating at the dispersion turning point," Journal of Lightwave Technology **36**, 2240-2247 (2018).

[89] R. C. Youngquist, J. L. Brooks, and H. J. Shaw, "Two-mode fiber modal coupler," Optics Letters **9**, 177-179 (1984).

[90] P. D. Gianino, and B. Bendow, "Calculations of stress-induced changes in the transverse refractive-index profile of optical fibers," Applied optics **20**, 430-434 (1981).

[91] S. J. Garth, "Intermodal coupling in an optical fiber using periodic stress," Applied optics **28**, 581-587 (1989).

[92] G. B. Richard, and M. S. Ali, *Roark's Formulas for Stress and Strain, Ninth Edition* (McGraw-Hill Education, 2020), 9781260453751.

[93] R. Gafsi, and M. A. El-Sherif, "Analysis of Induced-Birefringence Effects on Fiber Bragg Gratings," Optical Fiber Technology **6**, 299-323 (2000).

[94] Y. Wang, "Review of long period fiber gratings written by CO2 laser," Journal of Applied Physics **108**, 081101 (2010).

[95] M.-S. Yoon, H.-J. Kim, S.-J. Kim, and Y.-G. Han, "Influence of the waist diameters on transmission characteristics and strain sensitivity of microtapered long-period fiber gratings," Optics Letters **38**, 2669-2672 (2013).

[96] S. G. Kosinski, and A. M. Vengsarkar, "Splicer-based long-period fiber gratings," in *OFC '98. Optical Fiber Communication Conference and Exhibit. Technical Digest. Conference Edition. 1998 OSA Technical Digest Series Vol.2 (IEEE Cat. No.98CH36177)*(1998), pp. 278-279.

[97] F. P. W. Melchels, J. Feijen, and D. W. Grijpma, "A review on stereolithography and its applications in biomedical engineering," Biomaterials **31**, 6121-6130 (2010).

[98] M. Smietana, W. J. Bock, P. Mikulic, and J. Chen, "Increasing sensitivity of arc-induced long-period gratings—pushing the fabrication technique toward its limits," Measurement Science and Technology **22**, 015201 (2010).

[99] C. Colaço, P. Caldas, I. D. Villar, R. Chibante, and G. Rego, "Arc-Induced Long-Period Fiber Gratings in the Dispersion Turning Points," Journal of Lightwave Technology **34**, 4584-4590 (2016).

[100] P. J. Winzer, "Energy-Efficient Optical Transport Capacity Scaling Through Spatial Multiplexing," IEEE Photonics Technology Letters **23**, 851-853 (2011).

[101] V. A. J. M. Sleiffer, Y. Jung, V. Veljanovski, R. G. H. van Uden, M. Kuschnerov, H. Chen, B. Inan, L. G. Nielsen, Y. Sun, D. J. Richardson, S. U. Alam, F. Poletti, J. K. Sahu, A. Dhar, A. M. J. Koonen, B. Corbett, R. Winfield, A. D. Ellis, and H. de Waardt, "73.7 Tb/s (96 x 3 x 256-Gb/s) mode-division-multiplexed DP-16QAM transmission with inline MM-EDFA," Optics Express **20**, B428-B438 (2012).

[102] P. J. Winzer, and G. J. Foschini, "MIMO capacities and outage probabilities in spatially multiplexed optical transport systems," Optics Express **19**, 16680-16696 (2011).

[103] S. Randel, R. Ryf, A. Sierra, P. J. Winzer, A. H. Gnauck, C. A. Bolle, R.-J. Essiambre, D. W. Peckham, A. McCurdy, and R. Lingle, "6×56-Gb/s mode-division multiplexed transmission over 33-km few-mode fiber enabled by 6×6 MIMO equalization," Optics Express **19**, 16697-16707 (2011).

[104] K. P. Ho, and J. M. Kahn, "Statistics of Group Delays in Multimode Fiber With Strong Mode Coupling," Journal of Lightwave Technology **29**, 3119-3128 (2011).

[105] K.-P. Ho, and J. M. Kahn, "Mode-dependent loss and gain: statistics and effect on mode-division multiplexing," Optics Express **19**, 16612-16635 (2011).

[106] H. Chen, N. K. Fontaine, B. Huang, R. Ryf, and I. Giles, "Demonstration of Mode Scramblers Supporting 6 Spatial Modes to Reduce Differential Group Delays," in *2017 European Conference on Optical Communication (ECOC)*(2017), pp. 1-3.

[107] J. Fang, A. Li, and W. Shieh, "Low-DMD few-mode fiber with distributed long-period grating," Optics Letters **40**, 3937-3940 (2015).

[108] H. Liu, H. Wen, B. Huang, R. A. Correa, P. Sillard, H. Chen, Z. Li, and G. Li, "Reducing group delay spread using uniform long-period gratings," Scientific Reports **8**, 3882 (2018).

[109] J. Li, N. K. Fontaine, H. Chen, R. Ryf, M. Cappuzzo, R. Kopf, A. Tate, H. Safar, C. Bolle, D. T. Neilson, E. Burrows, K. W. Kim, P. Sillard, F. Achten, J. Du, Z. He, M. Bigot, A. Amezcua-Correa, R. A. Correa, and J. Carpenter, "Design and Demonstration of Mode Scrambler Supporting 10 Modes Using Multiplane Light Conversion," in *2018 European Conference on Optical Communication (ECOC)*(2018), pp. 1-3.

[110] L. Su, K. S. Chiang, and C. Lu, "Microbend-induced mode coupling in a graded-index multimode fiber," Applied Optics **44**, 7394-7402 (2005).

[111] S. Warm, and K. Petermann, "Capacity increase in spliced mode-mulitplexd transmission systems by using mode mixers," in *2012 IEEE Photonics Society Summer Topical Meeting Series*(2012), pp. 201-202.

[112] Y. Jung, Q. Kang, J. K. Sahu, B. Corbett, J. O. Callagham, F. Poletti, S. Alam, and D. J. Richardson, "Reconfigurable Modal Gain Control of a Few-Mode EDFA Supporting Six Spatial Modes," IEEE Photonics Technology Letters **26**, 1100-1103 (2014).

[113] D. J. Derickson, R. Fortenberry, M. Scobey, R. Sommer, and L. Stokes, "Advancements in thin film filters for telecommunications applications," in *Active and Passive Optical Components for WDM Communications III*(SPIE2003), pp. 595-607.

[114] M. Lequime, "Tunable thin film filters: review and perspectives," Advances in Optical Thin Films **5250**, 302-311 (2004).

[115] Y. Mimura, K. Mizuno, Y. Iida, K. Masuda, T. Itoh, and Y. Nishi, "Gain-flattening filters using dielectric multilayer thin film," Furukawa Review **21**, 12-16 (2002).

[116] B. M. Zhang, Y. Feng, D. Lin, J. H. V. Price, J. Nilsson, S. Alam, P. P. Shum, D. N. Payne, and D. J. Richardson, "Demonstration of arbitrary temporal shaping of picosecond pulses in a radially polarized Yb-fiber MOPA with > 10 W average power," Optics Express **25**, 15402-15413 (2017).

[117] P. Manurkar, N. Jain, M. Silver, Y.-P. Huang, C. Langrock, M. M. Fejer, P. Kumar, and G. S. Kanter, "Multidimensional mode-separable frequency conversion for high-speed quantum communication," Optica **3**, 1300-1307 (2016).

[118] J. Y. Sung, K. T. Cheng, C. W. Chow, C. H. Yeh, and C. L. Pan, "A scalable and continuous-upgradable optical wireless and wired convergent access network," Optics Express **22**, 12779-12784 (2014).

[119] J. Zhou, A. Luo, Z. Luo, X. Wang, X. Feng, and B.-o. Guan, "Dual-wavelength single-longitudinal-mode fiber laser with switchable wavelength spacing based on a graphene saturable absorber," Photonics Research **3**, A21-A24 (2015).

[120] Y. Sun, A. K. Srivastava, J. Zhou, and J. W. Sulhoff, "Optical fiber amplifiers for WDM optical networks," Bell Labs Technical Journal **4**, 187-206 (1999).

[121] A. R. Chraplyvy, "High-capacity lightwave transmission experiments," Bell Labs Technical Journal **4**, 230-245 (1999).

[122] G. P. Agrawal, *Fiber-optic communication systems* (John Wiley & Sons, 2012), ISBN: 0470922826.

[123] R.-J. Essiambre, G. Kramer, P. J. Winzer, G. J. Foschini, and B. Goebel, "Capacity limits of optical fiber networks," Journal of Lightwave Technology **28**, 662-701 (2010).

[124] https://telecom-info.njdepot.ericsson.net/site-cgi/ido/docs.cgi?ID=SEARCH&DOCUMENT=GR.

[125] P. M. Gabla, "Bright prospects for erbium-doped fiber amplifiers in future lightwave communication systems," Fiber & Integrated Optics **10**, 109-125 (1991).

[126] H. Iwamura, S. Hayashi, and H. Iwasaki, "A compact optical isolator using a Y 3 Fe 5 O 12 crystal for near infra-red radiation," Optical and Quantum Electronics **10**, 393-398 (1978).

[127] M. Pal, M. C. Paul, A. Dhar, A. Pal, R. Sen, K. Dasgupta, and S. K. Bhadra, "Investigation of the optical gain and noise figure for multi-channel amplification in EDFA under optimized pump condition," Optics Communications **273**, 407-412 (2007).

[128] R. Zhang, and R. R. Mansour, "Dual-band dielectric-resonator filters," IEEE Transactions on Microwave Theory and Techniques **57**, 1760-1766 (2009).

[129] I.-B. Sohn, and J.-W. Song, "Gain flattened and improved double-pass two-stage EDFA using microbending long-period fiber gratings," Optics Communications **236**, 141-144 (2004).

[130] H. Chotard, Y. Painchaud, A. Mailloux, M. Morin, F. Trepanier, and M. Guy, "Group delay ripple of cascaded Bragg grating gain flattening filters," IEEE Photonics Technology Letters **14**, 1130-1132 (2002).

[131] B. Zhu, M. Law, J. Rooney, S. Shenk, M. F. Yan, and D. J. DiGiovanni, "High-power broadband Yb-free clad-pumped EDFA for L-band DWDM applications," Optics Letters **39**, 72-75 (2014).

[132] K. H. Yla-Jarkko, C. Codemard, J. Singleton, P. W. Turner, I. Godfrey, S. U. Alam, J. Nilsson, J. K. Sahu, and A. B. Grudinin, "Low-noise intelligent cladding-pumped L-band EDFA," IEEE Photonics Technology Letters **15**, 909-911 (2003).

[133] S. Liang, J. D. Downie, S. Makovejs, M. Edwards, and Y. Jung, "A study of the power conversion efficiency of EDFAs for future multicore submarine transmission systems," in *IET Conference Proceedings CP839*(IET2023), pp. 554-557.

[134] M. Cantono, R. Schmogrow, M. Newland, V. Vusirikala, and T. Hofmeister, "Opportunities and Challenges of C+L Transmission Systems," Journal of Lightwave Technology **38**, 1050-1060 (2020).

[135] P. Hazarika, M. Tan, A. Donodin, S. Noor, I. Phillips, P. Harper, J. S. Stone, M. J. Li, and W. Forysiak, "E-, S-, C- and L-band coherent transmission with a multistage discrete Raman amplifier," Optics Express **30**, 43118-43126 (2022).

[136] B. J. Puttnam, R. S. Luis, Y. Huang, I. Phillips, D. Chung, N. K. Fontaine, G. Rademacher, M. Mazur, L. Dallachiesa, H. Chen, W. Forysiak, R. Man, R. Ryf, D. T. Neilson, and H. Furukawa, "301 Tb/s E, S, C+L-band transmission over 212 nm bandwidth with E-band bismuth-doped fiber amplifier and gain equalizer," in *49th European Conference on Optical Communications (ECOC 2023)*(2023), pp. 1674-1677.

[137] N. K. Thipparapu, Y. Wang, S. Wang, A. A. Umnikov, P. Barua, and J. K. Sahu, "Bi-doped fiber amplifiers and lasers [Invited]," Optical Materials Express **9**, 2446-2465 (2019).

[138] M. Arbore, Y. Zhou, H. Thiele, J. Bromage, and L. Nelson, "S-band erbium-doped fiber amplifiers for WDM transmission between 1488 and 1508 nm," in *OFC 2003 Optical Fiber Communications Conference, 2003.*(2003), pp. 374-376 vol.371.

[139] H. Ono, M. Yamada, and M. Shimizu, "S-Band Erbium-Doped Fiber Amplifiers With a Multistage Configuration-Design,Characterization, and Gain Tilt Compensation," Journal of Lightwave Technology **21**, 2240 (2003).

[140] K. Thyagarajan, and C. Kakkar, "S-band single-stage EDFA with 25-dB gain using distributed ASE suppression," IEEE Photonics Technology Letters **16**, 2448-2450 (2004).

[141] C. Lei, H. Feng, Y. Messaddeq, and S. Larochelle, "Investigation of Bi-Directionally, Dual-Wavelength Pumped Extended L-Band EDFAs," IEEE Photonics Technology Letters **32**, 1227-1230 (2020).

[142] C. Bo-Hun, P. Hyo-Hoon, and C. Moo-Jung, "New pump wavelength of 1540-nm band for long-wavelength-band erbium-doped fiber amplifier (L-band EDFA)," Journal of quantum electronics **39**, 1272-1280 (2003).

[143] Y. Chien-Hung, L. Chien-Chung, and S. Chi, "120-nm bandwidth erbium-doped fiber amplifier in parallel configuration," IEEE Photonics Technology Letters **16**, 1637-1639 (2004).

[144] M. Foroni, F. Poli, A. Cucinotta, and S. Selleri, "S-band depressed-cladding erbium-doped fiber amplifier with double-pass configuration," Optics Letters **31**, 3228-3230 (2006).

[145] L. Wang, M. Sharma, F. Maes, S. Jalilpiran, F. E. Durak, Y. Messaddeq, S. LaRochelle, and Z. Jiang, "Low Cost Solution for Super L-Band Fiber Amplifier based on Single-mode and Multi-mode Hybrid Pumping Scheme," in *Optical Fiber Communication Conference (OFC) 2022*(Optica Publishing Group, San Diego, California, 2022), p. W3J.4.

[146] B.-H. Choi, H.-H. Park, and M.-J. Chu, "New pump wavelength of 1540-nm band for long-wavelength-band erbium-doped fiber amplifier (L-band EDFA)," Journal of quantum electronics **39**, 1272-1280 (2003).

[147] L. M. Sousa, R. Oliveira, R. N. Nogueira, and A. M. Rocha, "Pressure-Induced Long-Period Gratings in Multi-Core Fibers," in *2023 23rd International Conference on Transparent Optical Networks (ICTON)*(2023), pp. 1-4.

[148] M. Wang, C. Guan, Z. Yu, J. Yang, Z. Zhu, J. Shi, J. Yang, and L. Yuan, "Core-independent inscription of LPGs in twin-core fiber by CO2 laser and coupling between LPGs," Optics Express **27**, 15786-15793 (2019).

[149] I. Gasulla, D. Barrera, J. Hervás, and S. Sales, "Spatial Division Multiplexed Microwave Signal processing by selective grating inscription in homogeneous multicore fibers," Scientific Reports **7**, 41727 (2017).

[150] V. Mikhailov, Y. Sun, J. Luo, F. Khan, D. Inniss, Y. Dulashko, M. Lee, J. Mann, R. S. Windeler, P. S. Westbrook, J. W. Nicholson, and D. J. DiGiovanni, "1255–1355 nm (17.6 THz) Bandwidth O-Band BDFA Pumped Using Uncooled Multimode 915 nm Laser Diode via YDF Conversion Stage," Journal of Lightwave Technology **42**, 1265-1271 (2024).

[151] Y. Wang, S. Wang, A. Halder, and J. Sahu, "(INVITED) Bi-doped optical fibers and fiber amplifiers," Optical Materials: X **17**, 100219 (2023).